Alessandro Masat

B-PLANE ORBITAL RESONANCE ANALYSIS AND APPLICATIONS

POLITECNICO
MILANO 1863

B-PLANE ORBITAL RESONANCE ANALYSIS AND APPLICATIONS

PERTURBED SEMI-ANALYTICAL MODEL FOR PLANETARY PROTECTION AND DEFENCE APPLIED TO BALLISTIC RESONANT FLYBY DESIGN

Laurea Magistrale
Space Engineering - Ingegneria Spaziale - BV(470)

DAER - Dipartimento di Scienze e Tecnologie Aerospaziali
Politecnico di Milano

Academic year 2018-2019

Candidate: Alessandro Masat

Supervisor: Camilla Colombo
Co-supervisor: Matteo Romano

When referring to this work, full bibliographic details must be given:
Alessandro Masat, "B-plane orbital resonance analysis and applications: Perturbed semi-analytical model for planetary protection and defence applied to ballistic resonant flyby design ", 2019 , Scuola di Ingegneria Industriale e dell'Informazione, DAER - Dipartimento di Scienze e Tecnologie Aerospaziali, Politecnico di Milano, Supervisor: Camilla Colombo, Co-supervisor: Matteo Romano.

DEDICATION

A warm thank you to Camilla and Matteo, whose advice and supervision have been always precious and valuable.

Thanks to every single friend back home in Fossalta, whose support and help was never missing, not when living in Milano, not even when moved to Stockholm. Thanks to Gianluca and Carlo, we grew up together, have been sharing a whole life and managed to stay this close even though spread over the world, you helped me keeping a piece of home in myself wherever I've gone. Thanks to Giulia, a true shoulder where to lean against in some moments of need. Thanks to Marco, Ilario, Francesco, Mirco, Simone, Eros, Chiara and all the others, true friends who I will always be pleased to meet when coming back home.

Thanks to all the friends I had met in Milano, we had been sharing most of our studies and fatigues. Thanks to Tommaso, we together moved to Milano as freshmen and together lived four unforgettable years. Thanks to Dario, we shared 6 full years of university experiences, both in Milano and in Stockholm, a true friend always available for help and advice. Thanks to Salvatore and Gabriele, I will never forget our in-field talks and view-point sharing, including making fun of our stuff to lighten the study burdens we had been facing. Thanks to Chiara, smiles and laughs were never missing in your company. Thanks to Alessandro, Alessandro, Luca, Domenico, Giovanni, Michele, Niccolò and Lorenzo. We shared only my last year in Milano, but I really say it's one of the best memories I have with me.

Thanks to the many friends, from all over the world, I had the luck to meet in my experience in Stockholm. Thanks to the friends in MAIN, THS and KTH, you helped me opening my mind and made me discover new points of view to student and international life. A full page would be needed to list you all, just know that even if your name is not appearing here and we have been a little close my thoughts are with you all. Thanks to Matteo, another double degree colleague of mine, for the great time and experience we had in the past few months. Thanks to my flatmate Valerio and to Mattia, Federico and Pablo, I would have never imagined to build such true and deep friendships in the very little time we got to spend together. Wherever in the world we will be in our future, I know we will always be able to rely on each other.

Thanks to my family, to my little sister Martina for your hope, kindness and faith. Being far does not affect the love I feel for you, no matter what the future will bring to our lives. Thanks to my mother Francesca for worrying so much about me and for having

been doing the dirty job of highlighting my weaknesses for my own goodness, sake and growth. Without your continuous and restless words I couldn't have been brave and foolish enough to make the decisions I've made. Thanks to my father Loris for being the strongest man and life example I could ever want. You've made me always feel safe, supported and helped, no matter what situation life put in front of me. Thank you all again, for your encouragements and unconditional love, without you no experience or study path would have ever been possible.

To my family.

ABSTRACT

Many space engineering and orbital mechanics applications seek for the usage of focused mathematical models, capable of providing useful insight onto particular phenomena or exploiting some theoretical and physical tools to reduce the computational costs and/or increase the level of accuracy reached. Orbital resonances are one of the phenomena that needs to be properly modelled, both for exploiting such features in the mission design phase and to predict possible resonant returns of threatening objects closely approaching a specified planet.

This work deals indeed with one of the possible models of orbital resonances, representing such a physical phenomenon in the b-plane reference frame with an analysis on the resonant trajectories performed at the moment of close encounter. Before this, flybys are an important source of uncertainty in the numerical simulations, which then need to be as accurate as possible to be used as benchmark. To this extent, a highly efficient method to account for general relativity effects in the N-body propagation is developed, tested and validated, to be then used as precise benchmark for the resonance analysis and application.

The b-plane resonance model is a strictly patched conics theory which does not account for perturbations. A semi-analytical extension of the current b-plane resonance model is proposed to account for perturbing effects inside the planet's sphere of influence. Introducing a set of perturbing coefficients brings the model to match the simulation results at the b-plane point where such coefficients are computed, as well as to be a highly reliable approximation in its vicinity, performing a validation with Monte-Carlo simulated data.

An extension of the validation proposed would lead to a complete planetary protection or defence application, whereas in its final part the work will show the flexibility of the model by looking at it from a different perspective. A ballistic resonant flyby design application will be implemented by solving a multi-level optimisation problem, to modify an initial trajectory into a new one on the same Tisserand level. Without dealing with the specific case of resonances, the b-plane reference frame embeds a smart geometrical framework where to express and design flyby deflections, whose power will be shown in terms of accuracy achieved and computational cost required.

Once completed by detaching from the patched conics approximation, such a model could bring remarkable simplifications in planetary protection applications, reducing the need of propagating a high number of Monte Carlo samples, and would increase the precision of the defence analyses against impacts from near-Earth threatening asteroids. About the application proposed here, internal and/or external

integration could eventually lead to an enhanced efficiency of the current mission design strategies and could widen the internal proposed capabilities, providing high precision and almost optimal results with lowered computational costs.

PUBLICATIONS

- **Alessandro Masat, Matteo Romano, Camilla Colombo**, *Orbital resonance analysis in Monte Carlo simulations for planetary protection and defence*
  AIDAA XXV International Congress, Università La Sapienza, Rome, Italy

ACKNOWLEDGMENTS

The research leading to these results has received funding from the European Research Council (ERC) under the European Union's Horizon 2020 research and innovation programme as part of project COMPASS (Grant agreement No 679086), www.compass.polimi.it.

The author has been enrolled in a T.I.M.E. Double Degree programme between Politecnico di Milano and KTH Royal Institute of Technology during the development of this work, exploiting infrastructural resources in both the universities.

CONTENTS

LIST OF FIGURES

LIST OF TABLES

ACRONYMS

GR	-	General relativity
SR	-	Special relativity
PNM	-	Post-newtonian mechanics
PPN	-	Parametrised post-newtonian mechanics

Part I

INTRODUCTION AND BENCHMARK

1

INTRODUCTION

The variety of applications within the orbital mechanics field itself is remarkably high. The very same mathematical and physical tools are used for many different purposes and applications, starting from the study of the orbital motion of natural bodies, passing through the first draft of mission analysis and manoeuvre and command design, finally for the final optimisation of rather complex multi-body trajectories.

The presented work will deal with orbital resonances in different applications of the common concept, which indeed is simply requiring two orbits whose periods are in a ratio equal to the one of two integers.

The planetary protection and defence side seeks to obtain a reliable prediction of impact probabilities of threatening objects, asteroids and natural celestial bodies in the case of defence, human-crafted disposal objects in the case of protection to avoid the contamination of planetary environments other than Earth. In fact, a danger of this kind is not finished when an impact is avoided in a simple close approach: some flybys feature a particular configuration such that a consequent close approach can be predicted. It is then crucial to design end-of-life manoeuvres and asteroid deflections being sure under a high confidence level that the small objects under analysis are injected in proper interplanetary orbits, such that they will not dangerously approach any planet or relevant body in future epochs. As a support for this last statement, an example is brought by the European Space Agency's planetary protection requirements [16], that ask to design interplanetary injections so that an uncontrollable spacecraft or disposal object has an impact probability with any planet of 0.01%, over 100 years forward in time.

Such high confidence levels are reached only through either extremely precise simulation or analytical models. About this last ones, their validation against a solid benchmark is a necessary step to be taken before their implementation and usage. High accuracy simulations involve any kind of perturbing effects and can actually be used for benchmark purposes, provided that their precision is ensured. To this extent, some cases where the full N-body simulation is not enough to guarantee minimum accuracy requirements will be shown, particularly in the long term propagation case (typical of planetary protection applications) and when the trajectory experiences close

encounters. It is of common knowledge [19] that in orbital motion a small error propagates and increases in time, with sudden steep growths every time that a flyby occurs, therefore the most accurate simulation strategy is required if it is to be used as benchmark. In this regard, the effect of general relativity on the N-body dynamics will be studied, to eventually validate and implement a simulation method that will be used as benchmark for all the upcoming parts of the work.

The word benchmark is fundamental in the purposes of this work, because, despite such a complete physical model features incomparable accuracy and reliability, the computational cost remains too high, particularly when performing Monte Carlo simulations where the motion of thousands of virtual bodies is propagated. Moreover, given that such simulations are carried out in a cartesian reference frame, some physical insight on the various orbital phenomena is missing, that needs to post process the propagation results to be retrieved. Referring again specifically to orbital resonances, there exists then the need to model reliable analytical tools, in order to obtain accurate predictions even without performing complete high precision simulations.

The b-plane reference frame is a step in this direction, where the deflection that a small body undergoes during a close approach is modelled by rather simple geometrical and mathematical relations. This work, particularly Part ii, aims to increase the precision of the b-plane tool by applying corrective coefficients obtained from simulated data; a detailed and referenced introduction of the b-plane reference frame will be given in the dedicated Chapter 4.

Finally, it is important to remember that such a reference frame is suitable for deflections of all kind and not only the resonant ones. To this extent, the deflection design capabilities of the b-plane model together with the concept of orbital resonances will be exploited in Part iii to design interplanetary resonant ballistic trajectories. Many works tackled the resonant orbit design problem, which will be described in detail in Chapter 10, in order also to provide some context about the current works and applications in similar directions.

As already mentioned, the first chapter of this work will be devoted to building a proper benchmark to rely on for all the future considerations, assumptions and modelling choices. Note that only the main results are reported in Chapter 2, leaving the conceptual details of general relativity in the appendix, since they are not the main focus of the work. The description given there is meant to be mostly conceptual and understandable with the classical engineering mathematical and physical background, thus a read-through is recommended for a complete understanding of what discussed in Chapter 2.

2

GENERAL RELATIVITY IN THE N-BODY DYNAMICS

2.1 INTRODUCTION

What presented in this chapter has been entirely developed within this thesis work, in this regard no reference material is available at the best of the author's knowledge. For a complete conceptual view of the model proposed here the reading of Appendix A and B is recommended, although it is not reported in the main body of the work because of the focus on orbital resonances developed in the next parts. Before digging more into general relativity (GR) details, the main reason of studying its effect on the N-body dynamics is to have a suitable benchmark where to test other orbital models. As it will be shown shortly, there are cases where the N-body propagation is not precise enough, particularly for long term propagations associated, for instance, with planetary protection and defence applications.

The test data used for the validation have been taken from NASA's toolkit SPICE [1], a database containing the propagated ephemerides of many celestial objects and that is known to be accounting for GR effects. Simulations are carried out only on asteroids, because the goal of this chapter has to be intended as the development, implementation and validation of consistent methods for the N-Body propagation taking into account GR. The most robust validation strategy is then the propagation of objects undergoing the pure gravitational motion, without introducing any sort of manoeuvres.

Note that only few meaningful cases are reported in this Chapter, despite, being it the validation of the benchmark needed for the rest of the work, many of them have been run and all of them showed the very same successful behaviour. For the sake of conciseness they are not included in the work, given that they would add only redundancy and no value to the discussion presented.

2.2 GENERAL MODEL AND METHOD

The model chosen to implement GR effects in the N-body equation of motion comes originally from [36], with the formulation used here proposed by [25]:

$$\begin{aligned}\ddot{\mathbf{r}}_i = &\sum_{j\neq i}\frac{\mu_j(\mathbf{r}_j-\mathbf{r}_i)}{r_{ij}^3}\Bigg\{1-\frac{4}{c^2}\sum_{k\neq i}\frac{\mu_k}{r_{ik}}-\frac{1}{c^2}\sum_{k\neq j}\frac{\mu_k}{r_{jk}}+\left(\frac{v_i}{c}\right)^2+2\left(\frac{v_j}{c}\right)^2\\&-\frac{4}{c^2}\dot{\mathbf{r}}_i\cdot\dot{\mathbf{r}}_j-\frac{3}{2c^2}\left[\frac{(\mathbf{r}_i-\mathbf{r}_j)\cdot\dot{\mathbf{r}}_j}{r_{ij}}\right]^2+\frac{1}{2c^2}(\mathbf{r}_j-\mathbf{r}_i)\cdot\ddot{\mathbf{r}}_j\Bigg\}\\&+\frac{1}{c^2}\sum_{j\neq i}\frac{\mu_j}{r_{ij}^3}\left\{\left[\mathbf{r}_i-\mathbf{r}_j\right]\cdot\left[4\dot{\mathbf{r}}_i-3\dot{\mathbf{r}}_j\right]\right\}(\dot{\mathbf{r}}_i-\dot{\mathbf{r}}_j)+\frac{7}{2c^2}\sum_{j\neq i}\frac{\mu_j\ddot{\mathbf{r}}_j}{r_{ij}}\end{aligned} \tag{2.1}$$

The dynamics, described by Equation (2.1), to be propagated looks very complex: many nonlinear terms (on position and velocity) are present, as well as coupling can be seen among all of them. However, one should not forget that in a propagation formalism all that matters is the state and its derivatives and, in this case, the state $\mathbf{x}_i$ for body i can be defined as the usual one for N-Body propagations:

$$\mathbf{x}_i = \begin{Bmatrix}\mathbf{r}_i\\ \dot{\mathbf{r}}_i\end{Bmatrix} \tag{2.2}$$

where $\mathbf{r}_i$ and $\dot{\mathbf{r}}_i$ are i-th body's position and velocity respectively.

A propagator needs the equation to propagate in the form

$$\dot{\mathbf{x}}_i = \mathbf{f}(\mathbf{x}_i) \tag{2.3}$$

with $\mathbf{f}$ that can be as complex as one wants. It will be shown shortly that even in the GR case the equation can assume a shape pretty similar to the one reported in Equation (2.3).

Equation (2.1) is then re-arranged in the following way:

$$\begin{aligned}\ddot{\mathbf{r}}_i = &\sum_{j\neq i}\frac{\mu_j(\mathbf{r}_j-\mathbf{r}_i)}{r_{ij}^3}+\Bigg\{\sum_{j\neq i}\frac{\mu_j(\mathbf{r}_j-\mathbf{r}_i)}{r_{ij}^3}\Bigg\{-\frac{4}{c^2}\sum_{k\neq i}\frac{\mu_k}{r_{ik}}-\frac{1}{c^2}\sum_{k\neq j}\frac{\mu_k}{r_{jk}}\\&+\left(\frac{v_i}{c}\right)^2+2\left(\frac{v_j}{c}\right)^2-\frac{4}{c^2}(\dot{\mathbf{r}}_i\cdot\dot{\mathbf{r}}_j)-\frac{3}{2c^2}\left[\frac{(\mathbf{r}_i-\mathbf{r}_j)\cdot\dot{\mathbf{r}}_j}{r_{ij}}\right]^2\Bigg\}\\&+\frac{1}{c^2}\sum_{j\neq i}\frac{\mu_j}{r_{ij}^3}\left\{\left[\mathbf{r}_i-\mathbf{r}_j\right]\cdot\left[4\dot{\mathbf{r}}_i-3\dot{\mathbf{r}}_j\right]\right\}(\dot{\mathbf{r}}_i-\dot{\mathbf{r}}_j)\Bigg\}\\&+\frac{1}{2c^2}\sum_{j\neq i}\frac{\mu_j(\mathbf{r}_j-\mathbf{r}_i)}{r_{ij}^3}\left[(\mathbf{r}_j-\mathbf{r}_i)\cdot\ddot{\mathbf{r}}_j\right]+\frac{7}{2c^2}\sum_{j\neq i}\frac{\mu_j\ddot{\mathbf{r}}_j}{r_{ij}}\end{aligned} \tag{2.4}$$

with three different groups can be highlighted, of which two can be defined as:

$$\mathbf{a}_i^{Newt} := \sum_{j\neq i}\frac{\mu_j(\mathbf{r}_j-\mathbf{r}_i)}{r_{ij}^3} \tag{2.5}$$

$$\begin{aligned}\mathbf{a}_i^{Rel} := \sum_{j\neq i} \frac{\mu_j(\mathbf{r}_j-\mathbf{r}_i)}{r_{ij}^3}\Bigg\{ &-\frac{4}{c^2}\sum_{k\neq i}\frac{\mu_k}{r_{ik}} - \frac{1}{c^2}\sum_{k\neq j}\frac{\mu_k}{r_{jk}} + \left(\frac{v_i}{c}\right)^2 + 2\left(\frac{v_j}{c}\right)^2 \\ &- \frac{4}{c^2}(\dot{\mathbf{r}}_i\cdot\dot{\mathbf{r}}_j) - \frac{3}{2c^2}\left[\frac{(\mathbf{r}_i-\mathbf{r}_j)\cdot\dot{\mathbf{r}}_j}{r_{ij}}\right]^2\Bigg\} + \frac{1}{c^2}\sum_{j\neq i}\frac{\mu_j}{r_{ij}^3}\Big\{\big[\mathbf{r}_i-\mathbf{r}_j\big] \\ &\cdot\big[4\dot{\mathbf{r}}_i-3\dot{\mathbf{r}}_j\big]\Big\}(\dot{\mathbf{r}}_i-\dot{\mathbf{r}}_j)\end{aligned} \tag{2.6}$$

with $\mathbf{a}_i^{Newt}$ to be the acceleration of body i due to Newtonian effects only and $\mathbf{a}_i^{Rel}$ to be a peculiar contribution of GR, however dependent on the states only, not on their derivatives.

The last group is identified by the sum of these two terms:

$$\underbrace{\frac{1}{2c^2}\sum_{j\neq i}\frac{\mu_j(\mathbf{r}_j-\mathbf{r}_i)}{r_{ij}^3}\big[(\mathbf{r}_j-\mathbf{r}_i)\cdot\ddot{\mathbf{r}}_j\big]}_{①} \qquad \text{and} \qquad \underbrace{\frac{7}{2c^2}\sum_{j\neq i}\frac{\mu_j\ddot{\mathbf{r}}_j}{r_{ij}}}_{②} \tag{2.7}$$

They are both linearly dependent on the acceleration $\ddot{\mathbf{r}}_j$, therefore they are linear in the derivative of the state $\dot{\mathbf{x}}_j$.

The dot product is a linear operator.

The two terms ① and ② are now manipulated, so that a single acceleration-dependent term can be obtained. Particularly, ① can be re-written as:

$$① = \frac{1}{2c^2}\sum_{j\neq i}\frac{\mu_j(\mathbf{r}_j-\mathbf{r}_i)}{r_{ij}^3}\big[(\mathbf{r}_j-\mathbf{r}_i)\cdot\ddot{\mathbf{r}}_j\big] = c_1\sum_{j\neq i}\mathbf{k}_{ij}(\mathbf{h}_{ij}\cdot\ddot{\mathbf{r}}_j) \tag{2.8}$$

and the dot product can be expanded and re-grouped in the following way:

$$\begin{aligned} c_1\sum_{j\neq i}\mathbf{k}_{ij}(\mathbf{h}_{ij}\cdot\ddot{\mathbf{r}}_j) &= c_1\sum_{j\neq i}\mathbf{k}_{ij}(h_{ij}^{(1)}\ddot{r}_j^{(1)} + h_{ij}^{(2)}\ddot{r}_j^{(2)} + h_{ij}^{(3)}\ddot{r}_j^{(3)}) \\ &= c_1\sum_{j\neq i}\left(h_{ij}^{(1)}\mathbf{k}_{ij}\ddot{r}_j^{(1)} + h_{ij}^{(2)}\mathbf{k}_{ij}\ddot{r}_j^{(2)} + +h_{ij}^{(3)}\mathbf{k}_{ij}\ddot{r}_j^{(3)}\right) \\ &= c_1\sum_{j\neq i}\big[h_{ij}^{(1)}\mathbf{k}_{ij} \quad h_{ij}^{(2)}\mathbf{k}_{ij} \quad h_{ij}^{(3)}\mathbf{k}_{ij}\big]\ddot{\mathbf{r}}_j \\ &= c_1\sum_{j\neq i}\mathbf{M}_{ij}^{①}\ddot{\mathbf{r}}_j \end{aligned} \tag{2.9}$$

where the notation $\mathbf{y}^{(n)}$ means the n-th component of the vector $\mathbf{y}$.

Both $\boldsymbol{k}_{ij}$ and $\boldsymbol{h}_{ij}$ are vectors, the double index ij means that they are dependent both on i and j.

② can be re-written as:

$$② = \frac{7}{2c^2}\sum_{j\neq i}\frac{\mu_j\ddot{\mathbf{r}}_j}{r_{ij}} = c_2\sum_{j\neq i}\alpha_{ij}\ddot{\mathbf{r}}_j = c_2\sum_{j\neq i}\alpha_{ij}\mathbf{I}\ddot{\mathbf{r}}_j = c_2\sum_{j\neq i}\mathbf{M}_{ij}^{②}\ddot{\mathbf{r}}_j \tag{2.10}$$

where $\mathbf{I}$ is the identity matrix.

The whole Equation (2.4) can therefore be written as:

$$\ddot{\mathbf{r}}_i = \mathbf{a}_i^{Newt} + \mathbf{a}_i^{Rel} + \sum_{j\neq i}(c_1\mathbf{M}_{ij}^{①} + c_2\mathbf{M}_{ij}^{②})\ddot{\mathbf{r}}_j \tag{2.11}$$

The final form of the equation has been almost reached, nevertheless coupling is still visible among the acceleration. To be able to face this computational issue it is enough to build an *augmented* system for all the N bodies, with quantities:

$$\ddot{\mathbf{r}}_{aug} = \begin{Bmatrix} \vdots \\ \ddot{\mathbf{r}}_i \\ \vdots \end{Bmatrix}; \quad \mathbf{a}_{aug} = \begin{Bmatrix} \vdots \\ \mathbf{a}_i^{Newt} + \mathbf{a}_i^{Rel} \\ \vdots \end{Bmatrix}; \quad \mathbf{M} = \begin{bmatrix} \mathbf{M}_{ij} \end{bmatrix}; \tag{2.12}$$

where the matrix $\mathbf{M}$ contributions are:

$$\mathbf{M}_{ij}{}^{1} = \begin{cases} \underline{\underline{0}} & i = j \\ c_1 \mathbf{M}_{ij}^{①} + c_2 \mathbf{M}_{ij}^{②} & i \neq j \end{cases} \tag{2.13}$$

with the elements composing M_{ij} explicitly defined as:

$$\begin{aligned} &c_1 := \frac{1}{2c^2}; \\ &c_2 := \frac{7}{2c^2}; \\ &M_{ij}^{①} := \begin{bmatrix} h_{ij}^{(1)}\mathbf{k}_{ij} & h_{ij}^{(2)}\mathbf{k}_{ij} & h_{ij}^{(3)}\mathbf{k}_{ij} \end{bmatrix} \\ &= \frac{\mu_j}{r_{ij}^3}\left[(r'(1)_j - r'1)_i)(\mathbf{r}_j - \mathbf{r}_i),\ (r'(2)_j - r'2)_i)(\mathbf{r}_j - \mathbf{r}_i),\ (r'(3)_j - r'3)_i)(\mathbf{r}_j - \mathbf{r}_i)\right]; \\ &\mathbf{M}_{ij}^{②} := \alpha_{ij}\mathbf{I} = \frac{\mu_j}{r_{ij}}\mathbf{I}. \end{aligned} \tag{2.14}$$

The augmented system takes then the form:

$$\begin{aligned} \ddot{\mathbf{r}}_{aug} &= \mathbf{a}_{aug} + \mathbf{M}\,\ddot{\mathbf{r}}_{aug} \\ \Longrightarrow (\mathbf{I} - \mathbf{M})\ddot{\mathbf{r}}_{aug} &= \mathbf{a}_{aug} \end{aligned} \tag{2.15}$$

It is now straight forward to obtain the final state-space formulation

$$\dot{\mathbf{x}}_{aug} = \mathbf{F}(\mathbf{x}_{aug}) \tag{2.16}$$

with the sole difference to simulate the whole augmented state if the purpose of the propagation is to propagate all the N-body trajectories.

Consistency is the only thing that matters when defining $\mathbf{F}$, meaning that $\mathbf{F}(\mathbf{x}_{aug})$ should be defined according to Equation (2.15), assigning the terms of $\mathbf{x}_{aug}$ following their physical meaning, independently on how the elements of the augmented vector are sorted. In any case, all the complexity of the problem has been reduced to the need of just solving a linear system at each step of the propagation.

Note also that no further assumption has been made so far, meaning that the result obtained with the propagation is affected only by the analytical approximations made back in the derivation of the starting

1 $\mathbf{M}_{ij}$, as well as $\mathbf{M}_{ij}^{①}$ and $\mathbf{M}_{ij}^{②}$, is a 3×3 matrix.

equation (parametrised post newtonian mechanics (PPN) formalism, treated in Section B.4) and by the round off errors coming from the numerical propagation.

As final remark, this formulation of the problem is also quite general and flexible: it is true that no other orbital perturbation is considered in this example, but they could easily be included as one of the elements to sum inside $\mathbf{a}_{aug}$, whether they are not dependent on the acceleration of the bodies[2]. Furthermore, the original equation reported in [36] includes also a term called "self-acceleration": the most general type of body is considered there, where the center of mass[3] is self-accelerated if shape and/or density are not spherically symmetric. But again this contribution is not dependent on the acceleration of any of the bodies, hence it can be added in $\mathbf{a}_{aug}$ as well.

2.3 FULLY RELATIVISTIC METHOD

2.3.1 *Implementation*

The computational effort required for a full N-Body propagation is extremely high, thus the model purposed in this work has been tested using MATLAB® and SNAPPSHOT (European Space Agency's planetary protection compliance verification software [11] [18]) the motion of several asteroids, propagating the small body and relying on planet's ephemerides data, i.e. assuming the asteroids having no gravitational influence on the major bodies. The cases of 2006H51, 2010RF12, Apophis and Icarus[4] are reported in this work, in a J2000 reference frame centred on the Solar System barycentre, propagated 100 years forward in time, starting from 1^{st} January 1989 at 12 : 00, with a Runge-Kutta 8 propagator and using the planet's ephemerides available in SPICE [1]. The reason for such long propagations is simply to perform a deep test on the high accuracy reached with including GR, given that the N-body propagation is already good if no close approach is to happen .

This is however proven to be reduced until the flyby date for Apophis (as it can be seen in Figure 2.3).

Since only the asteroids' motion needs to be propagated, it is possible to compute the acceleration of the asteroids with Equation (2.1), after having obtained the accelerations of the N-Bodies.

The validation will be carried out by comparing the propagator results with some benchmark data, thus the errors that will be pre-

2 This usually happens, for example all the oblateness perturbation models and the Solar Radiation Pressure are dependent on the position only.

3 Note that, as already mentioned in Subsection B.4.3, bodies are considered as point masses, like any N-Body model.

4 Those asteroids have been chosen because of their orbital perihelion close to the Sun (thus quite sensitive to GR effects) or because performing a close approach with Earth (thus planetary defence applications justify the interest to be extremely accurate in determining their trajectory).

sented, unless differently specified, are to be considered as computed with respect to each correspondent SPICE's set.

With this method, the accelerations of the N bodies are computed taking into account GR effects directly with the linear system reported in Equation (2.15). It is then solved at each propagation step with the purpose of obtaining the accelerations of the N-bodies, but without propagating their motion[5]. Note that the MATLAB® function `mldivide.m` does not require the user to specify the method used to solve the linear system. On the other hand, a method implementation was needed in SNAPPSHOT since no explicit linear system was solved before implementing GR effects. A thorough inspection showed a positive definite, ill-conditioned (some off-diagonal elements are in the order of $10^{-20} km/s^2$) and non-symmetric associated matrix, which thus led to the implementation of an LU factorisation with partial pivoting, in order to avoid a too small element to become pivot, and consequent forward and backward substitutions [22].

2.3.2 *Propagation and results*

The results of the propagation without taking into account GR are first presented. They are reported as distances from Mercury (2006HY51 and Icarus) or Earth (Apophis and 2010RF12), in Figures 2.1, 2.2, 2.3, 2.4 respectively. Looking at the order of magnitude of the distances

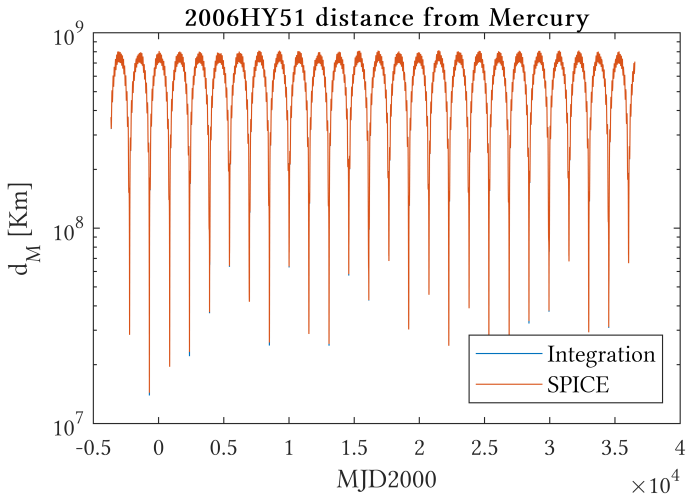

Figure 2.1: Order of magnitude of the distance between 2006HY51 and Mercury, N-body accelerations only.

from Mercury for both the asteroids 2006HY51 and Icarus, there seems to be almost no difference between the N-body propagation and SPICE's data (Figures 2.1 and 2.2). In the Apophis case (Figure 2.3)the difference becomes rather high, particularly after the flyby of Earth, whereas for 2010RF12 (Figure 2.4) a difference with respect to

5 Their position and velocity come always from ephemerides data.

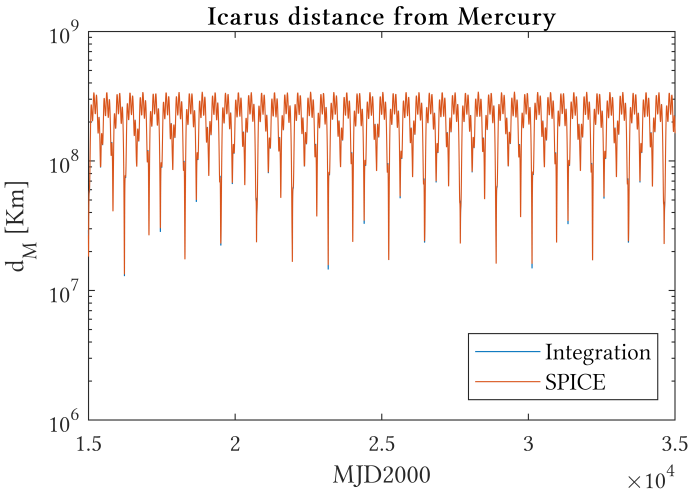

Figure 2.2: Order of magnitude of the distance between Icarus and Mercury, N-body accelerations only.

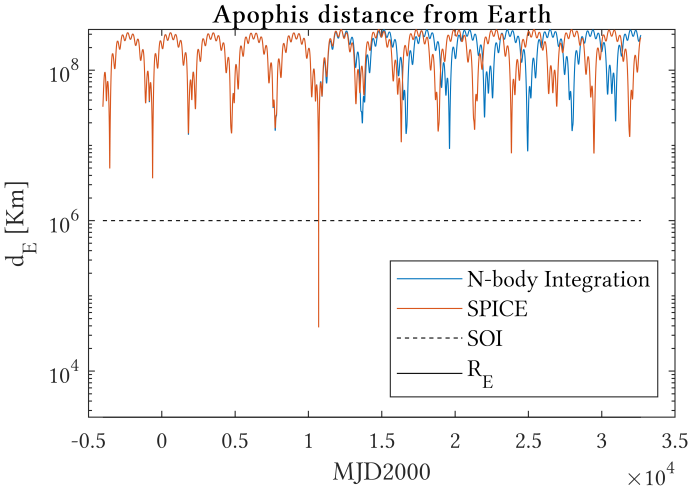

Figure 2.3: Order of magnitude of the distance between Apophis and Earth, N-body accelerations only.

SPICE's data can be seen, but after the second flyby of Earth and not as high as for Apophis.

It can be observed that, as expected, any flyby produces a sudden growth of the error and the uncertainty of the propagation, nevertheless this may be indeed due to be yet to include in the propagation GR effects.

The results of the propagation with GR are presented for Apophis and 2010RF12 in Figures 2.5 and 2.6, looking for some improvements of the N-body results.

The propagation results have become quite good for Apophis (Figure 2.5), with still a small difference left which however doesn't affect the next close approach dates, in any case better than what reported

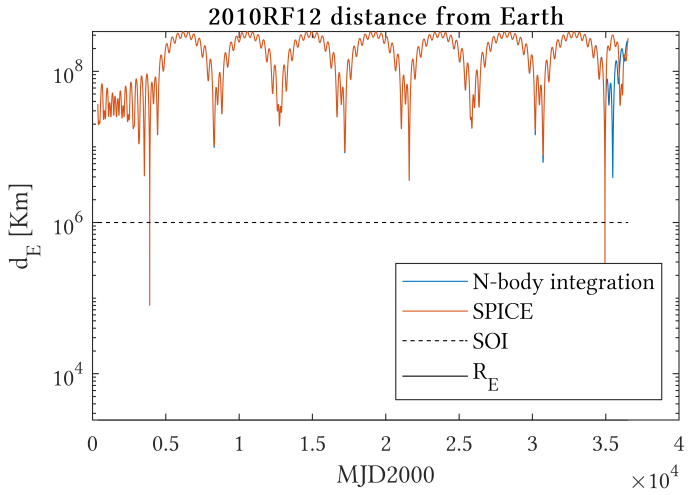

Figure 2.4: Order of magnitude of the distance between 2010RF12 and Earth, N-body accelerations only.

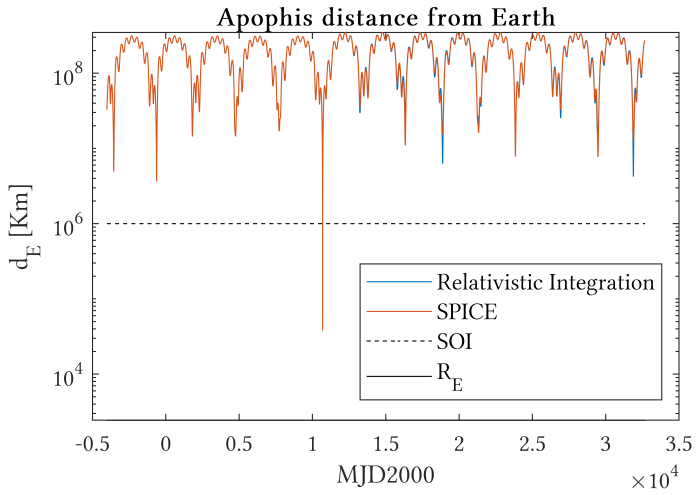

Figure 2.5: Order of magnitude of the distance between Apophis and Earth, general relativity effects added.

in Figure 2.3). For 2010RF12 the improvement is visible only after its second flyby of Earth (Figure 2.6.)

Note that, as it can be seen in Figures 2.1 and 2.2, the N-body propagation is already enough for the order of magnitude analysis, therefore their new distances are not reported again, because no actual improvement would be seen in those graphical representation.

A precise study of the error behaviour is then carried out, with the purpose of understanding properly where the difference on the model has actually made the biggest improvement on the results. The comparison between the position errors are reported in Figures 2.7, 2.8, 2.9, 2.10. The velocity errors have been computed as well in all the cases, for the sake of conciseness they are not included in this

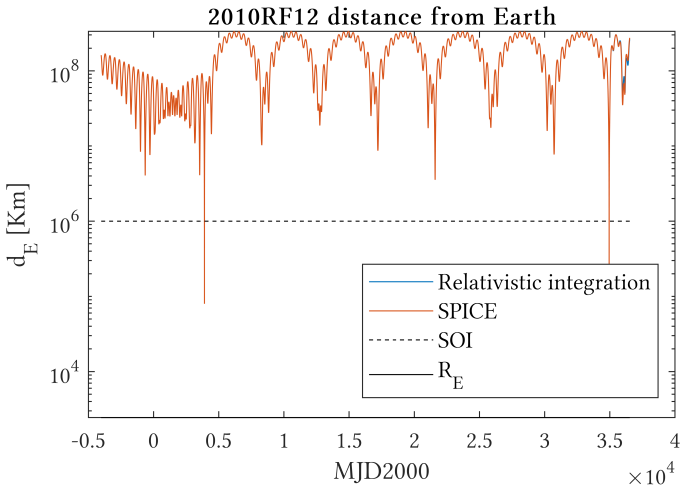

Figure 2.6: Order of magnitude of the distance between 2010RF12 and Earth, general relativity effects added.

work since they have always been showing the same behaviour of the position errors.

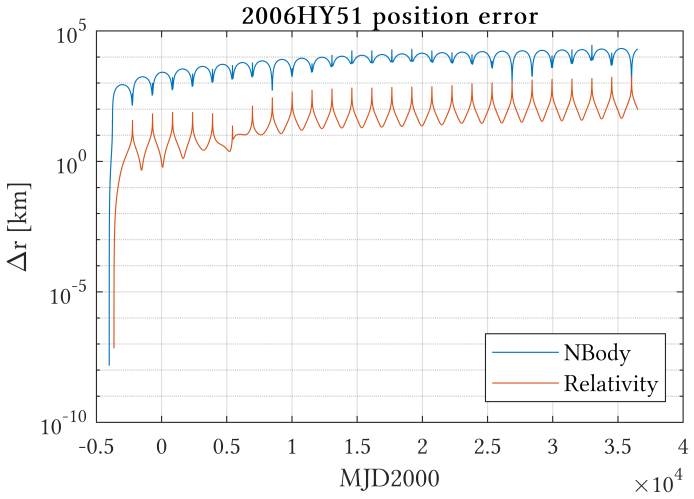

Figure 2.7: 2006HY51, position error.

Despite it was not visible in Figures 2.1 and 2.2, there actually is an improvement even for these asteroid if GR is taken into account. The same observation can be made: over a 100 years propagation, the reduction on the error is experienced to be of at least one order of magnitude, because of the combined effects of the model being improved and, as a consequence, of a lower error to be propagated.

A sudden increase of the error, as expected, is experienced while performing the flyby for both Apophis and 2010RF12 (Figures 2.9 and 2.10 respectively). However, the improved model due to GR allows this time to still have quite an accurate prediction of the motion after the event. For the particular case of 2010RF12, the error when accounting

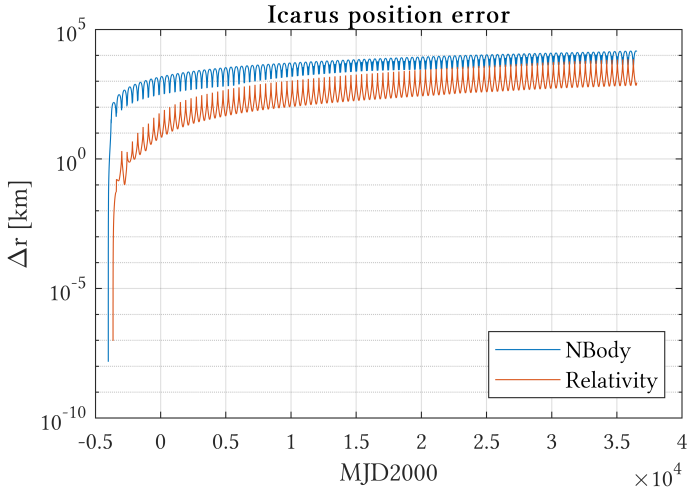

Figure 2.8: Icarus, position error.

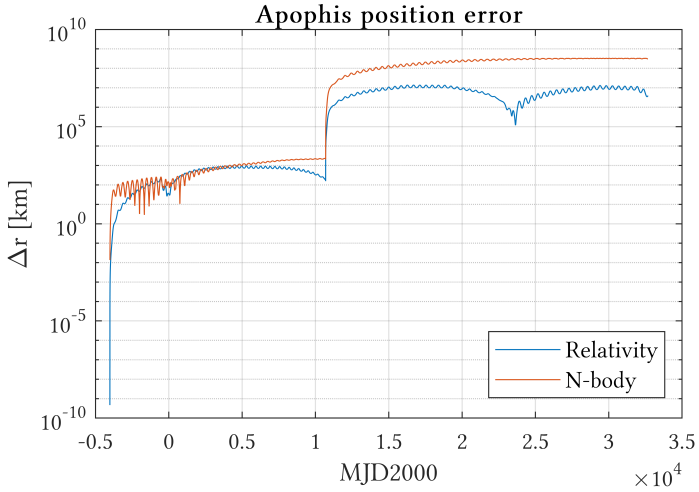

Figure 2.9: Apophis, position error.

for GR effects is observed to be lower than the N-body propagation even before the 2nd flyby, despite it did not seem so by comparing Figures 2.6 and 2.4.

2.3.3 *Orbital element analysis*

Semi-major axis, eccentricity, inclination, right ascension of the ascending node, perihelion anomaly and true anomaly respectively

To give stronger support to the accuracy of the model, an analysis on the orbital elements $(a, e, i, \Omega, \omega, \theta)$ (obtained by converting each state $(\mathbf{r}, \dot{\mathbf{r}})$ coming from the cartesian propagation) is performed with and without taking into account GR. Particularly, the results are reported zoomed at the end of the propagation (where the accumulated error makes the differences more visible) and in terms of ω[6] only for 2006HY51 (Figure 2.11) and Icarus (Figure 2.12). All the other

6 The perihelion drift is the most significant effect of GR for near-Sun objects.

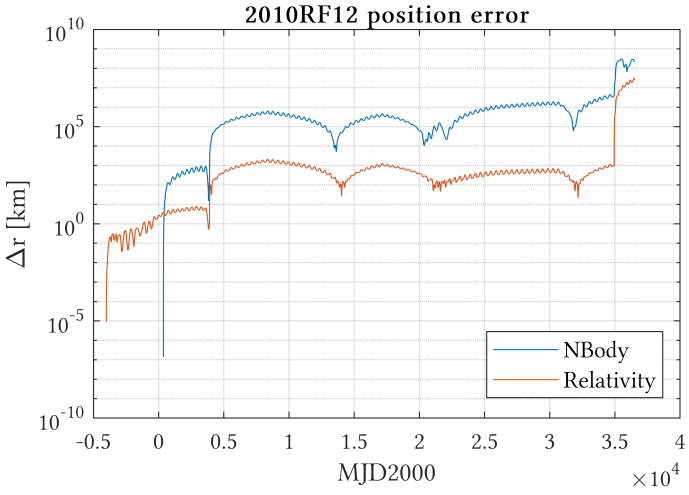

Figure 2.10: 2010RF12, position error.

elements have been tested but not reported, since showing the very same behaviour of the presented ones.

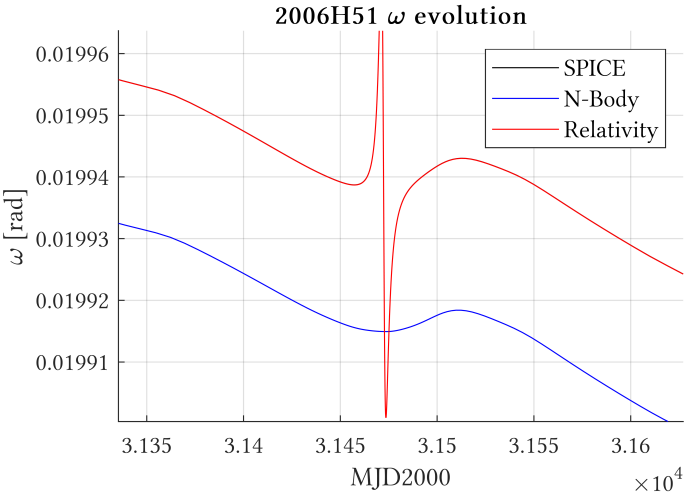

Figure 2.11: 2006HY51, perihelion anomaly variation.

For 2006HY51 and Icarus (Figures 2.11 and 2.12) it can be seen that now the model is capable of tracking even the smallest variations on the orbital parameters, with almost no difference compared to SPICE's data.

About Apophis, all the elements experience a sudden change due to the close approach. The time history of a is reported in Figure 2.13, whereas all the other elements, again for the sake of conciseness, are not reported in the analysis since showing the very same behaviour. The difference was already significant even before the flyby, with an oscillating behaviour from the N-body propagation pretty different than the ephemerides data.

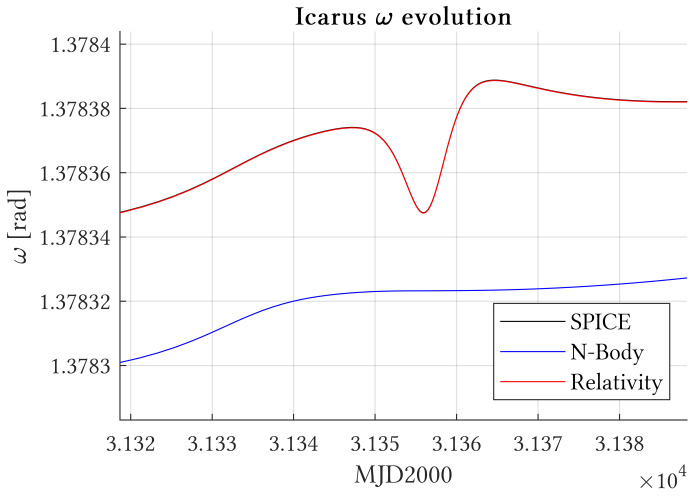

Figure 2.12: Icarus, perihelion anomaly variation.

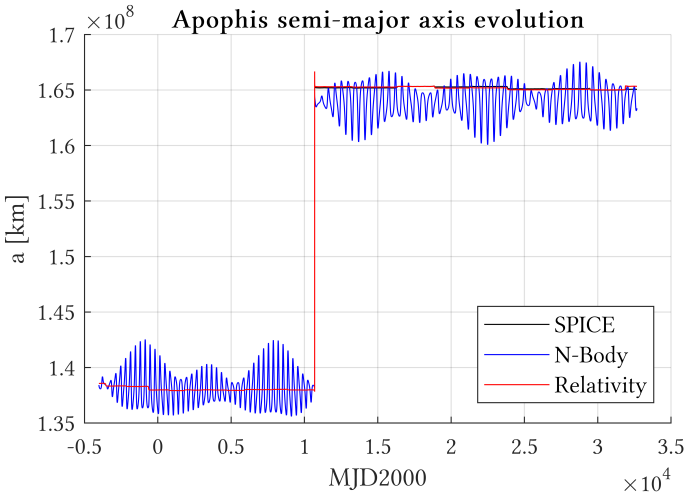

Figure 2.13: Apophis, semi-major axis variation

The eccentricity variation of 2010RF12 is presented in Figure 2.14, with again all the other elements to follow the same trend and not included here. What happens at the second flyby is highlighted. Accounting for GR effects has now kept the elements close to the ephemerides data, whereas the N-body model would have led to a completely different result.

As a final comment about what observed with orbital elements and errors, despite the differences being small between ephemerides and GR propagation, note that all the distances involved are quite high in their absolute value. Even a tiny variation in α or θ can easily lead to positions remarkably different one another.

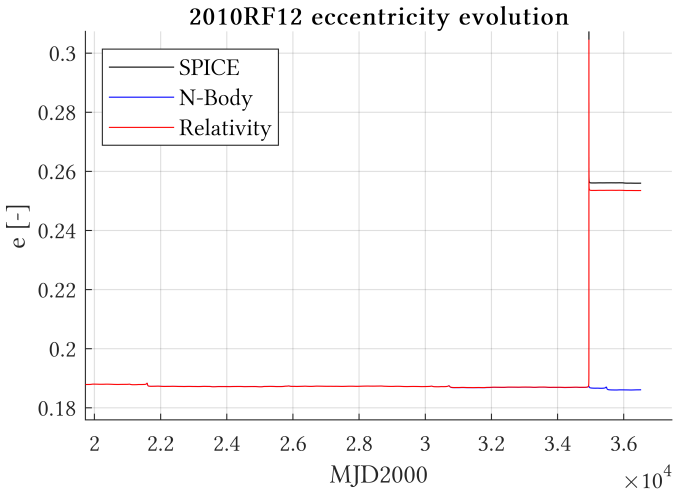

Figure 2.14: 2010RF12, eccentricity variation

2.4 NEWTONIAN N-BODY ACCELERATIONS METHOD

For the sake of reducing the computational cost but still obtaining an accurate result, it may be worth to look for a suitable approximation that allows to avoid, even if linear, to solve the system reported in Equation (2.15) at each iteration. This can actually be done when one wants to rely on data from ephemerides about the N-bodies and not to propagate the full N-body motion, namely avoiding to compute the N-body accelerations required to apply the model presented in the previous sections.

2.4.1 *Rigorous definition*

An order-of-magnitude-based proof is then proposed in the following lines: Equation (2.11) written for a mass particle p, that has no gravitational influence on the body i, is:

$$\ddot{\mathbf{r}}_p = \mathbf{a}_p^{Newt} + \mathbf{a}_p^{Rel} + \sum_i \mathbf{M}_{ip}\ddot{\mathbf{r}}_i \tag{2.17}$$

where:

- $\mathbf{a}_p^{Newt}$ is the Newtonian Acceleration on the mass p due to bodies i, hence of order $O(1)$;
- $\mathbf{a}_p^{Rel}$ is what was the relativistic vector contribution in Equation (2.11), but for the mass p due to the bodies i; thus it is of order $O(1/c^2)$;
- The quantity $\mathbf{M}_{ip}$ embeds a reduction of $1/c^2$, recalling its definition in Equations (2.13) and (2.14).

It follows that any acceleration, including the body i, can be seen as:

$$\ddot{\mathbf{r}}_i = \underbrace{\mathbf{a}_i^{Newt}}_{O(1)} + \underbrace{\mathbf{a}_i^{Rel}}_{O\left(1/c^2\right)} + \underbrace{\sum_{i \neq j} \mathbf{M}_{ij} \left[\mathbf{a}_j^{Newt} + O\left(1/c^2\right)\right]}_{O\left(1/c^2\right)} \tag{2.18}$$

Note that the actual purpose of the relativistic corrections is to reach a level of accuracy up to $O\left(1/c^2\right)$: multiplying the acceleration by $\mathbf{M}_{ij}$ is then providing a term $O\left(1/c^2\right)$ from the Newtonian part, and a term $O\left(1/c^4\right)$ from all the other contributions.

Therefore, if there is no need of propagating the full relativistic N-body problem, it is reasonable to use

$$\ddot{\mathbf{r}}_p \approx \mathbf{a}_p^{Newt} + \mathbf{a}_p^{Rel} + \sum_i \mathbf{M}_{ip} \mathbf{a}_i^{Newt} \tag{2.19}$$

with the consequence of not needing to solve the augmented system of Equation (2.15) to obtain the full accelerations of the N-bodies providing the gravitational field, but applying directly Equation (2.19) to obtain the small body's acceleration.

2.4.2 *Results*

The numerical integration performed with this method has a reduced computational cost 3 times lower than the fully relativistic propagation. About the cases presented here on the order of 6 vs 2 minutes for 2006HY51 and Icarus, 10 vs 3.5 minutes for Apophis and 15 vs 5 minutes for 2010RF12, all computed with a Runge Kutta RK7(8) [22] method, run on MATLAB® in a local machine, on a single CPU at 2.7GHz. Accurate results are obtained anyway, as it can be observed in Figures 2.15 and 2.16 for the most critical cases analysed, the flyby asteroids Apophis and 2010RF12 respectively. The position errors are reported in Figures 2.17 and 2.18, with the error again not included since showing exactly the same behaviour.

Looking at the order of magnitude of the distance Apophis-Earth (Figure 2.15), no difference is visible and the flyby seems not to be critical with this approximated method. A similar situation happens for 2010RF12 (Figure 2.16), with a deviation slightly increased after the second flyby.

For Apophis error with respect to SPICE data is very similar to the fully relativistic case (Figure 2.17), whereas the error between the two relativity methods stays more or less constant over the propagation. Note that these two errors have been plotted on the same graphs to highlight what particularly happens for 2010RF12 (Figure 2.18): the situation is again similar to the Apophis until the second flyby is reached, here the error increases, with the fully relativistic model this time staying closer to SPICE's data.

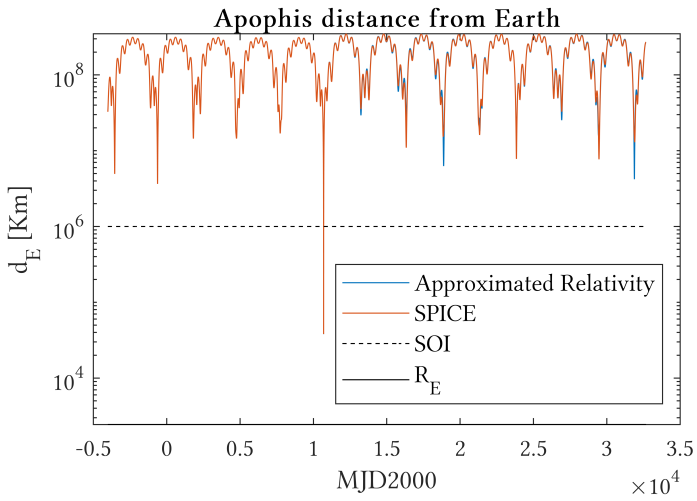

Figure 2.15: Order of magnitude of the distance between Apophis and Earth, approximated general relativity effects.

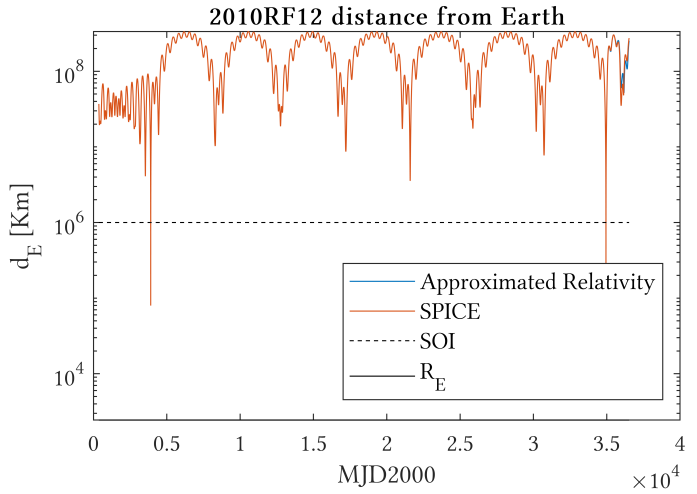

Figure 2.16: Order of magnitude of the distance between 2010RF12 and Earth, approximated general relativity effects.

The maximum values of the error have been observed to be in both the cases more or less of 0.005% of the magnitude of the problem. This value however increases enormously after the second flyby for the case of 2010RF12, with the maximum value of the error between the two propagations reaching an order of 20% of the reference magnitude. This can be considered due to the amplifying effect of the close approach on the error, as well as the increased uncertainty that is always propagated.

The orbital element analysis is not reported for this method, because the results would not be distinguishable from the fully relativistic propagation treated in Section 2.3.

As a final remark about this approximated method, note that the actual impact on the propagation is that small only because all the

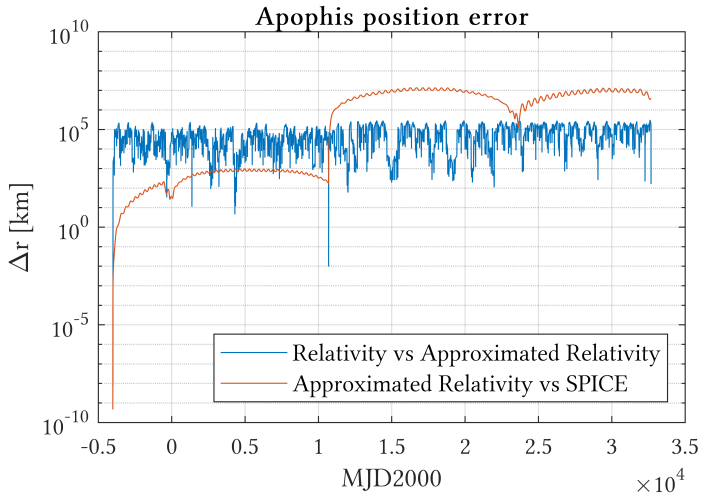

Figure 2.17: Apophis, position error comparison between general relativity models.

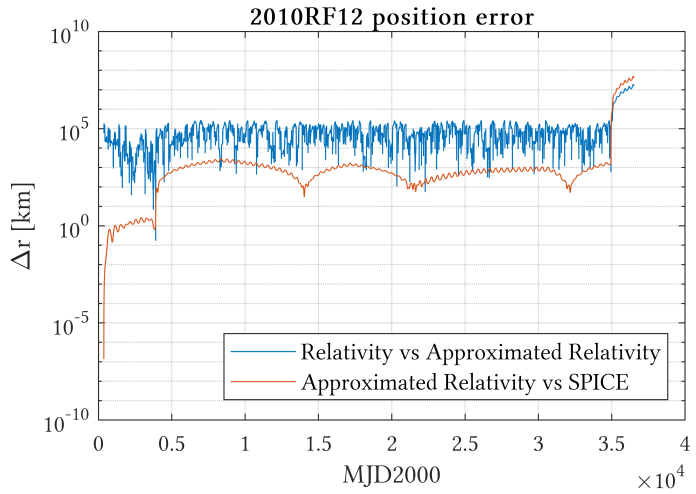

Figure 2.18: 2010RF12, position error comparison between general relativity models.

accelerations are scaled by the factor c^2. In a full N-body propagation they have a direct impact on the future position and velocity, thus quite a significant error accumulation can be expected whether propagating with the acceleration-approximated method.

3

CONCLUSION AND OUTLOOK

The study and research of methods to take into account GR in the N-body propagation are now over, with two consistent methods proven to be solid and robust. The first one, the fully relativistic propagation, is an approach suitable even for the ephemerides generation, since it does not embed any assumption that is not coming from the PNM model derivation and can be, as already discussed at the end of Section 2.2, easily generalised to take into account many other effects and contributions.

The first method looks gives always the best results, even if propagating a simple mass assumed as having no influence on the other N-bodies. The computational cost is high, but not so high in fact, given the results and the robustness that it provides: on this regard, it has been crucial to rely completely on the numerical propagation already needed for the N-body case to implement the equation of motion. This allowed to formulate the problem just as the solution of an augmented linear system (Equation (2.15)) at each time step for the computation of the accelerations up to machine precision, without any further loss of generality and accuracy.

The difference between this general method and the Newtonian-acceleration approximated one (described in Section 2.4) does however highlight that precise results can be achieved even with a simplified approach, paying just a slightly reduced accuracy to have a computational cost way lower than the fully relativistic propagation (the computational performances had been compared in Section 2.4). This last method has however proven itself to have a reduced robustness when a second flyby occurred, in the 2010RF12 case (Figures 2.6 2.16 and 2.18). Hence, it may be used and trusted whether no particular event is expected during the propagation, where the sudden growth of the error due to flyby events is not experienced.

Model and propagation method can both be improved, implementing other perturbation sources (i. e. J2 oblateness and solar radiation pressure, for instance) and studying the uncertainty propagation, for the sake of reaching a model where, ideally, this last element is the only error source. They have not been included in this work, since the goal was only to study the peculiar effects of GR in an interplanetary sense, although their implementation would be straight forward.

As a final remark, a suitable benchmark has been built and can be used to test and study other orbital models. In the following parts of this work such a benchmark will be used not only to test the approximations made in the model derivations, but also to compute and apply corrective coefficients to improve the model's precision.

Part II

B-PLANE ORBITAL RESONANCE THEORY

4

TWO BODY B-PLANE RESONANCE THEORY

4.1 INTRODUCTION

As a takeaway from the previous part of this work, the reader should now be aware of how crucial it is to have a proper model to study the flybys and their future consequences: for instance, Apophis' remarkably deep close encounter with Earth (Figure 2.5) can be predicted quite ahead in time, nevertheless one should still wonder whether a next, consequent close approach occurred.

Remaining within the patched conics context[1], there indeed exists an analytical theory that attempts to setup a first model for *orbital resonances*. Such a framework had been developed based on Öpik's variables[2] [14] first in [9], deepened in [29] and then finalised in [30], whose geometry and concepts will be recalled and described with a deep level of detail in the upcoming sections.

4.2 CLOSE ENCOUNTER GEOMETRY

Assuming the planet to follow a circular orbit around the Sun, the reference frame of analysis (Figure 4.1) was first introduced in [9]. Referring all the quantities to the flyby planet, the system is centred on the planet's centre of mass, the x axis is directed as the heliocentric position, the y axis as the heliocantric velocity $\mathbf{v}_p$ and z as the heliocentric angular momentum.

The remaining quantities presented in Figure 4.1 stand for the ingoing and outgoing planetocentric velocities $\mathbf{U}$ and $\mathbf{U}'$, the respective spherical angles θ and θ' with respect to the planet's velocity, ϕ and ϕ' to locate the correspondent maximum circles with respect to the one on the plane (y, z). The deflection magnitude is identified by γ (i.e. the turn angle) and the direction by ψ, given as the internal angle between the sides γ and θ of the spherical triangle $\theta\gamma\theta'$, formed by the vectors $\mathbf{U}$, $\mathbf{U}'$ and $\mathbf{v}_p$ ([9], [30]). Note that the flyby effect, interplanetary-wise

1 There are other resonance models and applications which make use of different assumptions and environments, that will be better mentioned in Part iii.

2 The six elements used to describe the orbital motion will be mentioned in the following sections.

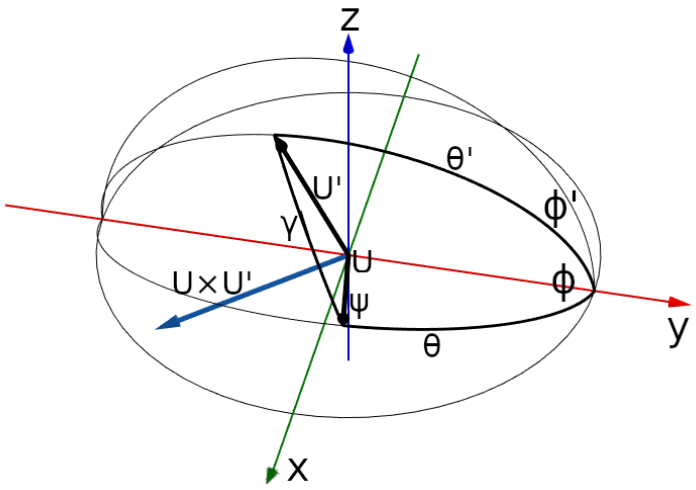

Figure 4.1: Deflection reference frame introduced by [9].

in any patched conics approximation, is modelled as an instantaneous rotation of the vector **U**.

Identifying by (a, e, i) the non-dimensional semi-major axis, eccentricity and inclination of the small object's orbit, the components of **U** can be written as ([9],[30]):

$$\mathbf{U} = \begin{bmatrix} U_x \\ U_y \\ U_z \end{bmatrix} = \begin{bmatrix} \pm\sqrt{2 - 1/a - a(1-e^2)} \\ \sqrt{a(1-e^2)}\cos i - 1 \\ \pm\sqrt{a(1-e^2)}\sin i \end{bmatrix} \tag{4.1}$$

where the reference length is the distance planet-Sun, the reference time is the planet's orbital period divided by 2π and the Sun's gravitational parameter is set to 1. In this a way also the planet's velocity magnitude is equal to 1 [30].

Identifying with T the Tisserand parameter the magnitude $U = \|\mathbf{U}\|$ becomes:

$$U = \sqrt{3 - \frac{1}{a} - 2\sqrt{a(1-e^2)}\cos i} = \sqrt{3 - T} \tag{4.2}$$

U can be also expressed as function of the angles θ and ϕ:

$$\begin{bmatrix} U_x \\ U_y \\ U_z \end{bmatrix} = \begin{bmatrix} U\sin\theta\sin\phi \\ U\cos\theta \\ U\sin\theta\cos\phi \end{bmatrix} \tag{4.3}$$

which then suggests the following definition for such angles

$$\begin{bmatrix} \cos\theta \\ \tan\phi \end{bmatrix} = \begin{bmatrix} U_y/U \\ U_x/U_z \end{bmatrix} \tag{4.4}$$

4.3 THE B-PLANE REFERENCE FRAME

With the above defined quantities it is possible to introduce the *b-plane* reference frame, whose axes $(\hat{\xi}, \hat{\eta}, \hat{\zeta})$ are defined as [14]:

$$\eta = \frac{\mathbf{U}}{\|\mathbf{U}\|}; \qquad \xi = \frac{\mathbf{U} \times \mathbf{v}_p}{\|\mathbf{U}\| \ \|\mathbf{v}_p\|}; \qquad \zeta = \xi \times \eta. \tag{4.5}$$

Note that the components of such axes identify a rotation matrix to express a generic point $\mathbf{x}_{car}$ of the cartesian space[3] into *b-plane* coordinates:

$$\mathbf{x}_{b-plane} = [\hat{\xi}, \hat{\eta}, \hat{\zeta}]^T \mathbf{x}_{car}. \tag{4.6}$$

From now on the definition *b-plane* will be used to identify the plane perpendicular to the $\hat{\eta}$ axis, because

$$\xi^2 + \zeta^2 = b^2 \tag{4.7}$$

with b the impact parameter [20]. Each of the coordinates has its own physical meaning [5]:

- $\hat{\eta}$ is directed as the planetocentric velocity, thus η stands for some distance measure with respect to the pericentre of the planetocentric hyperbolic orbit. In fact it is there that $\eta = 0$ because of the velocity vector being normal to the planetocentric position, for negative and positive η values in the ingoing and outgoing arcs respectively.
- $\hat{\zeta}$ is directed opposite to the projection on the b-plane of $\mathbf{v}_p$, therefore ζ identifies the phasing of the two orbits.
- $\hat{\xi}$ completes the right-handed reference frame, the coordinate ξ highlights the minimum distance between the two orbits.

Such physical meanings allow then to separate the flyby features into three different coordinates, i.e. what is missing for the small body to impact with the planet could be just a matter of time (η), the two orbits never intersecting each other or their minimum distance being higher than the planet's radius (ξ), the phasing of the two orbits (ζ) or a combination of the three.

Now all the six Öpik's variables [14] have been introduced, thus summarising them:

1. the magnitude U of the planetocentric velocity;
2. the angle θ (Figure 4.1);
3. the angle ϕ (Figure 4.1);
4. the b-plane coordinate ξ;

3 Provided that it is written in the same reference frame of the *b-plane* axes

5. the b-plane coordinate ζ;
6. the time of b-plane crossing t_b, i.e. strictly linked to the third coordinate η.

The b-plane coordinates and the impact parameter provide a straight forward definition of the deflection direction angle ψ ([9],[30]):

$$\begin{bmatrix} \xi \\ \zeta \end{bmatrix} = \begin{bmatrix} b \sin\psi \\ b \cos\psi \end{bmatrix} \tag{4.8}$$

and introducing the quantity $c = m/U^2$, where m is the planet's mass expressed in solar masses, γ can be identified as:

$$\tan\frac{\gamma}{2} = \frac{m}{bU^2} = \frac{c}{b} \tag{4.9}$$

or

$$\begin{aligned} \cos\gamma &= \frac{b^2 - c^2}{b^2 + c^2} \\ \sin\gamma &= \frac{2bc}{b^2 + c^2}. \end{aligned} \tag{4.10}$$

Recalling Figure 4.1, the deflection can be then determined by solving the spherical triangle $(\theta, \gamma, \theta')$, with ψ acting as internal angle, thus obtaining the new orientation θ'. The cosine law for spherical geometry gives [30]:

$$\cos\theta' = \cos\theta\cos\gamma + \sin\theta\sin\gamma\cos\psi. \tag{4.11}$$

4.4 RESONANT CIRCLES FORMULATION

Following [30], by combining Equations (4.4), (4.1) and (4.2), $\cos\theta$ can be expressed in terms of the orbital parameters to obtain:

$$\cos\theta = \frac{\sqrt{a(1-e^2)}\cos i - 1}{\sqrt{3 - \frac{1}{a} - 2\sqrt{a(1-e^2)}\cos i}} \tag{4.12}$$

Taking the square of Equation (4.2) it can be highlighted that

$$\sqrt{a(1-e^2)}\cos i = \frac{3 - 1/a - U^2}{2} \tag{4.13}$$

thus plugging such an expression from Equation (4.13) into Equation (4.12), a new definition for $\cos\theta$ is obtained:

$$\begin{aligned} \cos\theta &= \frac{\frac{3-1/a-U^2}{2} - 1}{\sqrt{3 - \frac{1}{a} - (3 - 1/a - U^2)}} \\ &= \frac{3/2 - 1/2a - U^2/2 - 1}{U} \\ &= \frac{3 - 1/a - U^2 - 2}{2U} \\ &= \frac{1 - 1/a - U^2}{2U} \end{aligned} \tag{4.14}$$

A definition of resonance needs now to be introduced: a flyby leads to a resonant return when the new small object's interplanetary orbit (with superscript ′) satisfy the condition [30]

$$h t'_{obj} = k t_{pl} \tag{4.15}$$

with t to identify the orbital period and (k, h) positive integers, respectively the number of orbits of planet and small object until the next close approach. Note that in the considered reference frame the planet's non-dimensional orbital period $t_{pl} = 2\pi$ and the small object's one is linked to the new interplanetary orbit semi-major axis by $t'_{obj} = 2\pi a'^{3/2}$. Therefore, a resonant post encounter semi-major axis can be determined just by k and h [30]:

A 0 subscript is added to remark the resonance feature of this new orbit

$$a'_0 = \left(\frac{k}{h}\right)^{2/3} \tag{4.16}$$

In theory, from Equation (4.16), there can be infinite resonances with each one featuring its own semi-major axis, however the interest lies only on rather small values of k and h to not push the analysis pointlessly too much forward in time.

Taking now a look to Equation (4.14), it can be seen that the resonant condition turns into a specified orientation θ'_0 of $\mathbf{U}'$ with respect to $\mathbf{v}_p$:

$$\cos\theta'_0 = \frac{1 - 1/a'_0 - U^2}{2U} \tag{4.17}$$

This post encounter angle must satisfy the deflection equation (Equation (4.11)). Plugging the expressions for $\cos\gamma$, $\sin\gamma$, $\cos\psi$ from Equations (4.10) and (4.8) into Equation (4.11) $\cos\theta'_0$ becomes [30]:

$$\cos\theta'_0 = \frac{b^2 - c^2}{b^2 + c^2}\cos\theta + \frac{2c\zeta}{b^2 + c^2}\sin\theta \tag{4.18}$$

and re-arranging to write explicitly ζ:

$$\zeta = \frac{(b^2 + c^2)\cos\theta'_0}{2c\sin\theta} - \frac{(b^2 - c^2)\cos\theta}{2c\sin\theta} \tag{4.19}$$

As already mentioned, a key b-plane feature sees $b^2 = \xi^2 + \zeta^2$. Then

$$\begin{aligned} 2c\sin\theta\zeta &= (\xi^2 + \zeta^2)\cos\theta'_0 + c^2\cos\theta'_0 - (\xi^2 + \zeta^2)\cos\theta + c^2\cos\theta \\ &= (\xi^2 + \zeta^2)(\cos\theta'_0 - \cos\theta) + c^2(\cos\theta'_0 + \cos\theta) \end{aligned} \tag{4.20}$$

Which once re-arranged becomes the resonant circle equation proposed in [30]:

$$\begin{aligned} &\xi^2 + \zeta^2 - \frac{2c\sin\theta}{\cos\theta'_0 - \cos\theta}\zeta + \frac{c^2(\cos\theta'_0 + \cos\theta)}{\cos\theta'_0 - \cos\theta} = 0 \\ &\qquad\qquad \Longleftrightarrow \\ &\xi^2 + \zeta^2 - 2D\zeta + D^2 = R^2 \end{aligned} \tag{4.21}$$

with

$$D = \frac{c \sin\theta}{\cos\theta'_0 - \cos\theta} \qquad R = \left| \frac{c \sin\theta'_0}{\cos\theta'_0 - \cos\theta} \right| \tag{4.22}$$

Specifically, those geometrical entities are circles on the b-plane, whose centre is located on the $\hat{\zeta}$ axis at a coordinate D and whose radius is equal to R (e.g. Figure 4.2).

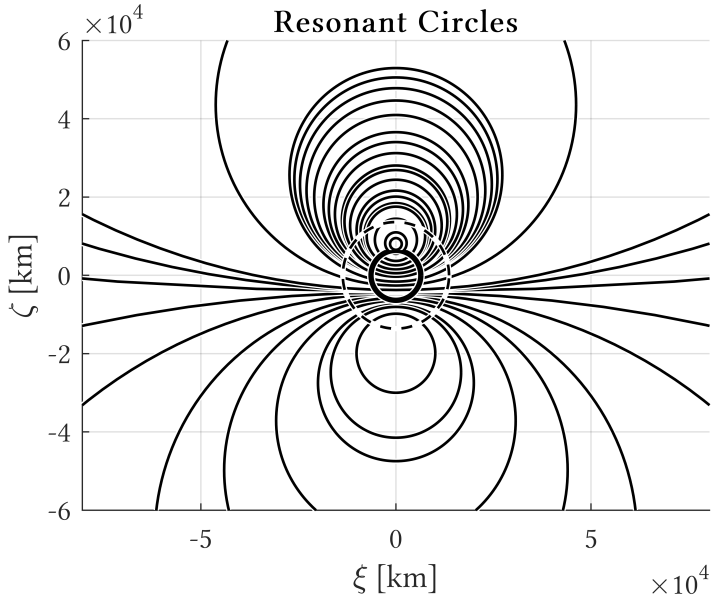

Figure 4.2: Example of set of resonant circles in the b-plane; the thicker solid and dashed lines represent, in this case, respectively Earth's radius and augmented radius due to gravitational focusing.

Note that the most general concept of circle on the b-plane is linked only to a specified post-encounter semi-major axis, without necessarily having it resonant. To this extent, there may exist a flyby whose encounter only changes eccentricity and inclination preserving the semi-major axis, with the consequence of $\cos\theta = \cos\theta'$. The circle parameters do not exist in this case, taking the limit as in [30] the locus of points with such an unchanged semi-major axis is the straight line parallel to the $\hat{\xi}$ axis identified by the equation

$$\zeta = \frac{c \cos\theta}{\sin\theta} \tag{4.23}$$

This is already a quick visual information provided by the b-plane, useful to already classify the close approach.

Note also that (Figure 4.1) the angle θ is bounded between 0 and π, thus $\sin\theta \geqslant 0 \ \forall \ \theta$. Recalling the definition for $\cos\theta'$ in Equation (4.16), as in [30] it can be seen that $a' > a$ implies $\cos\theta' > \cos\theta$, therefore a positive value for the parameter D of all the circles satisfies $a' > a$. This then implies that all the circles with $D > 0$ will be included in the semi-plane $\zeta > \cos\theta / \sin\theta$ and will lead to a post encounter semi-major axis higher than the pre-encounter one [30]. Note that such a consequence is not exactly the rule leading-side/trailing

side flybys, since depending on the sign of $\cos\theta/\sin\theta$ slightly trailing-side close approaches may see a slight reduction in the semi-major axis, and vice-versa.

5

RESONANT BELTS AND PERTURBED CIRCLE PARAMETERS: A SEMI-ANALYTICAL MODEL

5.1 INTRODUCTION

The research performed in this thesis work led to a semi-analytical extension of the theory presented in Chapter 4, by introducing some corrective effects in order to make the b-plane deflection compliant with simulated data. The main perturbing effects are taken into account as happening only inside the sphere of influence, and despite the corrections start to improve the model in that specific direction, the overall assumption remains still the patched conics reference frame. The proposed model will be shown already suitable for a precise treatment of any deflection inside the planet's sphere of influence, nevertheless, to reach its final form, such a semi-analytical theory must detach from the patched conics method to embed a continuous study along the whole and most general orbital motion.

Indeed, the correction seeks to replicate the deflection that the trajectory experiences when undergoing any possible perturbation, although such a deflection is used instead of the patched conics' one in the b-plane analysis.

5.2 FROM RESONANT CIRCLES TO RESONANT BELTS

First of all, it might be worth to introduce a slightly more general concept of resonance than in [30][1], to take into account also non-perfectly phased return as resonant one. Recalling Equations (4.15) and (4.16), as in [11] a *quasi-resonance* definition can be introduced, i.e. an object is considered in resonance with a given planet whether the condition for a generic resonance k/h

$$\left| \frac{T_{object}/T_{planet} - k/h}{k/h} \right| \leqslant \Delta^* \tag{5.1}$$

is satisfied, with the quantity Δ^* to be an arbitrary value identifying the quasi-resonance thresholds.

For instance, $\Delta^* = 0.005$ in [11]

Such a definition can be conceptually reverted, in order to obtain the values of k/h that correspond to the quasi-resonance boundaries:

$$\frac{k}{h}^{\pm} = \frac{k}{h}(1 \pm \Delta^*) \tag{5.2}$$

1 The concept of resonance will select some specific semi-major axes, albeit the same considerations can be made for a general post encounter semi-major axis.

Re-applying Equation (4.16) two new quasi-resonant post encounter semi-major axes can be obtained

$$a_0'^{\pm} = \left(\frac{k}{h}^{\pm}\right)^{2/3} \tag{5.3}$$

to bring two new values for $\cos\theta_0'$, as it was in Equation (4.17)

$$\cos\theta_0'^{\pm} = \frac{1 - 1/a_0'^{\pm} - U^2}{2U} \tag{5.4}$$

and eventually obtain the parameters of two new circles as defined in Equation (4.22):

$$D^{\pm} = \frac{c\sin\theta}{\cos\theta_0'^{\pm} - \cos\theta} \qquad R^{\pm} = \left|\frac{c\sin\theta_0'^{\pm}}{\cos\theta_0'^{\pm} - \cos\theta}\right| \tag{5.5}$$

These two new circles bound a closed region, the locus of points in the b-plane satisfying the quasi-resonance condition, from now on called *resonant belts* (e.g. Figure 5.1).

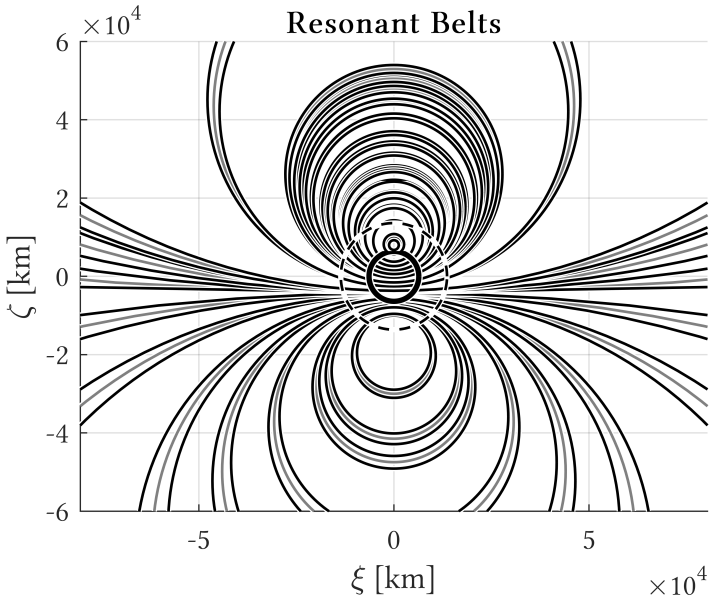

Figure 5.1: Resonant belts from the same example of Figure 4.2. The correspondent perfect resonances (i.e. resonant circles) are reported in grey.

5.3 CIRCLE MODIFICATION DUE TO PERTURBING EFFECTS

The current section will introduce perturbing effects in the computation of the resonant circle parameters, due to the actual trajectory slightly differing from the patched conics approximation. Note that whatever presented in the upcoming lines has to be intended as applicable to any of the circles, thus for both the perfect resonance and

the boundaries of the resonant belts, as well as to any other arbitrary post-encounter semi-major axis.

A set of perturbing parameters will be introduced, all meant to be computed by the results of numerical simulations.

5.3.1 *Perturbation effects in the planetocentric motion*

Some work to model perturbing effects in hyperbolic trajectories has already been made, particularly what developed by [3] presents an analytical solution for perturbing angles in a formalism close to Öpik's variables [14], by means of the Born approximation. Some inspiration has been taken from [3] on how to handle the geometry, even though the perturbing coefficients are kept as general, in order to be suitable for both a numerical computation and possible future analytical developments.

Starting with the perturbing effects, the following claim needs to be made, inside the sphere of influence any perturbation acts by modifying the classical spherical triangle introduced in [9] and [30] for the *relative* angles:

$$\begin{aligned} \gamma^* &= \gamma + \Delta\gamma \\ \psi^* &= \psi + \Delta\psi \\ \theta'^* &= \theta' + \Delta\theta' \end{aligned} \tag{5.6}$$

Note that such angles are in theory relative, their definition is strictly connected to the nominal b-plane coordinates, thus are expected to differ from point to point in the domain.

with the superscript * to identify the actual angles and the clean symbols to denote the analytical ones, from the usual resonance theory (Chapter 4, [30]).

5.3.1.1 *Geometry*

Since all the observations that will lead to the perturbing parameter definitions are made on the same reference frame, Figure 4.1 is shown again in this Section.

The final aim is to replicate the deflection obtained by the simulations including the perturbing effects. It is straight forward to model the variation in the deflection γ^* and θ'^*, if

$$\begin{aligned} \gamma^* &= \arccos\left(\frac{\mathbf{U}\cdot\mathbf{U}'}{||\mathbf{U}||||\mathbf{U}'||}\right) \\ \theta'^* &= \left(\frac{\mathbf{U}'\cdot\mathbf{v}_p^{out}}{||\mathbf{U}'||||\mathbf{v}_p^{out}||}\right) \end{aligned} \tag{5.7}$$

Note that in the upcoming lines the notation $\boldsymbol{U}$ and $\boldsymbol{U}'$ will stand for the actual velocity vectors obtained from the numerical simulation, whereas $\boldsymbol{v}_p^{out}$ will identify the planet's velocity at the exit of the sphere of influence.

re-arranging Equation (5.6) and with the definition of γ from Equation (4.10) the perturbing angle $\Delta\gamma$ becomes

$$\Delta\gamma = \gamma^* - \gamma = \gamma^* - \arccos\left(\frac{b^2 - c^2}{b^2 + c^2}\right) \tag{5.8}$$

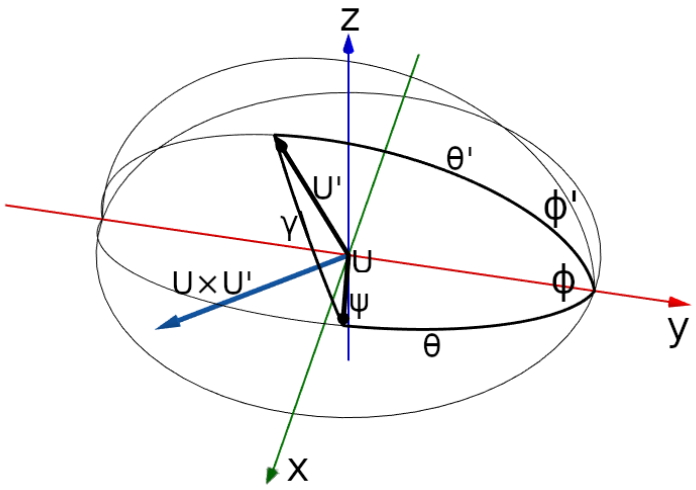

Figure 5.2: Deflection reference frame introduced by [9], as in Figure 4.1.

and $\Delta\theta'$, with the expression for θ' as in Equation (4.17)

$$\Delta\theta' = \theta'^{*} - \theta' = \theta'^{*} - \arccos\left(\frac{1 - 1/a'^{*} - U^2}{2U}\right) \tag{5.9}$$

with the symbol a'^{*} to denote the actual post-encounter semi-major axis. Note that this definition keeps in theory the model applicable to any post-encounter condition, not necessarily requiring it to be resonant. In fact, the actual value of a'^{*} should identify the b-plane locus of points leading to that specified post encounter semi-major axis.

It is conceptually more complicated to get the perturbation $\Delta\psi$, since some more observations on the geometry are needed. Note that the whole analysis is being conducted in the b-plane reference frame at the entrance of the sphere of influence, thus, by the definition of the reference frame in Equation (4.5), the b-plane under analysis is perpendicular to the vector $\mathbf{U}$, which is common to both the actual deflection and the theoretical definitions[2]. This has several friendly implications, particularly that the angle ψ is measured counterclockwise ([9], [30]) on the upside[3] b-plane, starting from the axis direction $-\hat{\zeta}$ and the vector $\mathbf{U} \times \mathbf{U}'$ must lay on the same b-plane as well.

Since ψ^{*} identifies the actual direction of the deflection, exploiting $\mathbf{U} \times \mathbf{U}'$ being normal to the plane containing both $\mathbf{U}$ and $\mathbf{U}'$, the counterclockwise angle measured from the direction $-\zeta$ to $\mathbf{U} \times \mathbf{U}'$ is simply defined as $\psi^{*} + \pi/2$ (Figure 5.2).

2 In fact, $\mathbf{U}$ is used to initialise the b-plane analysis by means of identifying $\cos\theta$ and preserving its magnitude U.

3 Facing towards positive $\hat{\eta}$ directions.

Recalling the definition of the theoretical ψ given in Equation (4.8) ([9] and [30])

$$\begin{aligned} \cos\psi &= \zeta/b \\ \sin\psi &= \xi/b \end{aligned} \tag{5.10}$$

one must note that the b-plane coordinates do not provide directly the deflection direction, since on the downside b-plane it is measured clockwise from the positive $\hat{\zeta}$ direction.

In fact, the two angles are measured on the two opposite sides of the b-plane, whereas the current definition for ψ proposed by [9] and [30] is strictly counterclockwise. Which real directions (clockwise or counterclockwise) to consider in each definition to get the proper counterclockwise value of $\Delta\psi$ becomes then not so clear: even though a more compact form could be reached with some further manipulation, a fully b-plane description of the deflection direction is presented, with the purpose of obtaining a better understanding of its description on the downside b-plane itself, which is what is seen when entering the planet's sphere of influence. Since both the deflection directions must lie on the b-plane, the geometry of Figure 5.3 is introduced to properly identify $\Delta\psi$. The angles $\tilde{\psi}^*$ and $\tilde{\psi}$ are both measured on the downside b-plane (where the resonant circles are represented), thus with ingoing $\hat{\eta}$ axis. The magnitude of the difference $\tilde{\psi}^* - \tilde{\psi}$ will correspond to $\Delta\psi$, its direction will be counterclockwise on this plane and clockwise in the 3-dimensional deflection reference frame of Figure 5.2.

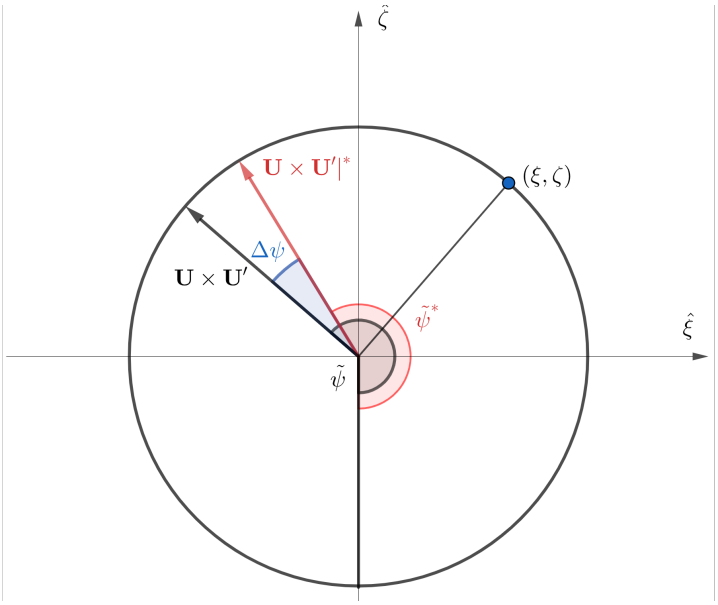

Figure 5.3: Graphical representation of the rotation convention used for the computation of $\Delta\psi$.

Particularly, the angle $\tilde{\psi} - \pi/2$ is defined as

$$\begin{aligned} \cos(\tilde{\psi} - \pi/2) &= -\frac{\zeta}{b} \\ \sin(\tilde{\psi} - \pi/2) &= \frac{\xi}{b} \end{aligned} \tag{5.11}$$

The actual deflection direction $\mathbf{U} \times \mathbf{U}'|^*$ is a vector that can be expressed in the b-plane reference frame in the same manner as it was done in Equation (4.6):

$$\mathbf{U} \times \mathbf{U}'|^*_{b-plane} = \left[\hat{\xi}, \hat{\eta}, \hat{\zeta}\right]^T \mathbf{U} \times \mathbf{U}'|^*_{cartesian} \tag{5.12}$$

with the component in the $\hat{\eta}$ direction to be equal to 0 by the cross product properties. Exploiting the geometry in Figure 5.3 the angle $\tilde{\psi}^*$ is defined as the counter-clockwise angle such that

$$\cos\tilde{\psi}^* = \frac{\left[\mathbf{U} \times \mathbf{U}'|^*_{\hat{\xi}}, \mathbf{U} \times \mathbf{U}'|^*_{\hat{\zeta}}\right]^T \cdot [0, -1]^T}{\|\mathbf{U} \times \mathbf{U}'|^*\|} \tag{5.13}$$

and therefore in the original 3-dimensional deflection frame (Figure 5.2) the counterclockwise $\Delta\psi$ is given by

$$\Delta\psi = -(\tilde{\psi}^* - \tilde{\psi}) \tag{5.14}$$

5.3.1.2 *Modified circle parameters*

Such perturbing angles are going to modify the circle parameters, since their definition has a direct impact on the variables that mathematically defined the circles (Equation (4.21)).

First of all, the modified $\cos\theta'^*$ can be kept in such a form, provided that its explicit definition is made clear as

$$\cos\theta'^* = \cos(\theta' + \Delta\theta') = \cos\theta'\cos\Delta\theta - \sin\theta'\sin\Delta\theta \tag{5.15}$$

Secondly, a re-derivation of the resonant circle equation is needed. The spherical triangle equation highlighting the perturbations is then:

The subscript 0 on $\cos\theta'^*_0$ stands for a resonant post encounter semi-major axis.

$$\cos\theta'^*_0 = \cos\theta\cos(\gamma + \Delta\gamma) + \sin\theta\sin(\gamma + \Delta\gamma)\cos(\psi + \Delta\psi) \tag{5.16}$$

with the trigonometry relations

$$\begin{aligned} \cos(A + B) &= \cos A\cos B - \sin A\sin B \\ \sin(A + B) &= \sin A\cos B + \cos A\sin B \end{aligned} \tag{5.17}$$

an equation of the following form is obtained

$$\begin{aligned} \cos\theta'^*_0 =& a_1\cos\gamma + a_2\sin\gamma + a_3\sin\gamma\cos\psi + a_4\cos\gamma\cos\psi \\ &+ a_5\sin\gamma\sin\psi + a_6\cos\gamma\sin\psi \end{aligned} \tag{5.18}$$

with the a_i coefficients not to depend on the b-plane variables, particularly:

$$\begin{aligned} a_1 &= \cos\theta\cos\Delta\gamma \\ a_2 &= \cos\theta\sin\Delta\gamma \\ a_3 &= \sin\theta\cos\Delta\gamma\cos\Delta\psi \\ a_4 &= \sin\theta\sin\Delta\gamma\cos\Delta\psi \\ a_5 &= -\sin\theta\cos\Delta\gamma\sin\Delta\psi \\ a_6 &= -\sin\theta\sin\Delta\gamma\sin\Delta\psi \end{aligned} \tag{5.19}$$

By replacing the trigonometric functions of γ and ψ with their b-plane definitions, Equation (5.18) becomes

$$\begin{aligned} (b^2+c^2)\cos\theta'^*_0 = \; & a_1(b^2-c^2) + 2a_2bc + 2a_3c\zeta + a_4(b^2-c^2)\zeta/b \\ & + 2a_5c\xi + a_6(b^2-c^2)\xi/b \end{aligned} \tag{5.20}$$

A final claim about modelling the perturbed resonant circles is made: since the perturbing effects must be small compared to the main 2-body effect, the overall shape should be still identified by circles centred on the ζ axis. To find the parameters of such circles it then is enough to obtain two expressions for the two intersections with the ζ axis:

$$\zeta_{1,2} = D \pm R \tag{5.21}$$

which correspond to the solution of the quadratic equation that is obtained by setting $\xi = 0$ in Equation (5.20):

The equivalence $b^2 = \zeta^2 + \xi^2$ must still hold, thus for $\xi = 0$ it must also be introduced that $b = \zeta$.

$$(\zeta^2+c^2)\cos\theta'^*_0 = \; a_1(\zeta^2-c^2) + 2a_2c\zeta + 2a_3c\zeta + a_4(\zeta^2-c^2) \tag{5.22}$$

therefore

$$\zeta^2 - 2c\frac{B}{A}\zeta + c^2\frac{C}{A} = 0 \tag{5.23}$$

where, writing explicitly the coefficients a_i

$$\begin{aligned} A &= \cos\theta'^*_0 - \cos\theta\cos\Delta\gamma - \sin\theta\sin\Delta\gamma\cos\Delta\psi \\ B &= \sin\theta\cos\Delta\gamma\cos\Delta\psi - \cos\theta\sin\Delta\psi \\ C &= \cos\theta'^*_0 + \cos\theta\cos\Delta\gamma + \sin\theta\sin\Delta\gamma\cos\Delta\psi \end{aligned} \tag{5.24}$$

The solutions to Equation (5.23) are

$$\zeta_{1,2} = \frac{2c(B \pm \sqrt{B^2 - AC})}{2A} \tag{5.25}$$

It is now possible to operate some simplifications under the square root, particularly some of the terms become:

$$\begin{aligned} B^2 &= \sin^2\theta\cos^2\Delta\gamma\cos^2\Delta\psi - 2\sin\theta\cos\Delta\gamma\cos\Delta\psi\cos\theta\sin\Delta\psi + \\ &\quad \cos^2\theta\sin^2\Delta\psi \\ AC &= \cos^2\theta_0'^* - (\cos\theta\cos\Delta\gamma + \sin\theta\sin\Delta\gamma\cos\Delta\psi)^2 \\ &= \cos^2\theta_0'^* + \cos^2\theta\cos^2\Delta\gamma + 2\cos\theta\cos\Delta\gamma\sin\theta\sin\Delta\gamma\cos\Delta\psi + \\ &\quad \sin^2\theta\sin^2\Delta\gamma\cos^2\Delta\psi \end{aligned} \tag{5.26}$$

thus

$$\begin{aligned} B^2 - AC = &\sin^2\theta\cos^2\Delta\gamma\cos^2\Delta\psi + \cos^2\theta\sin^2\Delta\psi - \cos^2\theta_0'^* + \\ &\cos^2\theta\cos^2\Delta\gamma + \sin^2\theta\sin^2\Delta\gamma\cos^2\Delta\psi \end{aligned} \tag{5.27}$$

and using the identity $\sin^2\Delta\gamma = 1 - \cos^2\Delta\gamma$

$$B^2 - AC = \cos^2\theta - \cos^2\theta_0'^* + \sin^2\theta\cos^2\Delta\psi \tag{5.28}$$

finally the use of $\cos^2\Delta\psi = 1 - \sin^2\Delta\psi$ yields the desired solution form $\zeta_{1,2} = D \pm R$, where

$$\begin{aligned} D &= \frac{c(\sin\theta\cos\Delta\gamma\cos\Delta\psi - \cos\theta\sin\Delta\psi)}{\cos\theta_0'^* - \cos\theta\cos\Delta\gamma - \sin\theta\sin\Delta\gamma\cos\Delta\psi} \\ R &= \left| \frac{c\sqrt{\sin^2\theta_0'^* - \sin^2\theta\sin^2\Delta\psi}}{\cos\theta_0'^* - \cos\theta\cos\Delta\gamma - \sin\theta\sin\Delta\gamma\cos\Delta\psi} \right| \end{aligned} \tag{5.29}$$

Note that, as a proper perturbation model, if the angles $\Delta\gamma$, $\Delta\psi$ and $\Delta\theta'$ were all to be zero the original solution from [30] would be obtained.

5.4 VALIDATION STRATEGY

The validation process is presented in Chapter 6, validating the deflection model itself and studying its relative-validity limits[4], and comparing the perturbed resonant circles with the b-plane coordinates of simulated samples in actual post-encounter resonance. Note that the validation process presented digs already into the planetary protection and defence study, whose complete version would include more thorough and extensive analyses about the risk of impact/resonance with the current planet.

4 In other words, since the perturbing angles introduced are relative it may be reasonable to expect them pretty similar for b-plane points close enough to each other.

6

RESONANCE MODEL VALIDATION

6.1 INTRODUCTION

The validation of the model developed in Chapter 5 will feature two main and consequent directions. First of all, the deflection model will be validated by itself, together with studying the error in the nearby b-plane regions if the perturbing angles $\Delta\gamma$ and $\Delta\psi$ are approximated as equal to the reference's ones.

Secondly, the perturbation on $\cos\theta'$ will be introduced and its quality will be checked directly by comparing the simulated resonances and the perturbed resonant belts. In this regards, Monte-Carlo simulations have been performed with SNAPPSHOT [11]. The test cases presented in this work feature three Near-Earth asteroids (Apophis, Duende, 2018BD) and Solar Orbiter's[1] launcher upper stage in its first uncontrolled flyby of Venus [2].

Each simulation includes N-body gravitational and general relativity effects.

In fact, the three asteroids highlight already a planetary defence application, whereas the uncontrolled dynamics of the upper stage of Solar Orbiter's launcher starts the planetary protection analysis.

6.2 DEFLECTION MODEL

As already briefly introduced, the validation of the deflection model involves the perturbations on the angles γ and ψ only. The solution of the spherical triangle in Figures 4.1 and 5.2 leads to the resonant circle equation by finding the combination of γ and ψ as the locus of b-plane points that brings a given post-encounter semi-major axis, i.e. a specified $\cos\theta'$. The case will be tackled on the opposite side, in order to maintain the generality of talking about the flyby deflection instead of restricting the analysis to the sole angle between $\mathbf{U}'$ and $\mathbf{v}_p^{out}$. Therefore, a b-plane domain map will be introduced, whose coordinates are numerically propagated until exiting the sphere of influence, building the benchmark to test the quality of the standard b-plane deflection model and the perturbed one.

For the sake of conciseness only a few remarkable cases[2] will be presented and discussed, from Apophis' and Solar Orbiter's velocities at the entrance of the sphere of influence in the same cases for the resonance analysis. Detailing deeper the plots that will be presented:

1 Solar Orbiter is a European Space Agency's mission to be launched in February 2020, studying the Sun and the related space weather phenomena [12].

2 In terms of b-plane coordinates.

- *Standard b-plane model*: the geometry in Figure 4.1 brings the full deflection, without considering any perturbation effects and obtaining $\mathbf{U}'$ from the angles γ and ψ (function of the b-plane coordinates). The error with respect to the simulated deflection is plotted.
- *Perturbed b-plane model*: the corrections $\Delta\gamma$ and $\Delta\psi$ are added as the ones featuring the middle point in the domain plotted for all the points, adding such effects to the standard deflection. The error with respect to the simulated deflection is plotted.

6.2.1 *Simulation details*

All the b-plane map points have been simulated with MATLAB®, propagating the initial conditions in non-dimensional coordinates with the solver `ode113.m`, using SPICE [1] as the ephemerides source and with a dedicated event function to stop the simulation at the exit of the sphere of influence. In this case the simulations have been carried out in the J2000 reference frame centred in the Solar System's barycentre, although any other reference could be chosen as long as consistency is kept among all the units and conversions.

The details about the precise times, locations and features of the close approach will be given in the following section, since the focus here is just to compare the different deflection models with the simulation benchmark.

6.2.2 *Apophis case*

The analysis of the deflection approximation in two different b-plane regions is reported in this section, low (Figures 6.2 and 6.1) and high (Figures 6.3 and 6.4) altitude flybys respectively, with two different colour scales in order to better highlight the differences between the two models. Note that impact regions have not been considered.

At low altitude the overall error is rather high for the unperturbed deflection (Figure 6.1), increasing for points closer to the attractor and, generally, showing a pretty steep variation over the whole domain. A remarkable improvement is obtained with the corrected model (Figure 6.2) in a wide region about the reference point, where the error goes to zero.

At high altitude the error decreases in magnitude for the unperturbed case (Figure 6.3), even though it remains different from zero about the reference. A displaced lower error region is observed, which may be explained by some occasional compensation of the error. The correction model is again effective (Figure 6.4), leading to a lower error about the reference point.

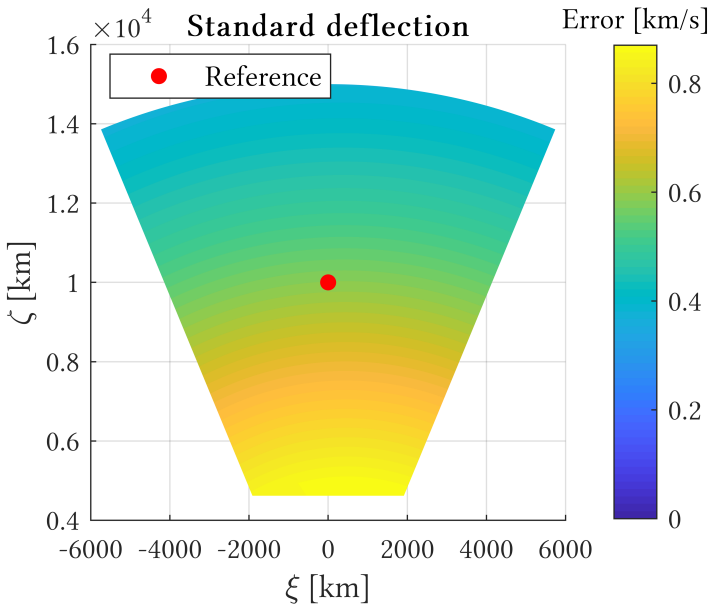

Figure 6.1: Apophis case, deflection error at low altitudes for the unperturbed model, as the norm of the difference between the actual and the modelled vectors.

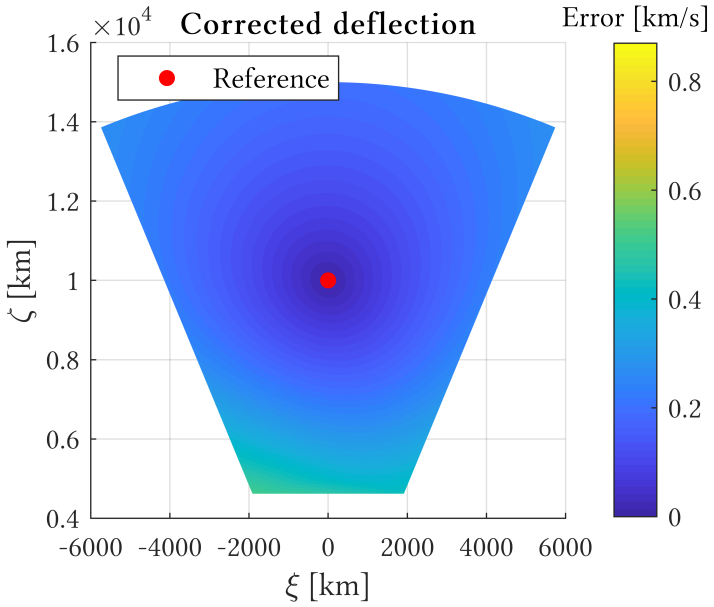

Figure 6.2: Apophis case, deflection error at low altitudes for the corrected model, as the norm of the difference between the actual and the modelled vectors.

Other b-plane regions (intermediate altitudes and circular sectors) have been analysed and are not included here for the sake of conciseness, since the behaviour observed remains basically the same, with the error getting to zero at and significantly decreasing nearby the reference point.

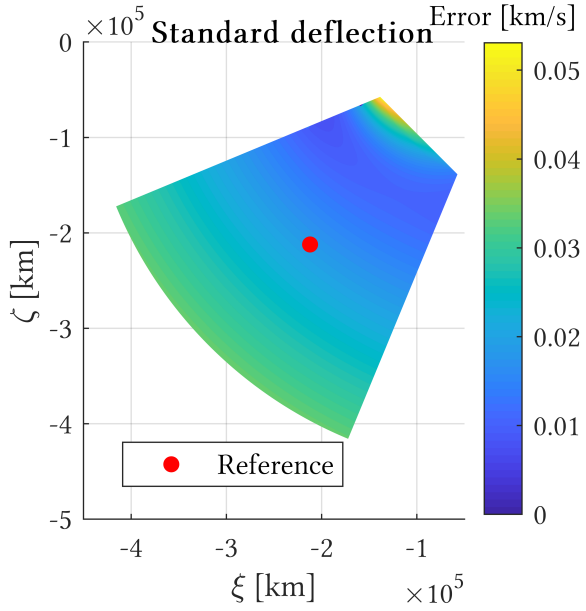

Figure 6.3: Apophis case, deflection error at high altitudes for the unperturbed model, as the norm of the difference between the actual and the modelled vectors.

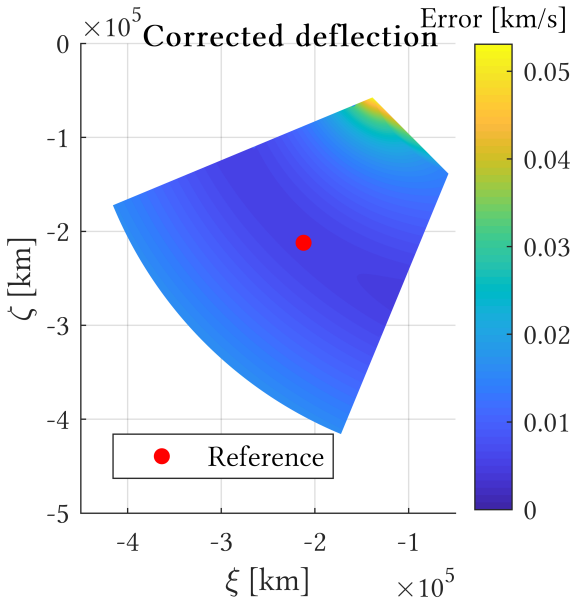

Figure 6.4: Apophis case, deflection error at high altitudes for the corrected model, as the norm of the difference between the actual and the modelled vectors.

6.2.3 *Solar Orbiter case*

The analysis of the deflection approximation in two different b-plane regions is reported in this section, low (Figures 6.5 and 6.6) and medium-low (Figures 6.7 and 6.8) altitude flybys respectively, with

two different colour scales in order to better highlight the differences between the two models. Note that impact regions have not been considered.

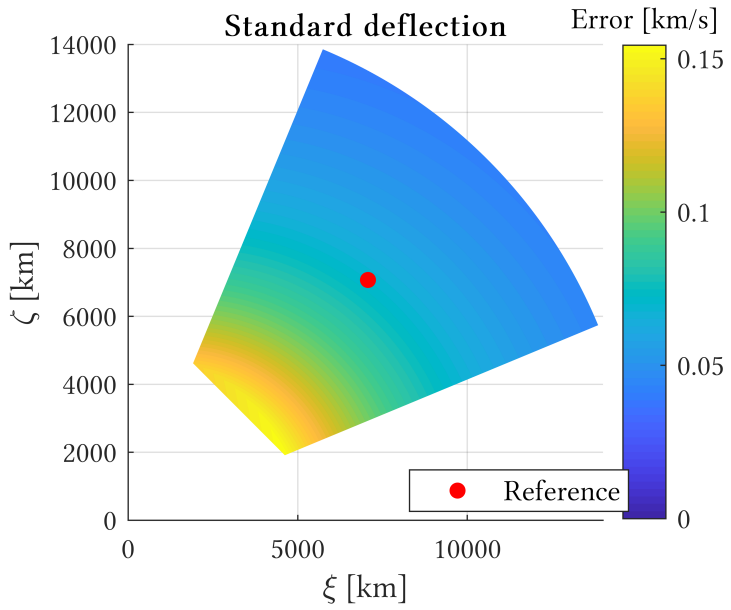

Figure 6.5: Solar Orbiter case, deflection error at low altitudes for the unperturbed model, as the norm of the difference between the actual and the modelled vectors.

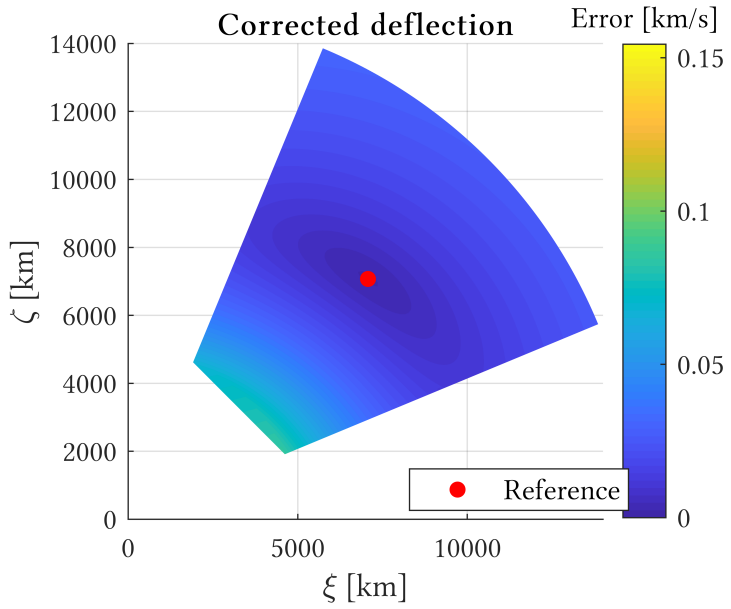

Figure 6.6: Solar Orbiter case, deflection error at low altitudes for the corrected model, as the norm of the difference between the actual and the modelled vectors.

Similarly to the Apophis case (Figure 6.1), at low altitude the overall error in this case (Figure 6.5) is rather high even though smaller in

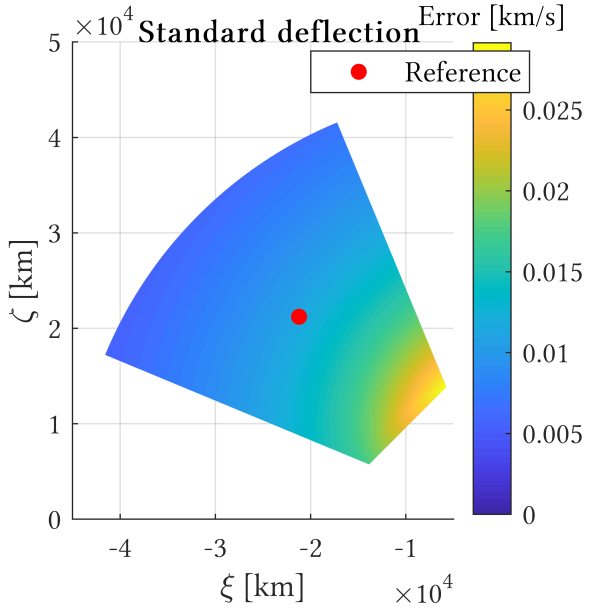

Figure 6.7: Solar Orbiter case, deflection error at medium-low altitudes for the standard model, as the norm of the difference between the actual and the modelled vectors.

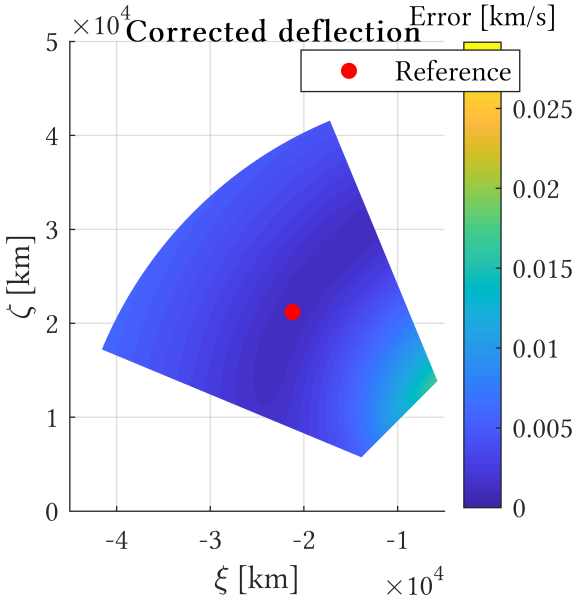

Figure 6.8: Solar Orbiter case, deflection error at medium-low altitudes for the corrected model, as the norm of the difference between the actual and the modelled vectors.

magnitude, increasing for points closer to the attractor. The deflection prediction is again more accurate with the corrected model (Figure 6.6), with a high precision region even wider than the correspondent Apophis case.

For medium-low altitudes a regular variation of the error is experienced (Figure 6.7), getting higher the closer the points are to the attractor, although overall lower in magnitude than the lower altitude case (Figure 6.5). The corrected deflection (Figure 6.8) is again precise about the reference, with a wide high accuracy region as in the low altitude case.

Other b-plane regions have been analysed and are not included here for the sake of conciseness, since the behaviour observed remains basically the same, with the error getting to zero at and significantly decreasing nearby the reference point.

6.3 B-PLANE PERTURBED RESONANCE MODEL

The just validated deflection model is used to show an improved definition of the resonant belts, adding the perturbing effect $\Delta\theta$ and letting the b-plane definitions of the angles γ and ψ identify the locus of points.

All the cases will be analysed as plots on the b-plane with a common colour legend, therefore presented here for good, leaving the floor to the analysis itself in each of the following subsections:

- *Red dots*: the current sample features a simulated impact with the planet.
- *Yellow dots*: the current sample features a simulated resonance (i.e. satisfying the condition in Equation (5.1) presented in [11].)
- *Dark grey dots*: the current sample features a simple close approach.
- *Blue dot*: reference sample (nominal condition which the cloud is generated upon) for the b-plane axes computation.
- *Black lines*: boundaries of the resonant belts.
- *Light grey lines*: perfect resonances (i.e. resonant circles).

6.3.1 *Test cases, introduction*

Each of the test cases will be introduced together with its nominal initial condition $(\mathbf{r}_0, \mathbf{v}_0, t_0)$ (J2000 reference frame, centred on the Solar System's barycentre). For the near-Earth asteroids, the clouds have been generated by applying to each component of position and velocity vectors a relative deviation to the nominal value, normally distributed with boundaries $\pm 0.005\%$ and propagated with SPICE ephemerides data [1]. Solar Orbiter's cloud has been instead generated according to the co-variance matrix given in [11], computed as specified by [16] to comply with ESA's planetary protection requirements, and propagated with ESA's ephemerides routine as in [11].

For all the cases, the numerical propagations have been carried out 100 years forward in time from the initial epoch, in the J2000 reference frame centred on the Solar System's barycentre. The b-plane analysis has been then performed at the first close encounter at the entrance of the sphere of influence, with the simulated samples converted into b-plane coordinates, switching them first into a J2000 planetocentric reference frame, by Equation (4.6), and plotting such coordinates in the b-plane of the nominal condition.

In each subsection the non-perturbed resonant belts (i.e. the original theory in [30] with the relaxed resonance definition as presented in Section 5.2) will be compared with the modified belts, presented in Section 5.3, with the corrective parameters computed by the perturbations featuring the nominal simulated trajectory[3]. For each case, the relative errors on the ζ coordinate of the lower bound of the three resonant belts closest to the reference sample are reported, for both the standard and the corrected belts. Note that the coordinate ζ has been chosen because of being the most significant b-plane coordinate varying from belt to belt, as well as an already available parameter for any point in the simulated clouds. The lower bound has been chosen arbitrarily and to select the actual resonant samples in an handier way, even though such a choice does not affect the contents of the analysis. The very same results, as it will be confirmed by the more visual plots, could have been shown by computing the error on the middle circles or on the upper bound of the resonant belts. Finally, only three belts are reported per each case because of the extreme variation of the number of resonances experienced in the test cases and to maintain a common framework, from a minimum of indeed 3 for 2018BD to more than 20 for Solar Orbiter. The three belts, for the cases where more resonances are experienced, are chosen as the closest to the reference because, as it was shown in Section 6.2, the deflection model is supposed to perform at its best about such point, therefore where the most significant improvements are expected even for the resonant belts modelling.

A particular observation needs to be made about modelling the perturbation $\Delta\theta'$, whose definition might be misunderstood in this context where only the resonant returns are searched. The common reference is the computation of the perturbation effects with respect to the nominal condition, with the definition straight forward in the case of the angles $\Delta\gamma$ and $\Delta\psi$ because dealing with the actual and theoretical velocity vectors. Despite it is used to improve the resonant belt model, the perturbation $\Delta\theta'$ is computed again on the reference sample, whose close approach may be in general perfectly resonant, quasi-resonant or just simple. The actual post-encounter semi-major axis a'^* is thus computed on the nominal condition and then used

3 Given the results of the deflection validation, a zero error would be expected at the reference, if this was located on a circle's intersection with the $\hat{\zeta}$ axis.

in Equation (5.9), with such a $\Delta\theta$ to be applied to all, in this case resonant, the b-plane circles that one wishes to draw.

Note that the resonance ratio is reported only when visible/relevant, because of, in some of the cases, the too packed samples/belts.

6.3.2 *Apophis*

The nominal initial condition is

$$\begin{aligned} \mathbf{r}_0 &= \begin{Bmatrix} 18658363.5984703 \\ 132490717.716693 \\ 49676168.1228006 \end{Bmatrix} \text{ km} \\ \mathbf{v}_0 &= \begin{Bmatrix} -28.3478281346163 \\ 9.00743133531365 \\ 2.63329103908463 \end{Bmatrix} \text{ km/s} \\ t_0 &= 10227 \text{ MJD2000(midnight)} \end{aligned} \tag{6.1}$$

and features a *resonant* close approach (resonance condition $k/h = 7/6$) with Earth at epoch 10694.3 MJD2000. The non-perturbed resonant belts and the perturbed ones are plotted in Figures 6.9 and 6.10 respectively.

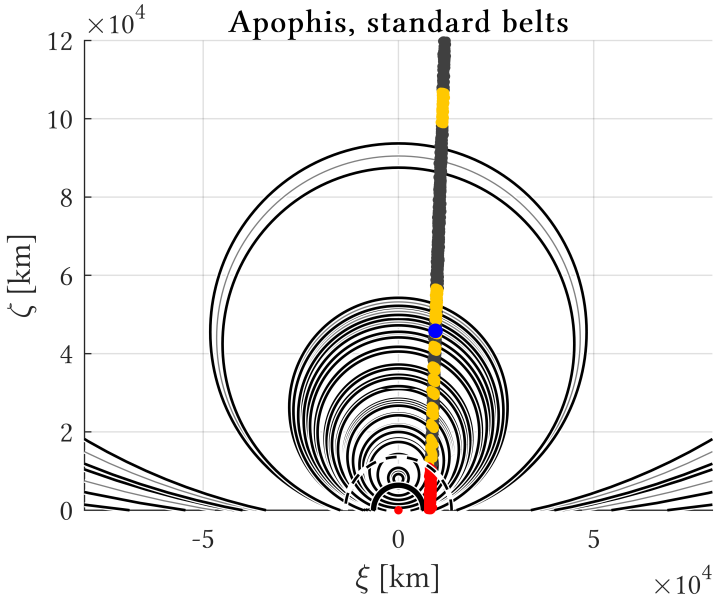

Figure 6.9: Apophis case, standard resonant belts vs simulated resonances.

A slight deviation between the simulated and the standard resonant belts is experienced (Figure 6.9), between all the analytical resonant belts and the correspondent simulated ones. The correction parameters improve the model (Figure 6.10), leading to a basically perfect correspondence of the simulated and modelled resonances particularly

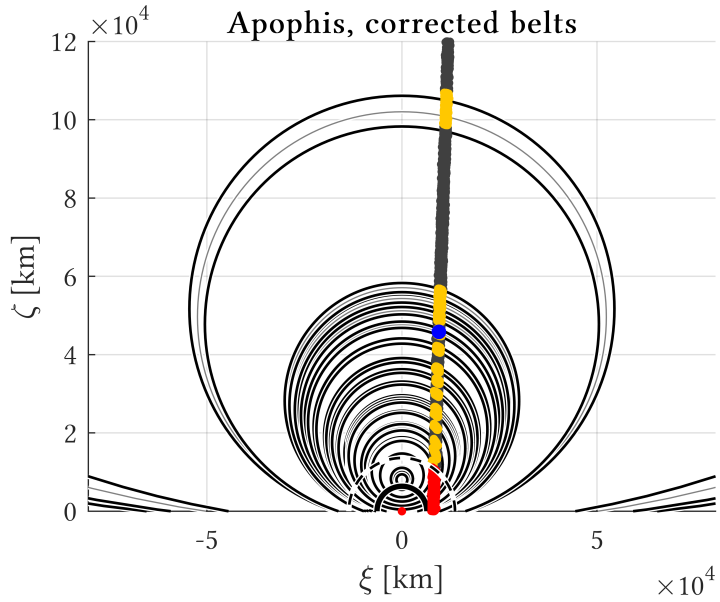

Figure 6.10: Apophis case, corrected resonant belts vs simulated resonances.

close to the reference sample. The correspondence is improved, but not perfect, for the upper belt. The relative error for the three resonances closest to the simulation reference are reported in Table 6.1.

k/h	Standard belt	Corrected belt
7/6	6.045%	0.199%
6/5	5.594%	0.327%
8/7	6.506%	0.047%

Table 6.1: Apophis case, relative error for standard and corrected belt models with respect to the simulated resonances.

The lower error for the 8/7 belt, with respect to the reference 7/6, might be due to the corrective coefficients computed at the reference but applied at the intersection with the $\hat{\zeta}$ axis, which might lead to slight occasional compensations of this kind in other near b-plane regions.

The corrected belts in Figure 6.10 seem to be pretty accurate also for all the points closer to Earth than the reference. This result complies with the deflection validation shown in Figure 6.2, where rather high errors were practically obtained only for points within the impact region, despite using the corrective parameters of the reference sample.

As another observation, in opposition to the next cases, the nominal close approach experienced will be shown to be the deepest overall.

6.3.3 *Duende*

The nominal initial condition is

$$\begin{aligned} \mathbf{r}_0 &= \begin{Bmatrix} -18623208.1303659 \\ 130438213.384556 \\ 36039104.1291735 \end{Bmatrix} \text{ km} \\ \mathbf{v}_0 &= \begin{Bmatrix} -32.2871979890617 \\ -3.11275285550554 \\ 2.42528219708185 \end{Bmatrix} \text{ km/s} \\ t_0 &= 4383 \text{ MJD2000(midnight)} \end{aligned} \tag{6.2}$$

and features a *simple* close approach with Earth at epoch 4794.92 MJD2000. The non-perturbed resonant belts and the perturbed ones are plotted in Figures 6.11 and 6.12 respectively.

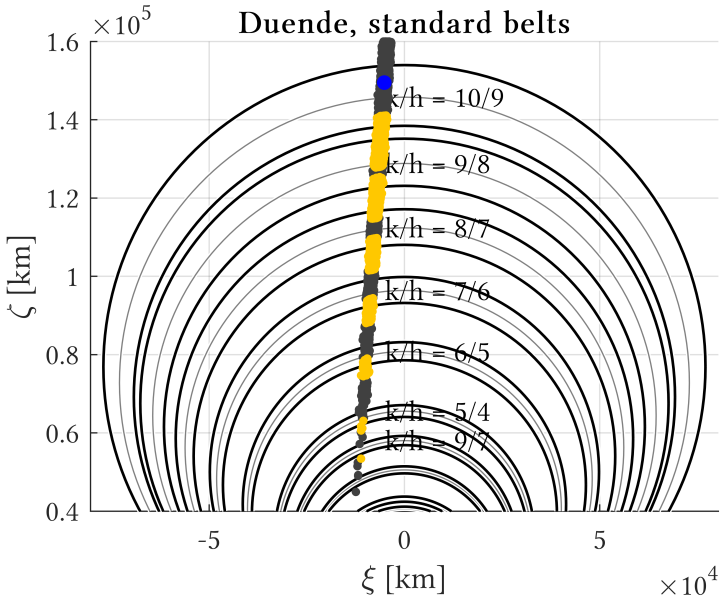

Figure 6.11: Duende case, standard resonant belts vs simulated resonances.

Similarly to Figure 6.9, a slight deviation is experienced again for Duende (Figure 6.11) and, as it happened for Apophis case, the corrected model (Figure 6.12) is basically matching the simulated resonances. The relative error for the three resonances closest to the simulation reference are reported in Table 6.2.

In this case, the corrected model behaves in the expected way: the resonance 10/9 is the closes to the reference, with also the lower relative error.

Duende's close approach is not as deep as Apophis' one, nevertheless there seems to be no effect within such a distance range between the furthermost samples and the reference, having again used the corrective parameters from the nominal simulation only.

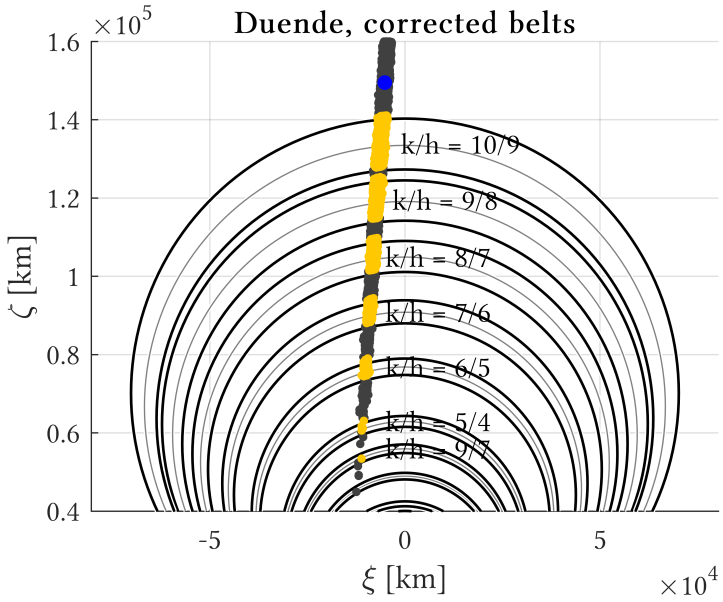

Figure 6.12: Duende case, corrected resonant belts vs simulated resonances.

k/h	Standard belt	Corrected belt
10/9	8.039%	0.869%
9/8	6.866%	1.076%
8/7	5.748%	1.307%

Table 6.2: Duende case, relative error for standard and corrected belt models with respect to the simulated resonances.

6.3.4 *2018BD*

The nominal initial condition is

$$\mathbf{r}_0 = \begin{Bmatrix} -6327111.07348661 \\ -141477865.487925 \\ -65847724.4156263 \end{Bmatrix} \text{ km}$$
$$\mathbf{v}_0 = \begin{Bmatrix} 29.3692470755624 \\ -9.93649939637433 \\ -3.13293598090667 \end{Bmatrix} \text{ km/s} \tag{6.3}$$
$$t_0 = 6210 \text{ MJD2000(midnight)}$$

and features a *simple* close approach with Earth at epoch 6592.86 MJD2000. The non-perturbed resonant belts and the perturbed ones are plotted in Figures 6.11 and 6.12 respectively.

The bigger dimension of the cloud seems now to affect the model prediction, especially the farther the samples get from the reference point. Even for the standard case (Figure 6.13) it can be seen that the distances involved are higher than the previous case. The correction

Note that the upper points of such a cloud reach an impact parameter in the order of 3×10^5 km *and the reference sample stands about at* 1.7×10^5 km

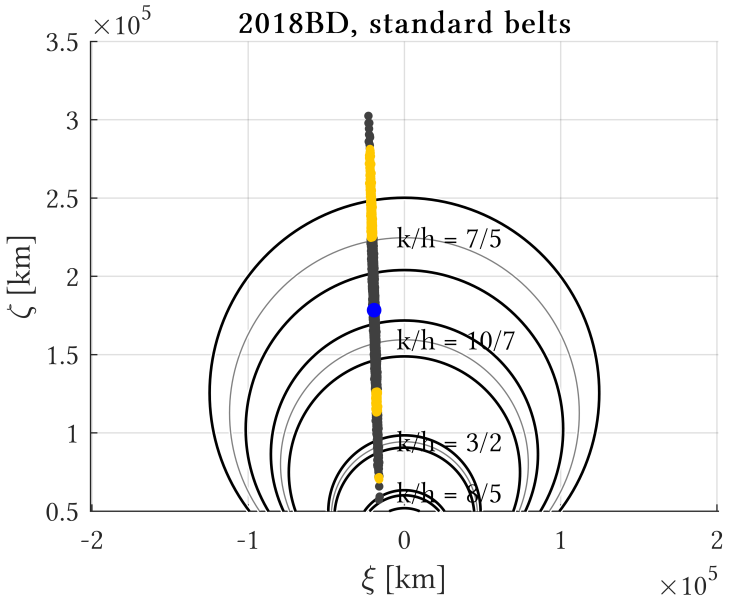

Figure 6.13: 2018BD case, standard resonant belts vs simulated resonances.

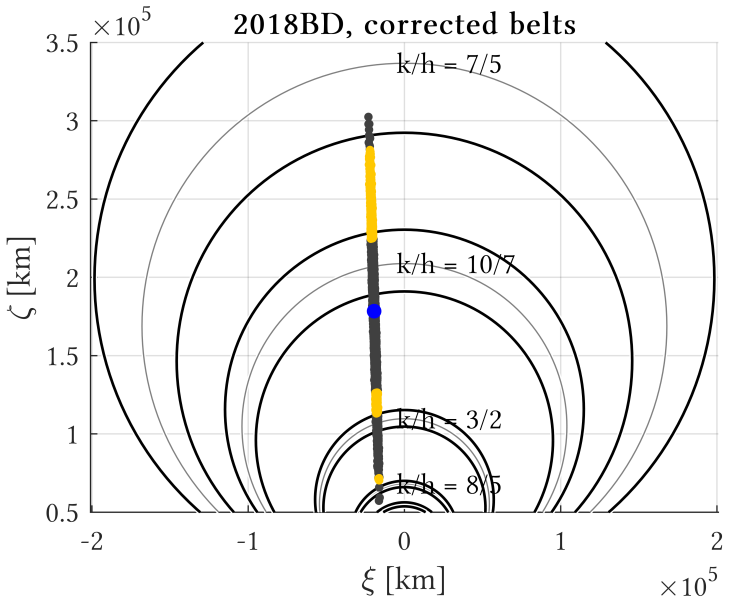

Figure 6.14: 2018BD case, corrected resonant belts vs simulated resonances.

(Figure 6.14) improves the model, although not as much as in the previous cases.

Note also that the distance range would be within what observed being the accurate regions presented in the deflection validation in Section 6.2, however one must remember that such regions were obtained with Apophis' flyby properties and despite the error still going to zero at the reference point, the different conditions featuring 2018BD's flyby, particularly on the planetocentric velocity, may lead to remarkably different accurate region sizes. A future work development

certainly involves a thorough analysis of the high-accuracy regions behaviour with the variation of the parameter c [4]. The relative error for the three resonances closest to the simulation reference are reported in Table 6.3.

k/h	Standard belt	Corrected belt
10/7	34.823%	15.745%
3/2	22.739%	9.832%
8/5	20.862%	11.968%

Table 6.3: 2018BD case, relative error for standard and corrected belt models with respect to the simulated resonances.

As the errors in Table 6.3 show, the correction model still improves the results, even though, as already mentioned, given the generally high distances from the reference and the possible effect related to the parameter c its performances are not as good as in the two previous cases.

6.3.5 *Solar Orbiter's launcher upper stage*

The nominal initial condition is

$$\begin{aligned} \mathbf{r}_0 &= \begin{Bmatrix} 132048839.0181729 \\ 63140185.87973432 \\ 27571915.37875966 \end{Bmatrix} \text{ km} \\ \mathbf{v}_0 &= \begin{Bmatrix} -12.19900175754253 \\ 20.24016626492768 \\ 9.767449779831535 \end{Bmatrix} \text{ km/s} \\ t_0 &= 6868.619376111506 \text{ MJD2000(midnight)} \end{aligned} \tag{6.4}$$

and the covariance matrix $\mathbf{C}$ used for the sample generation (from [11]) expressed in an inertial cartesian reference frame reported in Table 6.4.

The case features a *resonant* close approach (resonance condition $k/h = 5/4$) with Venus at epoch 7035.03 MJD2000. The non-perturbed resonant belts and the perturbed ones are plotted in Figures 6.11 and 6.12 respectively. Note that in order to spot the correspondent simulated and modelled resonances, only a portion of the whole cloud is shown.

As in 2018BD's case, the model prediction becomes less and less accurate the farther the cloud gets from the nominal sample, however with significant improvements in its neighbourhood. Note that, despite being the reference in the correct resonance predicted by the b-plane

4 Remembering its definition in Equation (4.9) as $c = \mu/U^2$

x km	y km	z km	v_x km/s	v_y km/s	v_z km/s
5.35E+04	5.41E+04	−2.56E+04	2.48E−01	2.74E−01	−1.21E−01
5.41E+04	1.36E+05	4.51E+03	2.34E−01	7.10E−01	3.43E−02
−2.56E+04	4.51E+03	1.73E+05	−1.37E−01	5.02E−02	8.33E−01
2.48E−01	2.34E−01	−1.37E−01	1.16E−06	1.18E−06	−6.49E−07
2.74E−01	7.10E−01	5.02E−02	1.18E−06	3.72E−06	3.08E−07
−1.21E−01	3.43E−02	8.33E−01	−6.49E−07	3.08E−07	4.02E−06

Table 6.4: Covariance matrix associated to the initial state of the launcher of Solo at the epoch 6868.6193MJD2000 expressed in an inertial reference frame [11].

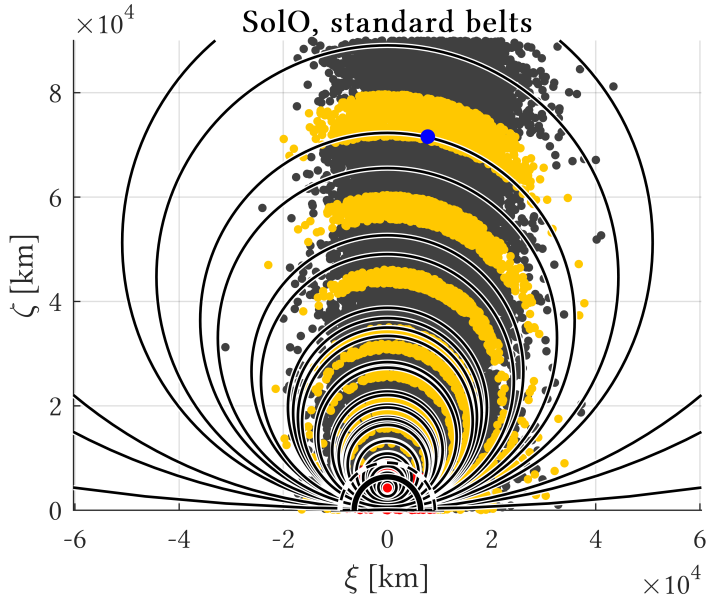

Figure 6.15: Solar Orbiter case, standard resonant belts vs simulated resonances.

belts, a slight deviation is observed between that semi-analytical belt and the simulated one. A possible explanation is again the deflection model, this time together with the circle definition. The reference sample is not exactly on the $\hat{\zeta}$ axis, whose intersections with the locii resonant points have been used to approximate the locii themselves by circles. Such a small position difference naturally embeds slightly different perturbing angles, and using the reference's one at the intersection with the $\hat{\zeta}$ axis may explain such a slight difference in the simulated and the modelled belts. The relative error for the three resonances closest to the simulation reference are reported in Table 6.5.

Again compatibly with the deflection model, the approximation seems to become better and better getting close to the attractor. A lower error for a non-reference belt is experienced, which may be an

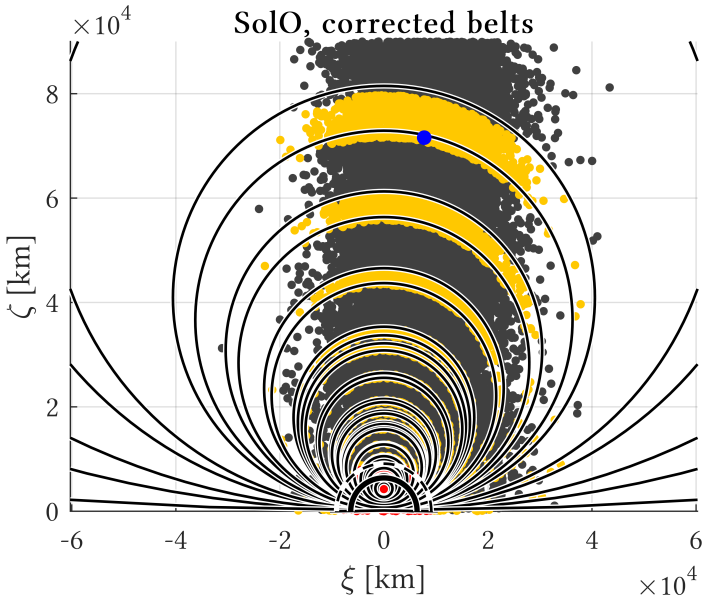

Figure 6.16: Solar Orbiter case, corrected resonant belts vs simulated resonances.

k/h	Standard belt	Corrected belt
5/4	24.460%	1.636%
6/5	52.669%	3.806%
9/7	17.499%	0.800%

Table 6.5: Solar Orbiter case, relative error for standard and corrected belt models with respect to the simulated resonances.

occasional compensation due to the perturbing angles computed on the reference and applied at the intersection with the $\hat{\zeta}$ axis.

In any case, the improvement obtained in this case is the highest overall, despite the small deflection errors shown in Section 6.2, suggesting again the need of a deeper analysis in the actual deflection behaviour with the parameter c.

7

CONCLUSION AND OUTLOOK

The model developed in Chapter 5 has gone through a first, even though limited, validation process. The corrective parameters proved to be quite an accurate approximation for resonances nearby the reference sample used for the computation.

Given the results obtained, a suitable approximation for planetary protection applications may involve assisting simulations in key b-plane region, rather than using the reference sample whose coordinates are generally unknown *a-priori*, in order to robustly and precisely map the perturbing effects even in the farthermost regions of the cloud.

For the sake of increasing again the model precision, the claim made about the shape of the locus of resonant points needs to be verified as well. The clouds analysed did not allow to check whether such an assumption was good at the outermost b-plane regions, thus the validity of such a claim must for now remain limited to the deepest encounters. A generalisation strategy is also possible, trying to stick to the deflection model as by itself looking for further developments.

Another issue to be taken into account, specific of planetary protection and defence applications, is the performed representation, namely plotting all the samples in the b-plane of the reference one. Indeed, the coordinates are computed with Equation (4.6), each single one featuring its own b-plane axes (Equation (4.5)) dependent on the planetocentric velocity $\mathbf{U}$. Such a b-plane property has a major impact on the plotted circles, whose elements actually depend on $\mathbf{U}$ and therefore are expected to be accurate for the reference sample only. A possible future exploration direction is then to include such an effect in the model, in order to apply some variation to the circle parameters dependent on the distance from the reference point.

Figure 7.1 shows that, as an example for the circle parameters' behaviour, the variation of the square of the radius is steep with the planetocentric velocity and appears to be linear, suggesting the exploration of some series expansion of the circle parameters upon $\mathbf{U}$ as a first modelling strategy.

Lastly, the most thorough validation strategy would include flybys over all the Solar System's planets. It is however difficult to find accurate data about asteroids or other bodies closely approaching planets

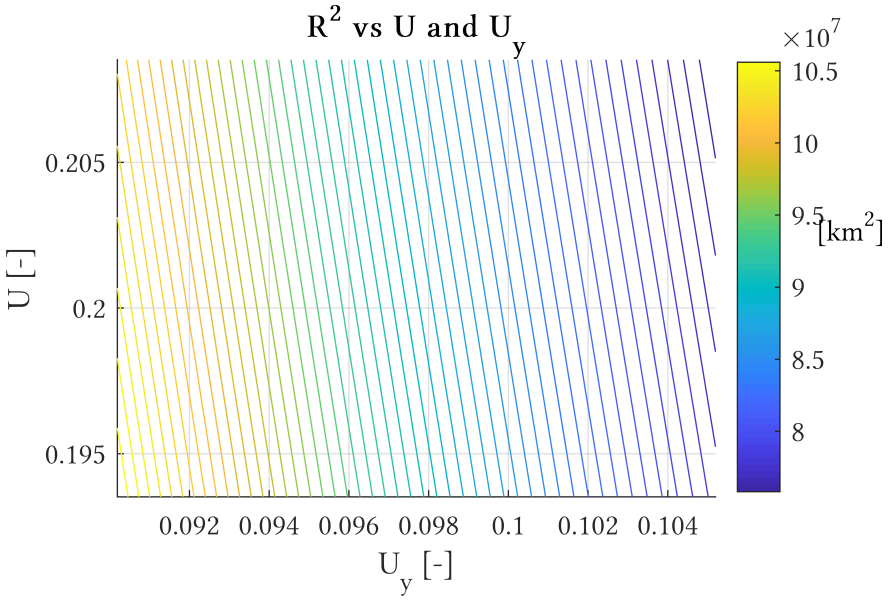

Figure 7.1: Apophis' square of the radius of the resonant circle 6/5 with respect to the non-dimensional magnitude and y-component (expressed in the deflection frame, Figure 4.1 has a direct impact on $\cos\theta$ [30]) of the planetocentric velocity, computed for planetocentric velocities between the minimum and the maximum ones in the cloud.

other than Earth, given the obvious interest in precisely monitoring such threatening objects. Artificial test cases would need to be created.

As the ultimate completion of the model, the final assumptions to be relaxed is the patched conics approximation itself. Note that the current model only improves the actual deflection making it compliant with the fully perturbed simulation, however such a deflection is considered as the two asymptotic conditions within the sphere of influence, thus applied as a sudden deflection exactly at the planet's position in an interplanetary point of view. The ultimate development goal should then be a more continuous model, accounting for the actual positions, times and velocities during the whole close encounter.

Part III

RESONANCE APPLICATION TO FLYBY DESIGN

8

BALLISTIC RESONANT FLYBY DESIGN ALGORITHM

8.1 INTRODUCTION

An improved model for b-plane orbital resonances has been developed in Part ii and validated with the first steps of planetary protection/defence analysis. In the way it currently stands, the model is not ready for the most general planetary protection application yet, since some further improvements and developments are needed (Chapter 7).

Nevertheless, a proof of its versatility will be shown by applying it to the design of resonant flybys, where the problem of different planetocentric velocities within the same b-plane representation is cut out, as well as a proper mapping of the perturbing effects on the b-plane could bring an almost real trajectory with low computational cost, basically only dependent on how thick the map is wanted to be.

In a planetary protection application one wishes to identify orbital resonances in order to minimise the probability of a resonant return, here the concept will be exploited in the exactly opposite way, using the degree of freedom left, in the patched conics approximation, by the point of injection in the sphere of influence to force resonant flybys, in order to achieve a total ballistic deflection that a single flyby could not provide.

Note that many other works have been performed on the design of resonant trajectories, all exploiting different concepts and shades of the resonance definition, and all meant to obtain optimal quasi ballistic deflections accounting also for other perturbing effects. Some of these methods exploit the resonance concepts for Earth-Moon missions trying to reach a weak capture, escape or the libration points, capable of lowering the fuel consumptions allowing for higher times of flight, determining a new set of governing equations or exploiting the properties of generalised dynamical systems, such as Ceriotti et al. [10], Topputo et al. [27], [26], Oshima et al. [21] and Vaquero et al. [32]. Other important applications concern all those missions at Saturn's and Jupiter's moon systems where the need of maximising the payload is crucial, being such orbits distant from Earth. In all the cases exploration missions seek to collect better data by performing repeated, resonant close approaches of a single moon or simply to exploit the natural gravitational field to reach other points of the space.

Among many of them, the study of low fuel consuption trajectories at the Jovian and Saturn's system has been done for example by Johannesen et al. [15], Ross et al. [24], Campagnola et al. [6], [7], [8], Lantoine et al. [17], Vaquero et al. [33], among hundreds of different shades of the same topics and moon systems.

All the just mentioned applications see a common framework, i.e. the Circular Restricted Three Body Problem (CR3BP) considering one moon, in the case of the giant planets, at a time and applying the dynamical systems theory, by means of Poincaré maps and invariant manifold dynamics. The Poincaré map [13] is a graphical tool used, generally, in dynamical systems theory that feature a periodic behaviour and, to general extent, undergoing to some perturbations. At a specified time such a tool is used to study a discretised dynamical system to show the evolution of the main system at each periodic passage through a selected state-surface normal to the system's evolution flow. The concept of invariant manifold [23] is strictly linked with the Poincaré map's one, despite having a more rigorous mathematical definition. It identifies a state-space region where the system is allowed to evolve in a continuous time frame, contrary to the periodic nature of the systems that can be studied with the Poincaré map. Two of the most important features of manifolds, among the others, is their stability (linked to the concept of "attraction") and and instability (viceversa qualitatively linked to "repulsion"), exploited in the trajectory design case to either get captured or escape from a gravitational field.

More restricted to the Orbital Mechanics field there is the tool/-concept of the Tisserand parameter and criterion and the connected Tisserand graph [6], which gives a visual identification of possible categories of motion in a strict orbital energetic sense. The quasi-conservation of the Tisserand parameter will be exploited in this work too, whereas other application combined the Tisserand graph features with the Poincaré map properties)[17], [7]), identifying new regions of allowed motion, albeit high time of flight demanding, more efficient than Hohmann transfers on the $\Delta\mathbf{v}$ point of view, as well as adding $\mathbf{v}_\infty$ leveraging manoeuvres [37] on top of such approaches, [8].

Returning to the perturbed model developed in this work, at the best of the author's knowledge, no application of this kind has been found in the existing literature, particularly dealing with open interplanetary resonances. The current non-completion of the model limits for now its usage to the patched conics definition of deflection, nevertheless the algorithmic method presented in this chapter will need some changes in the initial assumptions only, maintaining the innermost structure, where the actual b-plane flyby model enters, unaltered. Because of this, the actual interplanetary definition of resonance has remained unchanged and thus whatever resonant flyby designed will need to comply with the same. In other words, even though there is already the possibility to semi-analytically refine the planetocentric deflections,

Although an extension has been introduced with the quasi-resonance concept, the framework still remains the patched conics' one.

such modified resonances will not provide the same $\Delta\mathbf{v}$ of their 2-body parents, and therefore will not correspond to the $\Delta\mathbf{v}$ required for that specified resonance to happen [1].

That being said, the presented algorithmic method features a modular structure, where at the highest level the resonant flybys are designed by the solution of a global optimisation problem, under a fully 2-body patched conics approximation. At a lower level, the perturbed resonant deflections will be designed in order to minimise their difference with respect to each correspondent optimal 2-body $\Delta\mathbf{v}$.

8.2 2-BODY OPTIMAL RESONANCE DESIGN

Some work in a similar direction, even though not specifically meant for the optimal trajectory design purposes of this work, has already been performed in [31] and [28], where the authors developed an analytical solution for the post encounter keplerian parameters implementing the b-plane deflection formalism. In [31] and [28] the study was built such that a fully b-plane and keplerian description was enough to achieve a fully analytical solution. In this work the formulation presented will instead feature an hybrid cartesian, bplane and keplerian approach, in order to exploit the b-plane flyby design properties, the keplerian simple description of the orbital parameters and the simplicity and computational efficiency guaranteed by the cartesian coordinates.

Note that the cartesian formulation is perhaps the easiest choice for the flyby descriptions, where the deflections become simple vector summations.

8.2.1 *Key assumptions/observations*

8.2.1.1 *Tisserand parameter conservation*

First of all, a major limitation appears when using the b-plane formalism for design purposes: the deflections feature such a mathematical formulation only if fully natural, with a manoeuvre in the planetocentric motion to modify at least the outgoing asymptote and the hyperbolic excess velocity magnitude, severely affecting the geometry described in [9]. Since the objective of this section is to present an application of the current model, it is beyond the scopes of the whole work to investigate the modified deflections to take into account some manoeuvre execution, thus the design will stay limited to initial and final orbits featuring the same Tisserand parameter T. Indeed, recalling the relation in [9] and [30]

$$U = \sqrt{3 - T} \tag{8.1}$$

1 Referring again to [30], remember that the resonant circles are identified as the loci of points in the b-plane where the deflection leads to a specific post encounter semi-major axis, all under a 2-body patched conics approach. A different deflection may not lead to a post encounter resonant orbit.

interplanetary orbits with the same Tisserand parameter T are all and the only ones achievable with unpowered gravity assists, since the magnitude of the planetocentric velocity never changes. This implies that, given the quasi-conservation of the Tisserand parameter already embedded in the b-plane deflection formalism, a quasi-ballistic overall transfer between initial and final orbits is theoretically feasible under such a constraint.

This must not be seen as a limitation, it could actually be a property to be exploited to reduce the number of degrees of freedom when designing a flyby, as well as by definition potentially obtain a ballistic trajectory.

8.2.1.2 *Resonance consequences*

The 2-body patched conics definition of orbital resonance embeds naturally another assumption, of key value in this algorithm design: a resonant return is a consequent close approach happening after a *finite integer number of orbital periods of both the small body and the flyby planet*. Since such a number of orbits is indeed *integer*, the definition of orbital period, without considering orbital perturbations, implies that the next close approach is to happen at the same position and on the same interplanetary orbit of injection after the previous flyby.

Under a cartesian description of the two orbits, the elements of the position vector $\mathbf{r}$ will remain unchanged for all the resonant flybys designed, with only the heliocentric velocity $\mathbf{v}$ to change according to some $\Delta\mathbf{v}$ leading to consequent resonant returns. This new velocity $\mathbf{v} + \Delta\mathbf{v}$ (of the small body only, the planet obviously does not undergo any deflection) will then also be the ingoing condition of the consequent flyby, by the definition of resonant orbit itself.

8.2.2 *Combinatorial issues*

The standard flyby design is a highly combinatorial problem, with time playing a fundamental role in determining the best encounter position to target a desired orbit. Nevertheless, the definition of resonance allows to neglect at least a portion of such a combinatorial nature, having the encounter position always fixed in time and space moves the problem to the need of identifying the velocities only.

Even when dealing with resonances some combinatorial issues exist, namely what actual resonance (thus what set of planetocentric trajectories) to choose at each flyby. Once a specified resonance is chosen, there are again infinite possible solutions that satisfy such a resonance condition, indeed the degree of freedom exploited in the presented algorithm.

8.2.3 *Algorithm structure*

The implementation strategy chosen aims to drastically reduce the double combinatorial nature of the resonant flyby design, by paying the price of solving a non-smooth optimisation problem at the highest level.

8.2.3.1 *Non-handle inputs*

Apart from the various handle quantites, namely gravitational constants, reference frame and ephemerides data, the algorithm requires:

- a set of admissible resonances S [2];
- an initial orbit $(\mathbf{r}_0, \mathbf{v}_0)$;
- an ultimate target orbit $(\mathbf{r}_f, \mathbf{v}_f)$;
- the number of close approaches N to be designed to reach such a final trajectory.

8.2.3.2 *Sub-target optimisation*

A sub $\Delta\mathbf{v}$ target is assigned to each flyby and the planetocentric trajectory will be selected in order to minimise the difference between its own deflection and the specified sub-target.

The highest level consists then of finding a global optimal solution to the non-smooth optimisation problem, determining the best set of sub $\Delta\mathbf{v}$ targets that will eventually minimise the artificial contribution needed to match the final orbit. The non-smoothness of the problem, in principle unknown in its location on the domain, makes it necessary to use either stochastic-based (e.g. a genetic algorithm approach) or direct search methods to find the optimal solution. Any gradient-based method, such as interior point or active constraints, might not work in a global sense, unless a multi-start solution with a remarkably high number of initial points is implemented. A gradient-based optimisation could although be included to refine the results given by the direct search/stochastic first level solution, provided that it remains nearby the first level optimal solution.

As already outlined such a design is fully 2-body.

Note that, despite the solution comes from a global-like optimisation problem, it may not be unique and in general the lowest residual possible may not be compatible with other constraints (i.e. time-wise, having too long times of flight or also in some orbital parameters). At the current, initial development state of the algorithm the optimisation is let completely free, in order to get a first idea of performances and capabilities, with the possibility to add other constraints, include manoeuvres or more simply implement this ballistic resonance strategy

2 By definition the number of allowed resonances is integer, thus the non-smoothness is brought in the sense of having a mixed integer-nonlinear problem to solve.

in already existent design techniques to be among the first future developments.

The problem can then be formulated as:

$$\begin{aligned} &\text{minimise} && \|\Delta\mathbf{v}_{residual}(\Delta\mathbf{v}_i, (k/h)_i, \mathbf{v}_0, \mathbf{v}_f)\| && \\ &\text{subject to} && \sum_i \Delta\mathbf{v}_i = \Delta\mathbf{v}_{target} && i = 1, ..., N \\ & && (k/h)_i \in S && i = 1, ..., N \end{aligned} \tag{8.2}$$

Among the several possible ways of computing $\|\Delta\mathbf{v}_{residual}\|$, one should keep in mind the following three aspects:

- The summation of the sub-targets must lead to the global $\Delta\mathbf{v}_{target}$, but this does not mean that the optimal solution will exactly feature no residuals at each of the flybys. Even though it is not explicitly implemented as such, the resonance condition is actually a constraint on the $\Delta\mathbf{v}$ to occur at each flyby to experience a consequent return, whereas, in order to get rid of the combinatorial issues, the only linear constraint (in this case) put on the sub-targets is their summation to give the global target.
- Despite the likely experienced residuals, that cannot be included in the correspondent flybys, the summation of all the actual $\Delta\mathbf{v}$s given must still lead to the final target.
- When designing the last flyby it does not matter whether it is resonant or not (it may actually never be if the target orbit is not resonant), with this to imply much more flexibility and possibilities in the design of the last deflection.

In order to then fulfill all those aspects and constraints, a possible design choice is to split evenly the residual $\Delta\mathbf{v}$ of the current flyby over all the next sub-targets, in order to avoid the risk of sub-targets getting remarkably different each other. This allows, other than to automatically fulfill the constraint of the sub-target summation, to always design resonant flybys up to and including the second to last, without any artificial $\Delta\mathbf{v}$ needed, letting the last and more flexible deflection to be optimised in order to get as close as possible to the final target.

For N flybys the sub-target update can be easily written as:

$$\Delta\mathbf{v}^i_{target,new} = \Delta\mathbf{v}^i_{target} + \sum_{j=1}^{i-1} \frac{\Delta\mathbf{v}^j_{residual}}{N-j} \qquad i = 2, ..., N \tag{8.3}$$

The sub-targets are then, given that their residuals will update the following ones, a sort of guiding light for the design of each single flyby. Here lies the main feature of drastically reducing the combinatorial nature of the problem, solving the non-smooth optimisation that leads to the optimal set of brute-force designed resonant deflections.

8.2.3.3 *Optimal resonance choice*

Given a set S of resonances, for a specified sub $\Delta\mathbf{v}$ the algorithm finds the best resonant trajectory whose deflection gets the closest to the sub-target. This happens on another 2-level optimisation local algorithm that works as follows:

1. Select one of the resonances in S.
2. Find the point on the resonant circle, according to some deflection model detailed in the following subsections, of such a resonance that gives the best $\Delta\mathbf{v}$.
3. Loop over all the admissible resonances and pick the best $\Delta\mathbf{v}$.
4. Store the detailed data of such a resonant trajectory.

Some constraints are anyway needed, to bound the trajectories in a feasible region (i.e. the impact parameter must be at the same time not too low and not too high, $b_{min} \leqslant b \leqslant b_{max}$).

8.2.3.4 *Deflection model*

The core, and lowest level, of the proposed algorithm and approach is the deflection model implemented in the design of optimal flybys.

Each deflection is modelled by using the b-plane formalism, with the presented notation and not specifically defined quantities used to follow [30]. The two deflection cases need to be distinguished for the first step, i.e. locating the b-plane coordinates ξ and ζ, for resonant and free flybys: a specific resonance acts as by imposing a constraint on the position on the b-plane, namely the point must belong to a circle of centre's $\hat{\zeta}$ coordinate D and radius R. Identifying with α a counter-clockwise angle measured from the $\hat{\xi}$ direction (exactly as the angle in simple polar coordinates), given D and R a generic point features:

$$\begin{aligned} \xi &= R\cos\alpha \\ \zeta &= D + R\sin\alpha \end{aligned} \tag{8.4}$$

and the impact parameter defined as

$$b^2 = \xi^2 + \zeta^2 \tag{8.5}$$

whereas for a non-resonant case such coordinates are obtained by

$$\begin{aligned} \xi &= b\cos\alpha \\ \zeta &= b\sin\alpha \end{aligned} \tag{8.6}$$

with b to act directly as the radius variable in b-plane polar coordinates. Note that the non-resonant case removes the constraint of the b-plane point to be located on a resonant circle, although having one more degree of freedom on b. Another slight difference between the free

and resonant flybys is the way to include the constraint on the impact parameter: since b is one of the optimisation variables in the free case, it is enough to set lower and upper boundaries for b to get $b_{min} \leqslant b \leqslant b_{max}$, whereas the resonant case for given D and R has α as the only variable, and thus will feature a non-linear constraint built upon Equations (8.4) and (8.5) to check that b remains within the specified boundaries.

On the b-plane it is fairly easy to model the deflections, γ can be computed as in [30]:

$$\cos\gamma = \frac{b^2 - c^2}{b^2 + c^2} \tag{8.7}$$

The rotation direction, thus a principal rotation vector, lies on the b-plane and its orientation is strictly linked to the angle ψ, defined as:

$$\begin{aligned} \cos\psi &= \frac{\zeta}{b} \\ \sin\psi &= \frac{\xi}{b} \end{aligned} \tag{8.8}$$

This paragraph just re-phrases what presented in Subsection 5.3.1.

Particularly, with the planetocentric velocity pointing towards the b-plane, as defined in Equation (8.8) the angle ψ measures a clockwise rotation from the $\hat{\zeta}$ direction to the b-plane point itself, plus the velocity vector will be always rotated towards the centre of the plane. This implies that one of the possible deflection direction computation strategies is to rotate the direction $-\hat{\zeta}$ counterclockwise on the downside b-plane of an angle $\psi + \pi/2$.

With the rotation direction (given by ψ) and its magnitude (γ), to rotate the cartesian ingoing planetocentric velocity $\mathbf{U}_i$ into the outgoing one $\mathbf{U}_i'$ at the i-th flyby it is then enough to follow these steps:

1. rotate $-\hat{\zeta}$ on the downside b-plane counterclockwise of $\psi + \pi/2$;
2. represent this new vector in the cartesian reference frame (rotation matrix straight from the b-plane axes definition in Equation (4.5));
3. together with γ, this will build the principal rotation vector in the cartesian reference frame;
4. apply the rotation to $\mathbf{U}_i$;
5. compute $\Delta\mathbf{v}^i = \mathbf{U}_i' - \mathbf{U}_i$.

Defining the residual of flyby i as

$$\Delta\mathbf{v}^i_{residual} = \Delta\mathbf{v}^i_{sub-target} - \Delta\mathbf{v}^i \tag{8.9}$$

at the lowest level, the optimisation process will select a solution where the quantity $\|\Delta\mathbf{v}^i_{residual}\|^2$ is minimised. For the last free flyby the best coordinates (b, α) will be selected, whereas for a resonant flyby only the coordinate α together with the correspondent circle parameters will be chosen and saved.

8.3 PERTURBED RESONANCE DESIGN

Given that the perturbed semi-analytical model available still relies on a strictly 2-body patched conics definition of resonance, to feature the resonant return the deflection must still comply with such a definition. Therefore, the perturbed $\Delta\mathbf{v}$s are computed so that their difference with respect to the already optimised 2-body deflections is minimised. Note that such a $\Delta\mathbf{v}$ is not meant to be a manoeuvre to be implemented, in the current analysis it has only the purpose of showing the difference between perturbed and unperturbed case.

The semi-analytical model developed in this work applies the perturbing effects in terms of corrective elements to be included in the analytical deflection. Since in design applications a reference sample does not exist, some strategy to map the perturbing effects on the b-plane is required. As experienced in Section 6.2, mapping the perturbing effects reduces the deflection error nearby the point used for their computation, with higher magnitude errors observed for lower impact parameters. Such effects are then mapped on the b-plane before designing the flyby, with a thicker mesh close to the planet, and then interpolated to obtain the perturbing values not exactly at the map nodes, in order to exploit the deflection model to avoid to carry out numerical propagations at each step of the optimisation process.

A set of simulations is then performed at the beginning of the design itself: the starting conditions are identified by the b-plane polar coordinates $(b_{min} \leqslant b \leqslant b_{max},\ 0 \leqslant \alpha < 2\pi)$, thus with their correspondent (ξ, η, ζ) positions at the entrance of the sphere of influence, and the ingoing planetocentric velocity of the current flyby. All these points together will build a mesh (Figures 8.1 and 8.2), whose propagation will bring the following set of parameters at each node, computed in the same way as in Section 5.3:

- the perturbation $\Delta\gamma$ on the deflection magnitude;
- the perturbation $\Delta\psi$ on the deflection direction;
- the perturbation $\Delta\theta'$ on the outgoing angle between the planet's and the object's planetocentric velocities;
- mesh-related handle quantities for the interpolation.

Note that, similarly to what discussed in Section 6.2, once the mesh point is propagated the perturbation $\Delta\theta'$ is redundant for the deflection modelling, thus it will be used for the identification of the resonant loci of points to be then deflected according to the perturbations on γ and ψ only. The different α angles are linearly spaced one another, whereas b features a quartic distribution between b_{min} and b_{max}. Note that, as shown in Figures 8.1 and 8.2, the quartic distribution on b has been chosen arbitrarily to reach a thicker mapping nearby the lower limit, where the difference between two values of b

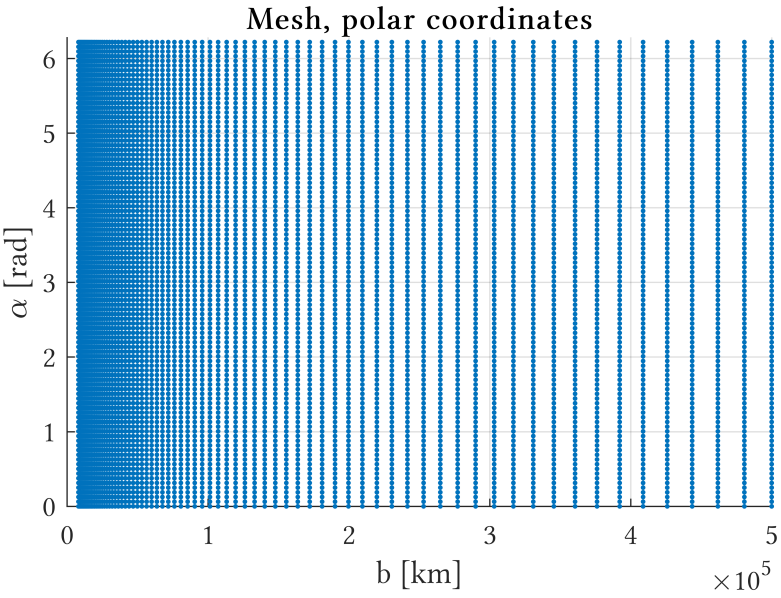

Figure 8.1: Mesh example in b-plane polar coordinates.

has an higher impact on the deflection error (Section 6.2). A quartic distribution may not be the best choice, some further analyses could deepen the focus on this topic in order to reach an optimised map building strategy. Nevertheless, it is not performed here since way beyond the demonstration scope of building a first resonant ballistic flyby design method. Such a map features in all the cases 100 evenly spaced elements between 0 and 2π for the angular coordinate, 100 map elements between b_{min} and b_{max}, identified respectively by the impact region of the current planet and a reasonable high altitude flyby (5×10^5km for Earth and 3×10^5km for Venus in the test cases presented)[3].

Despite the reason of mapping the whole domain is fully evident in the free flyby case, in principle for the resonant close approaches, if the b-plane region enclosing a specified resonance was to be known, there would not be the need of propagating such a whole mesh and the domain could be restricted to the interest areas only. Nevertheless, in the current application, one must remember that not only the position of the resonant circles at a specified close approach is not known, but also that all the configurations of the intermediate encounters are let free, leading to even more uncertainties than the sole circle location. For the current implementation some computational cost could be cut by using the optimal 2-body result to identify the interest areas in the N-body analysis, however, if the goal was to detach from the patched

3 Note that such a distribution with 100 mesh points within 8×10^3 km $\leqslant b \leqslant 5 \times 10^5$ km stays already in the well approximated regions highlighted in Secton 6.2. Some higher differences may be experienced at the highest altitudes, whereas the inter-node distance for points close to the planets is already in the order of 50/100 km, expected to be robust enough for the purposes of this work.

conics approximation, a complete mapping would be anyway needed to include the perturbing effect, since the optimisation may be run already at the perturbed level.

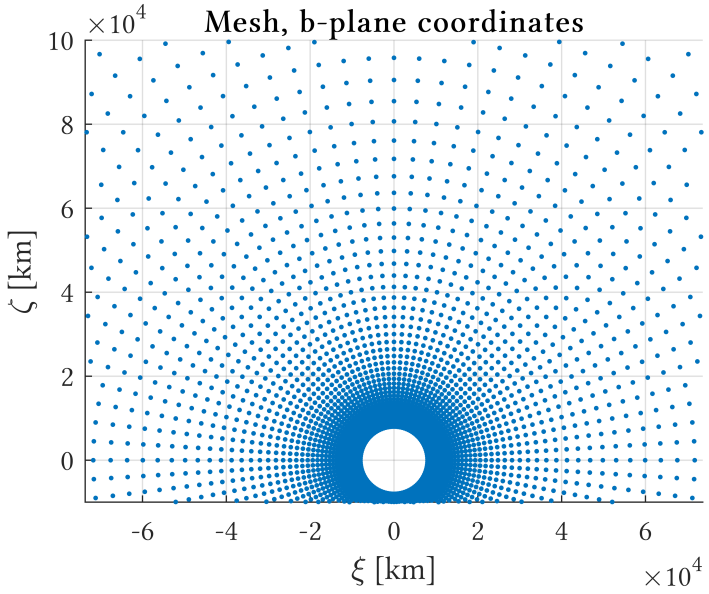

Figure 8.2: Mesh representation in b-plane coordinates. As already mentioned, the b-plane representation allows to visualise the enhanced mesh thickness given by the quartic distribution of b nearby the lower boundary.

The interpolation strategy is inspired to a bi-linear lagrange-polynomials, interpolating over b and the arc $b\alpha$. The four interpolation coefficients are then given by

Note that the interpolation will be still bi-linear on impact parameter and arc, albeit linearity is lost on the sole variable b.

$$l_{ij}(b,\alpha) = \frac{b - b_i}{b_j - b_i}\frac{b\alpha - b_i\alpha_i}{b_j\alpha_j - b_i\alpha_i} \tag{8.10}$$

with i, j to be the indexes identifying the nodes of the cell enclosing b and α.

8.3.1 *Resonant flyby design*

Sticking to what presented in Section 6.3, a complete use of the perturbed deflection model to draw the new resonant circles is made(i.e. to compute the perturbed circle parameters D_p and R_p), and then the same optimisation process (Subsection 8.2.3.3), constraints and deflection (Subsection 8.2.3.4) depicted in the two body case are applied, with the only difference to include the perturbing angles $\Delta\gamma$ and $\Delta\psi$ in the deflection computation.

Being in a design phase and having mapped the perturbing effects on the b-plane, there is no need to pick one node only as the reference to draw the perturbed resonant circles, whose approximation looses accuracy far from the reference. Since in general the position of the

circle intersection with the $\hat{\zeta}$ axis is not known, some iteration method is required. A fixed-point-iteration-like algorithm is proposed here, detailed as follows:

1. initialise the search by computing the unperturbed circle parameters D and R;
2. compute the highest magnitude intersection b with the $\hat{\zeta}$ axis;
3. get the interpolated perturbing angles $\Delta\gamma$, $\Delta\psi$ and $\Delta\theta'$ at such a point;
4. compute the perturbed circle parameters D_p and R_p and get the updated intersection b_{new} with the $\hat{\zeta}$ axis;
5. if the difference between the current b_{new} and the previous iteration's one (equal to b when initialising the algorithm with the unperturbed case) is lower than some tolerance stop the algorithm, otherwise return to step 3.

Since the intersection with the $\hat{\zeta}$ axis can be either positive or negative, the search is performed consistently in the correspondent semi-b-plane.

Given the thickness of the map implemented and the result of the deflection validation (Section 6.2), a fast convergence is expected, since the perturbing coefficients do not differ much in a vast region nearby the node. In fact, despite having set a rather strict tolerance of 10^{-6}km for the difference between two iterations and a maximum of 1000 steps, such a number was never reached and convergence happened in all the test cases analysed.

Note that such a model does not take into account possible different values of the perturbation $\Delta\theta'$ and still assumes the resonant loci of points to be described by circles. A possible generalisation performs the optimisation over both the variables (b, α) of the free flyby and relaxes the circle approximation of the perturbed resonances, but still makes use of the perturbing coefficients to insert the following nonlinear constraint based on the perturbed resonant geometric deflection:

$$\begin{aligned} &\cos\theta_0'^{*} - \cos(\gamma+\Delta\gamma)\cos\theta^{*} - \\ &\sin(\gamma+\Delta\gamma)\sin\theta^{*}\cos(\psi+\Delta\psi) = 0 \end{aligned} \tag{8.11}$$

The definition of $\cos\theta_0'^{*}$ is the one given in Equation (5.15), the different b-plane positions affect the theoretical angles γ and ψ as in Equations (8.7) and (8.8)

Basically the claim that such a deflection must bring a circular locus of points in the b-plane (whose parameters were identified by the two intersections with the $\hat{\zeta}$ axis in Section 5.3) is abandoned, accounting for possible different angles $\Delta\gamma$, $\Delta\psi$ and $\Delta\theta$ in the various b-plane positions to be obtained via map interpolation.

An attempt of optimising the deflection with such a generalised resonance has been made, although the new setup has not converged to an optimal solution. The results reported in Chapter 9 involve only the circular resonance model, a further analysis to find a suitable method for the generalised resonance optimisation is required.

8.3.2 *Last free flyby design*

The perturbed last free flyby is let free of any constraint, to get as close as possible to the desired final orbit. A difference with respect to the resonant perturbed flybys is that the optimisation can be let free to comply with the ultimate deflection required, since there is no 2-body resonant $\Delta\mathbf{v}$ to be fulfilled. Yet again the deflection model acts in a similar way to the resonant one but having both b and α as optimisation variables, featuring the same deflection algorithm presented in Subsection 8.2.3.4 accounting for the interpolated perturbing effects $\Delta\gamma$ and $\Delta\psi$, obtained by the map propagated before the flyby design. The domain is initially restricted by finding the map region nearby the point that get closest to the target, with a sequence of direct search and descent method refinement run to get the best deflection interpolating the map parameters.

9

TEST CASES AND RESULTS

9.1 INTRODUCTION AND COMMON FRAMEWORK

The algorithm presented in Chapter 8 has been applied to other general test cases, designing from 2 to 7 resonant flybys, of which only two particularly meaningful of them are reported here. They will be introduced with its initial orbit, the target orbit and the number of flybys that the solver is asked to design. The sequence of resonant orbits designed will given, as well as the b-plane coordinates at each close approach.

For all the cases the optimisation has been performed with MATLAB® and SPICE ephemerides[1], using the function `patternsearch.m` at the highest level (optimal $\Delta\mathbf{v}$ target search) and a multistart `fmincon.m` for the unperturbed b-plane deflections, since the formulation is non-convex albeit smooth enough to allow descent method to converge if starting from a good enough initial guess. In general, for the perturbed model the interpolation of the perturbing parameters makes the problem non-smooth even at the planetocentric design, thus a `patternsearch.m` optimisation is implemented at this level as well, with an `fmincon.m` refinement performed on the direct search optimal solution.[1]

9.2 GENERAL, SIMPLE BUT MEANINGFUL CASE AT EARTH LEVEL

The first case used to test the solver is conceptually simple, but already an interesting test for the physics upon which the optimisation process is based. Indeed, the solver is asked to find a 2-flyby ballistic solution for a deflection impossible to achieve with a simple close approach. The initial condition is Earth's position on 01 January 2020 at midnight,

1 `fmincon.m` is a function available in MATLAB® optimisation toolbox that implements several algorithms, among which the interior point method is always chosen in the cases presented. `patternsearch.m` is instead a function available in the global optimisation toolbox, implementing a direct search algorithm with smart mesh definition and update. It is used for its gradient-free features, for a global optimality search at the highest level and to provide good enough starting guesses for `fmincon.m` refinements in the deflection design.

with the two orbits, denoted with subscripts 0 for the initial and f for the final, in a heliocentric ecliptic J2000 reference frame defined as

$$\mathbf{r}_0 = \mathbf{r}_{Earth} = \mathbf{r}_f = \begin{Bmatrix} -0.1663 \\ 0.9691 \\ 0.0000 \end{Bmatrix} \text{ AU}; \qquad \mathbf{v}_{Earth} = \begin{Bmatrix} -29.8489 \\ -5.1623 \\ 0.0000 \end{Bmatrix} \frac{\text{km}}{\text{s}};$$
$$\mathbf{v}_0 = \begin{Bmatrix} -33.8489 \\ -4.1623 \\ -2.9999 \end{Bmatrix} \frac{\text{km}}{\text{s}}; \qquad \mathbf{v}_f = \begin{Bmatrix} -25.8489 \\ -6.1623 \\ 2.9999 \end{Bmatrix} \frac{\text{km}}{\text{s}}; \tag{9.1}$$

and highlighting the asymptotic conditions and the total deflection required

$$\mathbf{v}_\infty^0 = \begin{Bmatrix} -4 \\ 1 \\ -3 \end{Bmatrix} \frac{\text{km}}{\text{s}}; \qquad \mathbf{v}_\infty^f = \begin{Bmatrix} 4 \\ -1 \\ 3 \end{Bmatrix} \frac{\text{km}}{\text{s}}; \qquad \Delta\mathbf{v}_{tot} = \begin{Bmatrix} 8 \\ -2 \\ 6 \end{Bmatrix} \frac{\text{km}}{\text{s}}; \tag{9.2}$$

As already mentioned such a deflection is impossible to achieve in a single, hyperbolic, ballistic close approach, since it would require a turn angle equal to π. The resonance set S involves all the possible combinations of (k, h), for both Earth and the fictitious small object, between 1 and 10.

9.2.1 *Optimal unperturbed solution*

The algorithm converged to a ballistic optimal solution, obtaining a $\Delta\mathbf{v}_{res}$ after the last flyby whose norm is on the order of 10^{-8} km/s. The intermediate orbit features a $k/h = 8/7$ resonance, with the flyby providing a deflection $\Delta\mathbf{v}_i = \{4.035, -6.079, 3.439\}^T$ km/s, whereas the last free close approach that gives the remaining contribution $\Delta\mathbf{v} = \{3.965, 4.079, 2.561\}^T$ km/s.

The orbit evolution is reported in Figure 9.1 and Table 9.1, with the subscript i to identify the intermediate orbit.

	a [AU]	e [–]	i [rad]	Ω [rad]	ω [rad]	θ [rad]
Initial	1.4029	0.3025	0.0878	4.8819	2.9372	0.2049
Resonant	1.0947	0.1891	0.0141	1.7438	1.1688	5.1114
Final	0.8144	0.2165	0.1127	1.7412	2.9067	3.3761

Table 9.1: As a further design check, comparing the ratio $(a_i/a_{Earth})^{3/2} = 1.1453$ with $k/h = 8/7 = 1.1429$ proves the intermediate orbit to be resonant, with the small difference due to floating point issues.

A visual check of the intermediate resonance $k/h = 8/7$ is possible in Figure 9.1, with pretty similar sizes of that orbit and Earth's one.

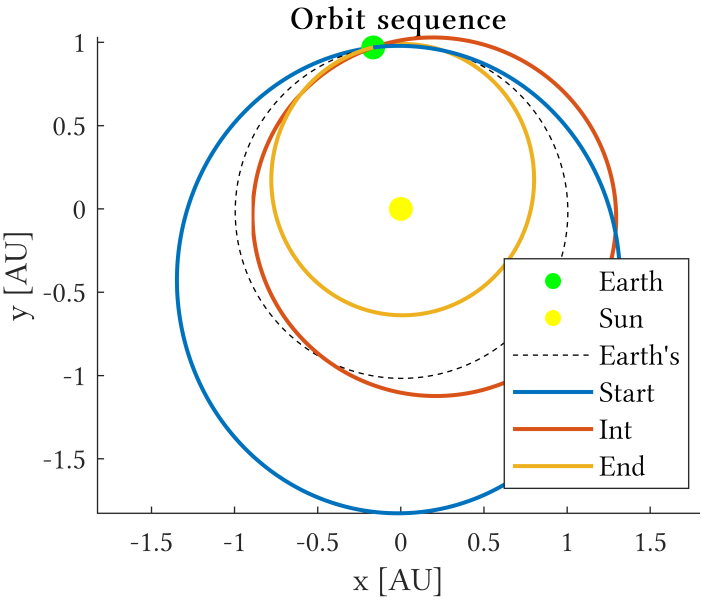

Figure 9.1: Interplanetary trajectories followed in the two-flyby general case.

Comparing the semi-major axis ratios from Table 9.1, $(a_i/a_{Earth})^{3/2} = 1.1453$ with $k/h = 8/7 = 1.1429$ proves the intermediate orbit to be resonant, with the small difference due to floating point issues. Note that the algorithm involves several rotation matrices and trigonometry functions, thus a simple floating point explanation is reasonable for such a small difference between T_i/T_{Earth} and k/h.

The only possible solution to this issue would be an analytical formulation refinement of the algorithm assisting and avoiding such computations whenever possible.

9.2.2 *Optimal perturbed solution*

The algorithm designed the optimal N-body trajectories according to the deflection model introduced in this work, again targeting the 2-body optimal deflections in order to comply with the current definition of resonance. Note that the algorithm is let free to choose among all the possible resonances even in this case, thus a different resonance chosen would highlight a remarkable difference between the perturbed and unperturbed resonant circles for the current b-plane. In this case the choice of the resonance has slightly changed to $k/h = 9/8$: such a circle is the one that, nearby the 2-body optimal solution, closest resembles the unperturbed one, in order to both accommodate the constraint of lying on a perturbed resonant circle and to try to get as close as possible to the point providing the best deflection (as shown in Figure 9.2). The optimal perturbed deflection is anyway close to the unperturbed one, with the perturbing effects that do not severely affect the optimal deflection region.

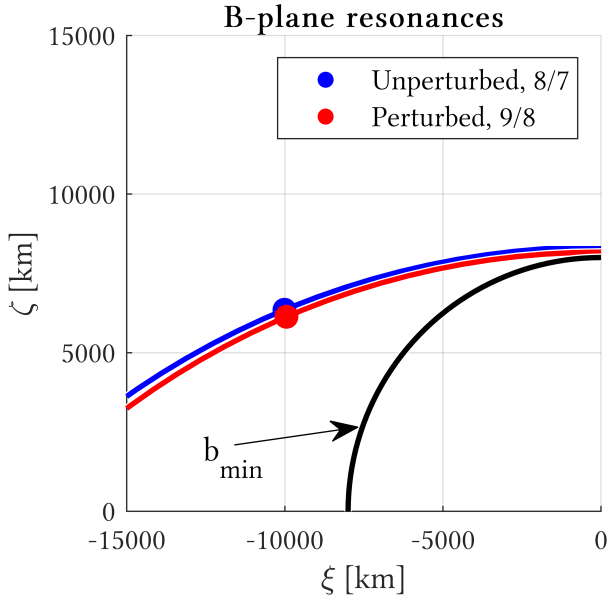

Figure 9.2: B-plane coordinate and circles of the deflection selected.

The resonant deflection is slightly different than the unperturbed case with $\Delta\mathbf{v}^{i}_{res} = -\{0.071, 0.011, 0.102\}^{T}$ km/s, mainly due to the constraints introduced, whereas the residual left on the free flyby is in the order of 10^{-6}km/s, compatible with the added degree of freedom left for its design.

Providing a further check to the deflection model, such a map led to a maximum error of 0.177 km/s, experienced on the resonant flyby with respect to the post-processed trajectory propagated with the design optimal solution as initial condition. Despite being already small if compared to the magnitude of the whole deflection (equal to 8.138 km/s, for a 2.169% relative error), whether a higher precision level was required it would be enough to implement a thicker mesh, allowing for necessarily larger computational times. Indeed a test was run to this extent, mapping the b-plane with a 3 times thicker mesh led to basically the same optimal results, with an error model/simulation of 1.142%. Nevertheless, still using the initial map, an error of only 0.8% is obtained with respect to the propagated deflection for the free flyby, likely due to a better approximation on the free flyby b-plane region.

9.3 SOLAR ORBITER-LIKE OPTIMISATION

As a second meaningful validation test, the solver will be asked to search for an optimal solution about designing resonant flybys similar to Solar Orbiter's [12] ones about Venus. Such trajectories are used to raise the orbit's inclination with low cost manoeuvres, exploiting repeated close approaches of Venus. The solution is expected to slightly

differ from the designed one, since the algorithm for now designs ballistic flybys only. In any case, reaching a solution similar to the already optimised ones available in Solar Orbiter's mission plans would give a strong proof of the proposed design approach.

The reference case will be the solution proposed with launch in January 2017 in [2], even though the whole mission has been eventually postponed to 2020. The optimised trajectory just mentioned is available in Figure 9.3. The algorithm will be asked to reproduce the resonant flybys, namely a solution similar to what here identified between V2 and V6.

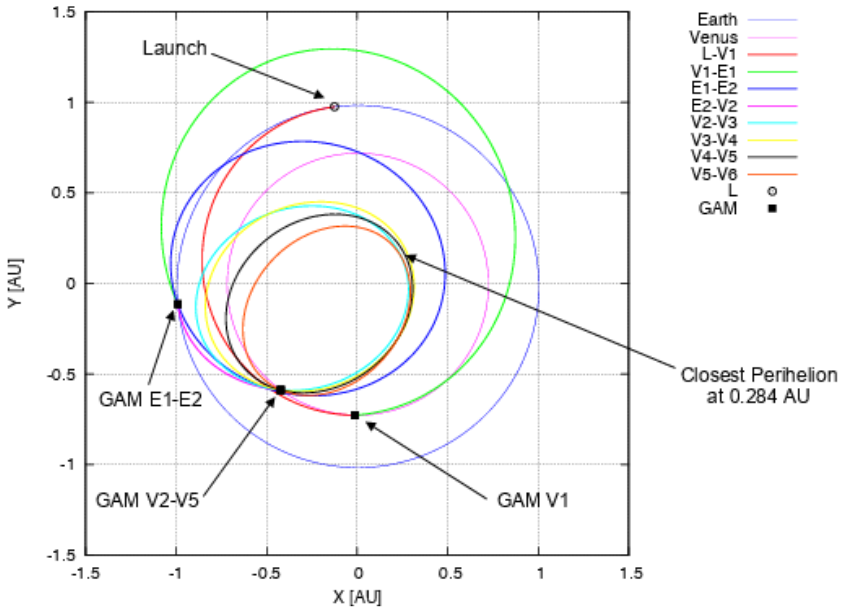

Figure 9.3: Optimised, final orbit sequence for the January 2017 Solar Orbiter's mission plan. Picture from [2].

The main features [2] of the four resonant orbits are reported in Table 9.2, with the first flyby to happen on 22/05/2020. The resonances designed are also specified in [2], namely $(3/4, 3/4, 2/3, 3/5)$ in that order. The notation used to identify the different close approaches is the same introduced in [2], namely Vi stands for the i-th flyby of Venus and $Vi - Vj$ refers to the heliocentric orbit between the flybys i and j. Note that the orbits are actually uniquely defined, since the position of Venus at each specified time adds the three remaining parameters.

Note that, being the design fully ballistic, some of the mission constraints, especially keeping perihelion and aphelion altitudes within specified boundaries, must be removed, since they would not be achievable without manoeuvres. In fact, the Tisserand parameter of the initial orbit is $T_0 = 2.724$, whereas the final orbit features $T_f = 2.922$, making it impossible to ballistically comply with all those properties. The solver will be therefore asked to perform the specified change in

Orbit	Aphelion [AU]	Perihelion [AU]	Ecl. Incl. [°]
Initial	0.998	0.311	1.72
V2 – V3	0.910	0.284	9.93
V3 – V4	0.870	0.315	18.11
V4 – V5	0.789	0.315	23.83
V5 – V6	0.740	0.290	27.25

Table 9.2: Orbital parameters of the resonant orbits for Solar Orbiter's January 2017 mission profile [2].

inclination in the same number of flybys, letting all the parameters to adjust autonomously. In any case, the solution is expected not to differ much from the optimal one reported in [2]. Given the optimal resonances mentioned above, the algorithm will this time select (k, h) values only within 1 and 5. Initial and final orbits for the optimisation prolem are then reported in Table 9.3. These two orbits feature the same Tisserand parameter. Note that the specified target is not a 3/5 resonant orbit, which is not ballistically achievable for the specified final inclination. The remaining two target parameters have been chosen so that an orbit with similar perihelion and aphelion is reached.

Orbit	Aphelion [AU]	Perihelion [AU]	Ecl. Incl. [°]
Initial	0.998	0.311	1.72
Final	0.738	0.320	27.25

Table 9.3: Initial and final orbit parameters given as input to the optimisation algorithm.

and the total deflection required is

$$\Delta \mathbf{v}_{tot} = \left\{ \begin{array}{c} -10.544 \\ -7.553 \\ 13.381 \end{array} \right\} \frac{km}{s}. \tag{9.3}$$

9.3.1 *Optimal unperturbed solution*

The algorithm converged to a ballistic optimal solution, obtaining a $\Delta\mathbf{v}_{res}$ after the last flyby whose norm is again on the order of 10^{-8} km/s. The four deflections are

$$\begin{aligned} \Delta\mathbf{v}_1 &= \begin{Bmatrix} -2.067 \\ -0.167 \\ 3.862 \end{Bmatrix} \frac{\text{km}}{\text{s}}; & \Delta\mathbf{v}_2 &= \begin{Bmatrix} -2.888 \\ -1.259 \\ 3.807 \end{Bmatrix} \frac{\text{km}}{\text{s}} \\ \Delta\mathbf{v}_3 &= \begin{Bmatrix} -3.719 \\ -2.367 \\ 2.882 \end{Bmatrix} \frac{\text{km}}{\text{s}}; & \Delta\mathbf{v}_4 &= \begin{Bmatrix} -1.870 \\ -3.760 \\ 2.830 \end{Bmatrix} \frac{\text{km}}{\text{s}}; \end{aligned} \tag{9.4}$$

and the orbits designed are reported in Figure 9.4, with their parameters in Table 9.4. The intermediate orbits feature resonances $(3/4, 2/3, 3/5)$ and as already briefly mentioned the last orbit was let free, to comply with the final inclination to reach and obtain a similar overall shape, albeit the last orbit reported in Table 9.2 is still in a 3/5 resonance. As a visual check, the algorithm has produced orbits pretty similar to the optimised ones of Figure 9.3. Also the orbital parameters obtained are similar, apart from the perihelion distance which appears to be, reasonably considering the purposes of the mission itself [12], the main objective of control manoeuvres.

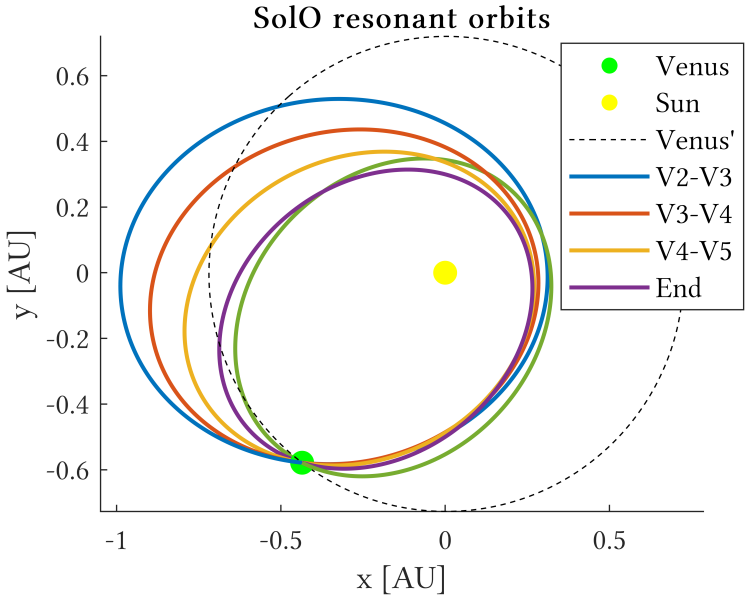

Figure 9.4: Interplanetary trajectory computed by the optimisation algorithm.

Note that only the first one out of three resonances correspond to the ones designed in [2]. The main possible explanation is the absence of manoeuvres and mission constraints in the optimisation algorithm,

Orbit	Aphelion [AU]	Perihelion [AU]	Ecl. Incl. [°]
Initial	0.998	0.311	1.72
V2 – V3	0.914	0.281	7.17
V3 – V4	0.838	0.267	15.68
V4 – V5	0.771	0.259	22.60
Final	0.738	0.320	27.25

Table 9.4: Interplanetary orbital parameters for the trajectories computed by the optimisation algorithm.

that for instance leads to perihelion distances too low compared to the constraints specified in [2].

9.3.2 *Optimal perturbed solution*

The chosen resonances remain in this case all compliant with what designed in the two body optimisation, i.e. the ratios k/h stay unchanged. Again as shown in Figure 9.5 the perturbed points chosen are the ones that get the closest to the optimal unperturbed b-plane coordinates. For the sake of conciseness all the resonant flybys are reported in the same plot, although the b-plane reference frame itself has a different orientation for each single close approach.

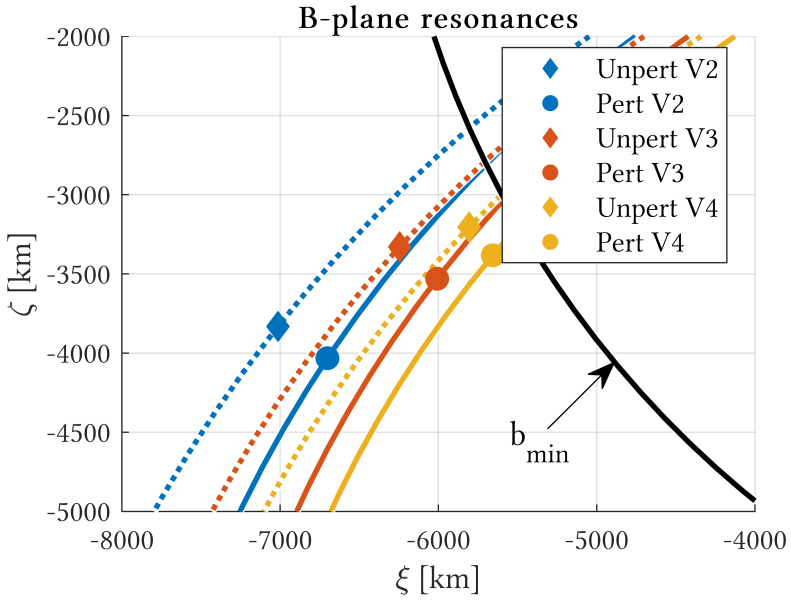

Figure 9.5: B-plane coordinates and circles of the resonant close approaches.

All the resonant deflections feature some residual, compatibly due to the constraint of lying on their b-plane circles:

$$\Delta\mathbf{v}^1_{res} = \begin{Bmatrix} 0.192 \\ -0.031 \\ -0.003 \end{Bmatrix} \frac{km}{s}; \qquad \Delta\mathbf{v}^2_{res} = \begin{Bmatrix} 0.195 \\ -0.021 \\ 0.039 \end{Bmatrix} \frac{km}{s} \qquad (9.5)$$
$$\Delta\mathbf{v}^3_{res} = \begin{Bmatrix} 0.137 \\ -0.027 \\ 0.078 \end{Bmatrix} \frac{km}{s};$$

As in the previous case, the residual on the last free flyby is in the order of 10^{-6}km/s.

Providing a further and final check to the deflection model, the maximum error is experienced in the third flyby, equal to 0.628% with respect to the simulated trajectory. This suggests that the chosen mesh is more accurate than the previous case studied, despite the equal number of elements. Intuitively it appears that stronger gravitational fields require a much thicker mesh, although a thorough verification is needed to confirm the claim.

9.4 PERFORMANCES

All the upcoming machine times are referred to a local computer, for computations carried out in MATLAB® parallelised onto two CPUs at 2.7GHz.

9.4.1 *Unperturbed design*

The heaviest part from the computational point of view is the target selection, indeed `patternsearch.m` implements an intelligent direct search method, although that still needs to perform several function evaluations at each algorithm iteration. For large domains and small tolerances this turns into a rather high computational time, due to the optimal targets not being known at all. An extremely small computational time is experienced when the algorithm is ran again for retrieving the complete solution, of only 1.5s for the design of Solar Orbiter's flybys. A slightly higher time, 4.1s, is experienced in the general cased detailed in Section 9.2, mainly due to the higher number of resonances available in the set.

9.4.2 *Perturbed design*

In order to underline the performances of the deflection model itself, the performance focus is put here on the local computations, whose time mentioned below include the numerical simulation of the selected

trajectory. The heaviest part is indeed the map generation, for higher machine times associated obviously with higher thicknesses. If the map is given again an extremely fast convergence is experienced, for about 2.7s in both last free flybys the cases presented, 1.9s for a resonant close approach in the Solar Orbiter case and of 4.5s in the general case, again due to the higher number of resonances analysed. Such numbers are remarkable if combined with the precision level reached and the software used, a full transition to better programming languages could easily tackle such design problems with higher precision and even lower computational times.

10

CONCLUSION AND OUTLOOK

A first draft of efficient algorithm for the design of resonant orbits using the b-plane formalism has been succesfully implemented. The solution given when trying to replicate Solar Orbiter's already optimised trajectory, for a close fully ballistic result which is yet to include manoeuvres and mission constraints, is particularly meaningful. In the way it currently stands the algorithm is already suitable for mission analysis purposes, in the cases where orbital resonances are exploited in a 2-body sense and obtaining also an idea about how the perturbed deflection behaves.

Such a tool is however strictly linked to the model it uses, which, as already mentioned in the previous part of this work, is yet to be completed, particularly for what concerns the current resonance definition. What then needs to be taken away from the perturbed design section is the capability of the deflection model to comply with a target and the perturbed b-plane definition of resonance, which will see some updates with the model developments but will not change in their main structure. In other words, an extended definition of resonance, detaching from the pathced conics approximation, could perhaps modify the circle parameters or their shape on the b-plane, without however affecting the design capabilities of the algorithm since they are always implemented as a constraint to fulfill.

About the algorithm itself, some work needs still to be done to reach a final form, especially studying the possibility of adaptive/smart mesh designs that would lower the computational cost and at the same time enhance the precision where required. Despite it already appears to be rather efficient in all the test cases analysed, a more thorough analysis on the optimisation strategy could be performed, in order to either confirm the existing choice or offer some better solution. As final remark, some work should be spent towards studying the convergence of the algorithm implementing the resonance as a real deflection constraint, rather than the correspondent locus of points on the b-plane. It is true that in all the test cases considered in Part ii such circles seem to well approximate the orbital resonances, enhancing also the computational speed due to the lower number of degrees of freedom, nevertheless a more detailed study would even in this case either confirm the choice or suggest the need of a more general

implementation. A smart approach could be considered as well, with the algorithm eventually capable of distinguishing itself whether the circle approximation is good or not.

Part IV

FINAL CONCLUSION AND OUTLOOK SUMMARY

11

FINAL CONCLUSION

An interesting outcome can be found in the benchmark development part, where an efficient formulation to account for general relativity effects in the N-body dynamics has been developed. The real efficiency stands in the precision of the achieved results, for exact computations of the relativistic accelerations under the most general parametrised post newtonian mechanics context. Such a model could then be implemented for any sort of application, opening the possibility of extreme precision numerical studies.

The precise identification of the resonant loci of point in the b-plane reference frame successfully brought a semi-analytical modification of the current model, reaching an exact solution, in terms of simulation compliance, at the b-plane point where the perturbing coefficients have been computed, providing also a highly reliable approximation in the nearby b-plane regions. The immediately next developments already comply with the planetary protection application needs, namely studying the actual impact of plotting a full Monte Carlo simulation on the same b-plane representation. The model should eventually detach from the patched conics approximation and then generalise the proposed semi-analytical solution, to account for the variations of the perturbing parameters among different b-plane regions. To this extent, some focus should be put towards both exploring optimal mapping strategies and new analytical solutions, in order not to waste the efficiency features reached so far and to guarantee an in-b-plane precise impact/resonance probability computation for planetary protection and defence analyses.

Finally, the deflection modelling capabilities of the b-plane formalism have been shown by implementing an efficient ballistic resonant trajectory design algorithm. The main outcome of such an application is perhaps having showed once again how embedding and connecting different orbital representations could enhance the algorithm performances, namely using the b-plane features for the deflection design, the traditional keplerian elements for the objective definition and the simple cartesian representation to carry out rather easy computations. The results achieved by the algorithm, particularly the Solar Orbiter-like optimal ballistic solution in terms of both precision and computational resources required, suggest again to keep developing

both the model and the method. On one hand, the restriction to resonant flybys drastically reduced the number of degrees of freedom left to the problem, main reason for such low computational costs, highlighting that proper analytical or semi-analytical developments, such as optimal perturbation mapping strategies and in-b-plane manoeuvre design, could lead to application extensions to the non-resonant case. On the other hand, optimal trajectory design techniques already exist, thus the proposed method could contribute in increasing the functionalities of the current procedures, from which it could also take and embed other mathematical and physical tools for its own development.

Part V

APPENDIX

A

INTRODUCTION TO GENERAL RELATIVITY

A.1 INTRODUCTION

Newtonian mechanics provides quite an accurate description of what happens to point-mass objects in space, how they move and how they interact. The purely Newtonian models can sometimes be adjusted, taking into account the effect of several orbital perturbations (J2 Oblateness, Solar Radiation Pressure, etc.). In very peculiar cases general relativity (GR) plays an important role, which can not be neglected if high precision computations are needed.

In this chapter a collection of the key and the introductory concepts necessary for a broad understanding of GR will be presented. The main reference will be [35], the classical tome used to tackle consistently GR, although the contents will be presented sorted differently, with the purpose of highlighting what is of key importance from an application point of view.

A.2 SPECIAL RELATIVITY (SR)

In this section a brief summary of the principles of special relativity (SR) is collected, following what is presented on [35] and on [4]. The concepts of SR are fundamental to understand completely its generalisation, GR.

A.2.1 *Principles and concept of time*

It was Einstein who first developed this theory, trying to explain some apparently wrong phenomena description, e. g. Maxwell's equations: the mathematical formulation underlines an asymmetric behaviour, which is not consistent with observations and experiments. The most simple example to underline this phenomenon is the interaction between a magnet and a conductor, represented in Figure A.1 and expressed with Equations (A.1) and (A.2). The relative motion gives different results in terms of electromotive force (F_{e-m}), if the body considered moving is the conductor, with a velocity **v** (Equation (A.1)) or the magnet with a velocity **-v** (Equation (A.2)).

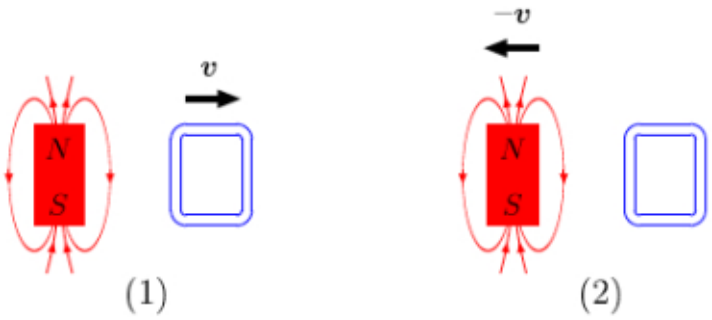

Figure A.1: Picture of the relative motion issue in Maxwell equations. Source [4].

$$\mathbf{F}_{magn} = e\mathbf{v} \times \mathbf{B} \qquad \mathbf{F}_{el} = e\mathbf{E}$$
$$F_{e-m} = \int (\mathbf{v} \times \mathbf{B}) \cdot d\mathbf{l} \quad (A.1) \qquad F_{e-m} = \int \mathbf{E} \cdot d\mathbf{l} \quad (A.2)$$

Despite the usual description leading to two completely different results, the observed reality is only dependent on the relative motion of the source (magnet) and the conductor.

Indeed the basic, well known principle (first postulate of SR) is:

Different observers (inertial reference frames) provide different descriptions of the same phenomenon, but the considered physical law is the same.

Note that SR is a theoretical formalism that applies to phenomena of different nature: new and more general (than the classical newtonian mechanics) kinematics and dynamics are introduced. Therefore, in the context of SR, an important inconsistency of classical physics (of which the magnet-conductor relative motion is a simple example, Equations (A.1) and (A.2)) appears: Newton's law is invariant under a galileian change of coordinates, Maxwell's equations are not.

Einstein had two key ideas:

1. Maxwell's equations are correct;
2. physic laws have the same form on every inertial reference frame.

This assumption is peculiar of SR, in the context of GR the case is generalized to non-inertial reference frames.

Einstein found that, to eliminate these asymmetric results of Maxwell Equations, a new concept of time was needed: time is *not* an absolute concept. Moreover, it is *not* uncorrelated to external phenomena (and this is a fundamental of newtonian mechanics).

On the contrary, time is intrinsically a relative quantity and, as Einstein remarked, it is always defined through two different simultaneous events (e. g. think about the two sentences "The train is passing at 7:00" and "The train is passing when the clock hand is pointing at 7:00", time is defined considering two different events, the train

passing and the clock hand pointing). It becomes then important to define the concept of simultaneity, which is again relative and done with the help of the second postulate of SR:

The speed of light c *in vacuum takes always the same value, in all the inertial reference frames independently on the motion of the source.*

The concept of simultaneity comes then by exploiting the speed of light staying constant, from the synchronisation of two hypothetical clocks embedded with two different reference frames (Einstein synchronisation process, Figure A.2), located in two different points in the space (1 and 2), distant L one another.

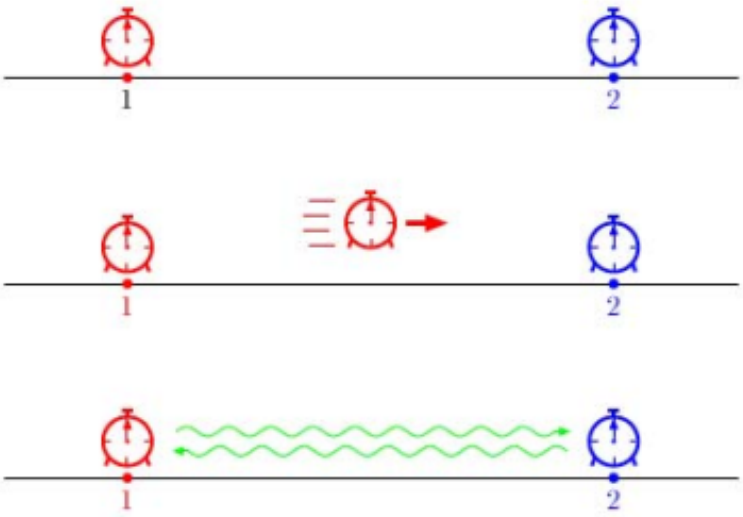

Figure A.2: If at time t a light signal is sent from the observer in 1 to 2, then the observer in 2 must set their clock to the time $t + \frac{L}{c}$ and re-send the signal back to 1. The observer in 1 should observe now the signal from 2 arriving at the time $t + 2\frac{L}{c}$. Source [4].

Before going deeper with the mathematical formulation, the definition of a reference quantity, the *proper time* $\Delta\tau$, is needed. Note that $\Delta\tau$ is a relativistic-invariant:

Relativistic-invariant means invariant with respect to the Lorentz transformations, treated in Section A.2.2.

The proper time $\Delta\tau$ *is the time measured on a clock in its reference frame at rest.*

A.2.2 *Lorentz transformations*

Lorentz transformations will be presented from two different points of view. The first one, more conceptual, follows what described in [4], whereas some simple tensor analysis will be presented following [35].

Let us consider two different reference frames, K and K′, in relative motion one another with velocity v, as in Figure A.3:

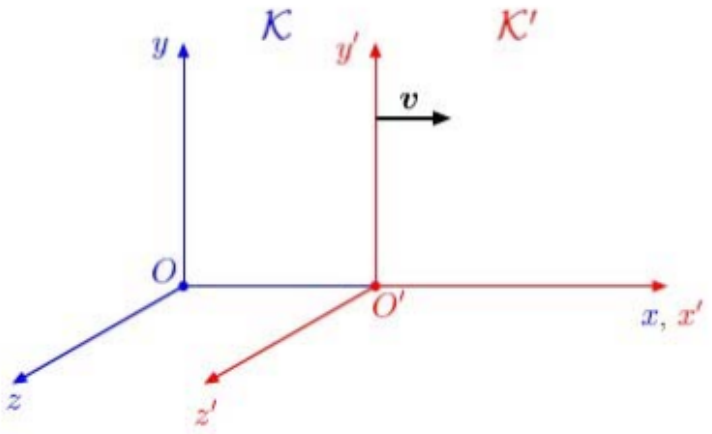

Figure A.3: Particularly, K′ is moving with velocity v along the x axis. Since the context of analysis is the one of SR, considering a motion along one axis only is not a loss of generality, since it must be rectilinear and uniform. If there were also other components, a rotation of the frame is enough to get back to this simple case. Source [4].

The galileian coordinate transformation is defined as:

$$x' = x + vt \quad , \quad t' = t \tag{A.3}$$

As already stated in Section A.2.1, a galileian coordinate transformation is based on the postulate of absolute time ($t = t'$), the same for both the frames K and K′.

A Lorentz coordinate transformation is instead defined as:

$$x' = \frac{x - vt}{\sqrt{1 - (v/c)^2}} \quad , \quad t' = \frac{t - vx/c^2}{\sqrt{1 - (v/c)^2}} \tag{A.4}$$

Lorentz transformations involve the second SR postulate only, the invariance of the speed of light c in vacuum. Some of observations can be made:

- the Lorentz Factor γ can be defined:

$$\gamma = \frac{1}{\sqrt{1 - (v/c)^2}} \tag{A.5}$$

  which basically identifies the difference between the Galileian and the Lorentz transformations;

- the speed of light is a limit velocity:

$$\text{if} \quad v \to c \quad \Longrightarrow \quad \gamma \to +\infty \tag{A.6}$$

  therefore a divergence (and thus the most significant differences with the classical physics) is experienced when $v \to c$;

- the relativistic law for the summation of velocities is:

$$V = \frac{v_1 + v_2}{1 + v_1 v_2 / c^2} \tag{A.7}$$

  one can easily observe that if $v_1 = c$ and $v_2 = c$ then $V = c$;

- galileian transformations are the limit of Lorentz transformations, for $c \to +\infty$.

Now several implications of Lorentz transformations can be found. Only three (the ones more intuitively related to the mechanics of the motion) will be reported in this section[1]:

1. Referring always to the two reference frames reported in Figure A.3, it is now provable that events which are simultaneous in K are not so in K′. Considering two different points A and B in K:

$$\begin{gathered} t_A = t_B \\ t'_A = \gamma\left(t - \frac{v}{c^2}x_A\right) \ , \ t'_B = \gamma\left(t - \frac{v}{c^2}x_B\right) \\ \implies \quad \Delta t' = t'_A - t'_B \neq 0 \end{gathered} \tag{A.8}$$

2. In the reference frame K′ time dilatation[2] is experienced. Consider two events happening in the same point in K′ ($x'_A = x'_B = x'$) and compute times and coordinates in K:

Time dilatation means that the time runs slower in K′ than in K, therefore $\Delta t' < \Delta t$.

$$\begin{gathered} t_A = \gamma\left(t'_A + \frac{v}{c^2}x'\right) \ , \ x_A = \gamma(x' + v t'_A) \\ t_B = \gamma\left(t'_B + \frac{v}{c^2}x'\right) \ , \ x_B = \gamma(x' + v t'_B) \\ \Delta t = t_B - t_A = \gamma(t'_B - t'_A) = \frac{\Delta t'}{\sqrt{1 - v^2/c^2}} \end{gathered} \tag{A.9}$$

3. Measuring the dimension of objects "attached" to K′ (moving with velocity v) in the frame K, length contraction is experienced in K. This happens because the length is actually measured as the distance between the two ends (1 and 2) of the object *at the same time instant in* K:

$$\begin{gathered} L' = x'_2 - x'_1 \qquad \text{length in the "attached" frame } K' \\ L = x_2 - x_1 = \frac{1}{\gamma}(x'_2 - x'_1) = \frac{1}{\gamma}L' \qquad \text{length in the frame } K \end{gathered} \tag{A.10}$$

1 To have a deeper insight on the topic the main reference is always [35].
2 Note that, due to the speed of light being a limit velocity, $0 \leqslant \gamma < 1$.

A.2.3 *Minkowski space*

The concept of space needs now to be extended. Physical phenomena happen in a four-dimensional continuum, called *space-time*. Time is now defined as any local quantity, therefore it is treated more or less like the other three spatial dimensions.

The elements of the space-time are events.

Let us write a generic vector $\mathbf{x}$ of a four-dimensional space of this kind with its component:

$$\mathbf{x} = (x, y, z, ct); \tag{A.11}$$

where c is the speed of light in vacuum, (x, y, z) the usual spatial coordinates and t is the actual time.

It can be observed that Lorentz transformations are *isometric transformations* among this kind of vector spaces:

$$\mathbf{x} = (x, y, z, ct) \xrightarrow{Lorentz} \mathbf{x}' = (x', y', z', ct') \tag{A.12}$$

Note that now also the time has changed ($t \neq t'$).

The concept of metric will be deepened in Section A.3.

Moreover, the metric of spaces of this kind can be written as:

$$g_{ij} = \begin{bmatrix} 1 & 0 & 0 & 0 \\ 0 & 1 & 0 & 0 \\ 0 & 0 & 1 & 0 \\ 0 & 0 & 0 & -1 \end{bmatrix} \tag{A.13}$$

All the vector spaces that feature this metric are called Minkowski spaces.

A.2.4 *Tensor formulation*

In the following section all the tensor expressions will follow Einstein's notation (implicit summation over the repeated indexes). The greek letters $\alpha, \beta, \gamma, \delta$ will represent the indexes in this subsection and all of them can vary among x, y, z, ct, according to what presented in Subsection A.2.3. Using tensor notation, Lorentz transformations from coordinate system $\mathbf{x}^\beta$ to coordinate system $\mathbf{x}^\alpha$ can be written as:

The two vectors under consideration are four-vectors, elements of a four-dimensional space-time

$$\mathbf{x}^\alpha = \Lambda^\alpha_\beta \mathbf{x}^\beta + \mathbf{a}^\alpha \tag{A.14}$$

where Λ^α_β and $\mathbf{a}^\alpha$ are constants, restricted by the following conditions:

$$\Lambda^\alpha_\gamma \Lambda^\beta_\delta \eta_{\alpha\beta} = \eta_{\gamma\delta}$$
$$\text{with} \qquad \eta_{\alpha\beta} = \begin{cases} +1 & \text{if } \alpha = \beta = x, y, z \\ -1 & \text{if } \alpha = \beta = ct \\ 0 & \text{if } \alpha \neq \beta \end{cases} \tag{A.15}$$

Note that, in tensor notation, upper and lower indexes distinguish the base of reference, canonical in the first and reciprocal in the latter. This property will be often used and expressed in the whole analysis. Further details, as well as all the tensor operations whose description is omitted here, can be found in [35].

One can already observe some similarities with the definition of metric given in Section A.2.3. The concept will be extended in Section A.3.

The tensor formulation becomes particularly useful when expressing metrics and transformations. A simple proof of this is the invariance of the proper time $\Delta\tau$ (following the steps reported in [35]). The definition is:

$$c^2\Delta\tau^2 = c^2\Delta t^2 - \Delta\mathbf{x}\cdot\Delta\mathbf{x} \tag{A.16}$$

This can be re-written using the tensor notation specified above:

$$\Delta\tau = -\eta_{\alpha\beta}\Delta x^\alpha \Delta x^\beta \tag{A.17}$$

Applying Lorentz's transformations to Δx^δ the correspondent element in the transformed reference frame is obtained:

$$\Delta x'^\alpha = \Lambda^\alpha_\delta \Delta x^\delta \tag{A.18}$$

So the proper time in the new frame will be:

$$\begin{aligned}\Delta\tau' &= -\eta_{\alpha\beta}\Delta x'^\alpha \Delta x'^\beta \\ &= -\eta_{\alpha\beta}\Lambda^\alpha_\gamma \Lambda^\beta_\delta \Delta x^\gamma \Delta x^\delta \\ &= -\eta_{\gamma\delta}\Delta x^\gamma \Delta x^\delta\end{aligned} \tag{A.19}$$

Therefore:

$$\Delta\tau'^2 = \Delta\tau^2 \tag{A.20}$$

A.3 CURVED GEOMETRY

The discussion reported in this section will refer mainly, about notation and formalism, to what presented in [34]. This section is meant to provide the reader of the key concepts only about generalised geometries[3], for what is necessary to have a conceptual but mathematically solid understanding of it, to be then able to face GR.

Tensor notation will be used, represented by the indexes i, j, k, l, m; all of them to vary over all the general n-dimensions of the space, unless differently specified in each particular case.

3 A deeper insight can be found in both [34] and [35], this section is a summary of what presented there.

A.3.1 *Metric*

First of all, generalised n-dimensional space will be considered, with a set of n coordinates q^i describing the position of a generic point in this space. Let us introduce now a basis $\mathbf{e}_i$ for this space. The position $\mathbf{q}$ of the point can therefore be written as:

$$\mathbf{q} = \mathbf{e}_i q^i \tag{A.21}$$

Note that any assumption about this space and coordinate system is yet to be made. The formulation will be then kept general, without assuming rectilinear basis vectors and the space to be flat.

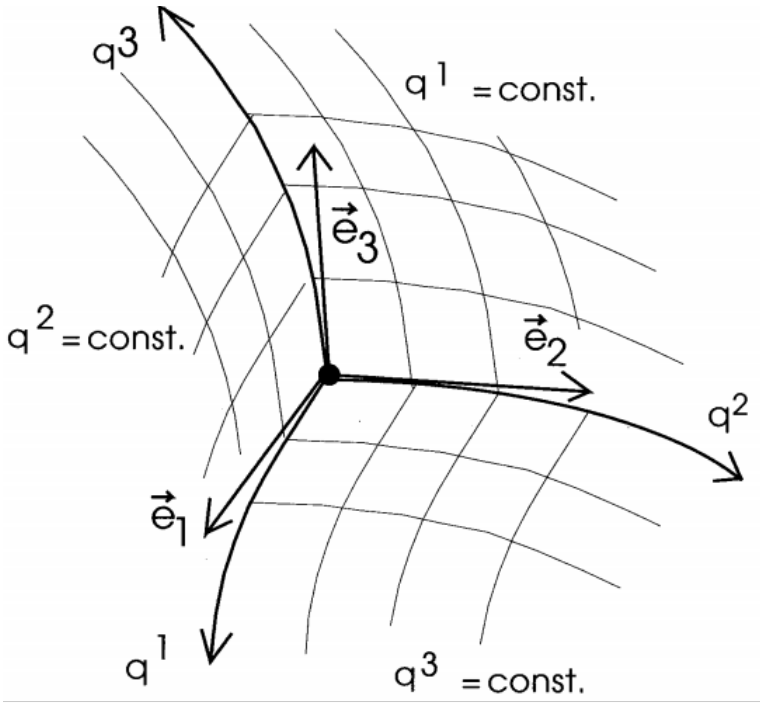

Figure A.4: The tangent space has rectilinear basis vectors and, therefore, quantities. This concept can be generalized to n-dimensional curved spaces, 3-d spaces are useful for visual interpretations. Source [34].

The only assumption required and to be made right now is the existence and uniqueness of a rectilinear tangent space (note that the problem is n-dimensional), at any point of the space. An example, for a 3-dimensional curved space, can be seen in Figure A.4. This assumption becomes particularly useful when the definition of infinitesimal quantities is needed, such as the *line element* ds[4]. It can be defined

4 Note that the *line element* corresponds to the exact "physical" displacement in the tangent space.

in the tangent space, and its definition is exact to the first order for quantities $dq^i \to 0$:

$$d\mathbf{s} = \mathbf{e}_i dq^i \tag{A.22}$$

A new quantity is now introduced, the *interval*, defined as the square of the distance of the displacement. The infinitesimal interval in the tangent space, from simple vector algebra, is:

$$(d\mathbf{s})^2 = \left(\mathbf{e}_i \cdot \mathbf{e}_j\right) dq^i dq^j \tag{A.23}$$

It is now possible to define the *metric matrix* g_{ij} in terms of the inner product of the basis vectors:

$$g_{ij} = \mathbf{e}_i \cdot \mathbf{e}_j \tag{A.24}$$

Some observations can be made:

- The metric matrix is symmetric by definition;
- In the case of generalized coordinates, the metric matrix, as well as the basis vectors, can be non-constant, but position-dependent ($g_{ij} = g_{ij}(\mathbf{q})$ and $\mathbf{e}_i = \mathbf{e}_i(\mathbf{q})$);
- Taking a look to Equation (A.13), the metric rules the dot product in the space of definition[5];

Moreover, following what presented in [34] about reciprocal basis analysis, it can be proved that the metric matrix also lowers (or rises, depending on the basis of definition) the indexes:

$$\begin{gathered} dq_i = g_{ij} dq^j \\ \text{or} \\ dq^i = g^{ij} dq_j \end{gathered} \tag{A.25}$$

And also, due to the definition of reciprocal basis itself, g_{ij} and g^{ij} are one the inverse of the other:

$$g_{ij} = \left(g^{ij}\right)^{-1} \tag{A.26}$$

A.3.2 *Affine connection*

How do the basis vectors change between two points of a generalized curved space? The *affine connection* is the mathematical entity that answers to this question. Remaining position-dependent, one can write the following relation (from [34]), under the assumption of infinitesimal displacements (therefore infinitesimal changes on the basis vectors) and expanding up to the first order in the original point:

$$d\mathbf{e}_i(\mathbf{q}) = \gamma^k_{ij}(\mathbf{q}) \mathbf{e}_k(\mathbf{q}) dq^j \tag{A.27}$$

5 The one reported in Equation (A.13) was the particular metric matrix of a Minkowski Space.

where $\gamma_{ij}^{k}(\mathbf{q})$ are a position-dependent set of coefficients. In the reference [34] it is proved that those coefficients correspond to $\Gamma_{ij}^{k}(\mathbf{q})$, the affine connection.

With some differential calculations and other manipulations, it is possible to obtain the following expression for $\Gamma_{ij}^{k}(\mathbf{q})$:

$$\Gamma_{ij}^{k}(\mathbf{q}) = \frac{1}{2} g^{km}(\mathbf{q}) \left[\frac{\partial g_{mi}(\mathbf{q})}{\partial q^{j}} + \frac{\partial g_{mj}(\mathbf{q})}{\partial q^{i}} - \frac{\partial g_{ij}(\mathbf{q})}{\partial q^{m}} \right] \tag{A.28}$$

In summary, the affine connection is the law with which the basis vectors change in a curved n-dimensional space.

A.3.3 *Lagrange equations and geodesics*

When the definition of time changes, energetic approaches become the only way to derive equations of motion. A generalized expression for Lagrange equations is needed, since it is no longer possible to use 3^{rd} Newton's law to obtain the equations of motion. But before doing this, it is crucial to define a new velocity concept.

The action-reaction law can be defined only as a simultaneous force exchange. But in the context of relativity, time is different for the two bodies involved, therefore it becomes tricky to define at what time instant (different in the two body-attached reference frames) the force exchange is happening.

The analysis is now restricted to a 4-dimensional space, similar to the Minkowski space characterizing SR, but with the possible presence of curvature (thus with the dependence on the position $\mathbf{q}$)[6].

The concept of proper time can be exploited to write the line element of this case:

$$(d\mathbf{s})^2 = -c^2(d\tau)^2 = (d\mathbf{q})^2 - c^2(dt)^2 = (v^2 - c^2)(dt)^2 < 0 \tag{A.29}$$

Using metric and proper time definitions:

$$\frac{d\mathbf{s}}{d\tau} \cdot \frac{d\mathbf{s}}{d\tau} = g_{ij}(\mathbf{q}) \frac{dq^{i}}{d\tau} \frac{dq^{j}}{d\tau} = -c^2 \tag{A.30}$$

A new quantity can now be introduced, the *four-velocity* $\mathbf{u}$. Its general component is:

$$u^{i} = \frac{dq^{i}}{d\tau} \tag{A.31}$$

From now until the end of Subsection A.3.3, the case of a particle of mass m freely moving in this four-space is being considered. The kinetic energy T of the particle can be then written according to the definition of $\mathbf{u}$:

$$T = \frac{1}{2} m\mathbf{u} \cdot \mathbf{u} = \frac{1}{2} m g_{ij}(\mathbf{q}) \frac{dq^{i}}{d\tau} \frac{dq^{j}}{d\tau} \tag{A.32}$$

Note that, in this case, the sole kinetic energy corresponds to the whole Lagrangian function.

Lagrange equations with these coordinates can be written as:

$$\frac{d}{d\tau} \left(\frac{\partial T}{\partial (dq^{i}/d\tau)} \right) - \frac{\partial T}{\partial q^{i}} = 0 \tag{A.33}$$

6 An element of this curved space is $\mathbf{q} = (q^1, q^2, q^3, ct)$

Writing the expression of T and after a small manipulation, Lagrange equations become:

$$\frac{d}{d\tau}\left(m g_{ij}(\mathbf{q})\frac{dq^j}{d\tau}\right) - \frac{1}{2}m\frac{\partial g_{jk}}{\partial q^i}\frac{dq^j}{d\tau}\frac{dq^k}{d\tau} = 0 \tag{A.34}$$

Note that the equation, and therefore the dynamics, is not dependent on the mass any longer, it has become a general (not related to the particular case of single point mass freely moving in the space) fact of pure geometry. This particular aspect will be better discussed in Chapter B.

It is indeed one of the peculiar results of GR.

Exploiting some properties of the definition of reciprocal basis and manipulating this form of Lagrange equations, it is possible to highlight the role of the affine connection $\Gamma^k_{ij}(\mathbf{q})$ (defined in equation (A.28)), on Lagrange equations ([34]):

$$\frac{d^2q^k}{d\tau^2} + \Gamma^k_{ij}(\mathbf{q})\frac{dq^i}{d\tau}\frac{dq^j}{d\tau} = 0 \tag{A.35}$$

It is worth to mention a particular class of solutions of these geometry problems, the *geodesics*. Geodesics are the minimum length trajectories, in a generalized space. They are obtained by solving the equations of motion, with the constraint to follow this minimized path[7]:

In an Euclidean space geodesics are straight lines, in a curved space they are not. Think about stretching a rope constrained to lie in a curved surface: that is a geodesic for that curved space(example reported in [34]).

$$s_{12} = \int_1^2 c\,d\bar{\tau} \tag{A.36}$$

It follows that, since c is constant by principle, the minimisation has to occur on the proper time τ, finding then the path that passes through the points satisfying this condition. The concept of geodesics will be of great value in Chapter B.

A.3.4 *Geometric tensors*

In this section the mathematical definitions of some relevant tensors are reported, as well as their main properties and how they are obtained, following what presented in [34]. Other details of the same are also available in [35].

First of all, two already presented entities are tensors indeed, the metric matrix and the affine connection:

- metric matrix - $g_{ij}(\mathbf{q})$ is a 2^{nd} order tensor, linear by definition (it comes from the inner product of the basis vectors $\mathbf{e}_i(\mathbf{q})$, Equation (A.24));
- affine connection - $\Gamma^k_{ij}(\mathbf{q})$ (defined in Equation (A.28)) is a 3^{rd} order tensor, dependent only of the metric and its derivatives, it is however nonlinear on the same;

7 Note that, since the coordinates change in space, the same does the proper time τ. In the context of SR the whole space was a Minkowski space, Section A.2.3, in a more generalized case the dependence on the position modifies also the the proper time.

Some other tensor entities are now introduced, defined as functions of $g_{ij}(\mathbf{q})$ and $\Gamma^k_{ij}(\mathbf{q})$.

The first one is the *Riemann curvature tensor* $R^i_{jlk}(\mathbf{q})$:

$$R^i_{jlk}(\mathbf{q}) = \left(\frac{\partial}{\partial q^l}\Gamma^i_{jk}(\mathbf{q}) + \Gamma^i_{lm}(\mathbf{q})\Gamma^m_{jk}(\mathbf{q})\right) - \left(\frac{\partial}{\partial q^k}\Gamma^i_{jl}(\mathbf{q}) + \Gamma^i_{km}(\mathbf{q})\Gamma^m_{jl}(\mathbf{q})\right) \tag{A.37}$$

with properties:

- position-dependent;
- 4^{th} order tensor;
- 2^{nd} order, nonlinear form of the metric;
- It describes the internal structure of the n-dimensional space dependent of the metric only;
- It is skew-symmetric in the single swaps of the couples (i,j) and (l,k):

$$R^i_{jlk}(\mathbf{q}) = -R^j_{ilk}(\mathbf{q}) \quad \text{and} \quad R^i_{jlk}(\mathbf{q}) = -R^i_{jkl}(\mathbf{q}) \tag{A.38}$$

This is a 4^{th} order tensor, the definition of symmetry has to be thought as just related to a general index swap. It is not "visual" as the symmetry definition for matrices is.

- Therefore, it is symmetric on both those swaps occurring together:

$$R^i_{jlk}(\mathbf{q}) = R^j_{ikl}(\mathbf{q}) \tag{A.39}$$

The second one is the *Ricci Tensor* $R_{ij}(\mathbf{q})$. Its derivation is straight forward and simply related to *Riemann Curvature Tensor* through a tensor contraction:

$$R_{ij}(\mathbf{q}) = R^k_{ikj}(\mathbf{q}) \tag{A.40}$$

The definition of this tensor is a simple but necessary step towards the derivation of *Einstein tensor*. However, it is also useful to define the *scalar curvature* $R(\mathbf{q})$, again through a tensor contraction:

$$R(\mathbf{q}) = R^i_i(\mathbf{q}) \tag{A.41}$$

Note that the operations of rising or lowering the indexes consists simply of a change in the basis of expression, from the initial to the reciprocal one, for the raised/lowered index.

Finally, *Einstein Tensor* $G_{ij}(\mathbf{q})$ can be defined:

$$G_{ij}(\mathbf{q}) = R_{ij}(\mathbf{q}) - \frac{1}{2}g_{ij}(\mathbf{q})R(\mathbf{q}) \tag{A.42}$$

It can be proved that, as reported in [34]:

The metric matrix $g_{ij}(\boldsymbol{q})$ is symmetric because of the definition of inner product.

- R_{ij} is symmetric, therefore G_{ij} is symmetric too;

- G_{ij} is *divergenceless*, meaning that its covariant divergence vanishes[8].

A.4 RIEMANNIAN GEOMETRY

Wrapping up, now all the conceptual and mathematical tools to tackle broadly GR have been defined. In this and last step (Section A.3) the biggest effort has been made, generalizing the common concept of euclidean geometry to the absolutely general and free of assumptions of riemannian Geometry. The next step is to extend the context of SR to GR, to be developed in Chapter B, to finally obtain a formulation of the relativistic N-body problem.

8 Deeper details about co-variant differentiation can be found in the reference papers. They are not reported here because they are not of high meaning for the goals of this thesis.

B

GENERAL RELATIVITY FEATURES AND EQUATIONS

B.1 INTRODUCTION

In this chapter the milestones to obtain the equations of the relativistic N-body Problem will be presented, making use of all the mathematical and conceptual tools developed in Chapter A. The main reference remains always [35], with the help of [34] to present the points in a more conceptual point of view. In the last section of the chapter (Section B.4) the main reference will be changed to [36], with the purpose of going deeper in what is specific of *post-newtonian celestial mechanics*. All the indexes (i, j, k, l) that will be used are intended to be, unless differently specified, varying among $(1, 2, 3, 4)$, the four dimensions featuring GR.

B.2 PRINCIPLES, EQUATIONS AND QUALITATIVE CONSEQUENCES

GR is a theory of principles. Those are reported in the following list, according to the way Einstein first formulated the theory (from [34]):

1. We live in a four-dimensional, curved, riemannian space.
2. The structure of this space is given by Einstein's field equations.
3. Particles move along geodesics in this space.

Each of these points will be tackled in the next subsections, building the frame to study and understand their consequences and applications.

B.2.1 *Equivalence principle*

Before going deeper into those concepts, it is crucial to understand another key principle that Einstein stated first, the so called *Equivalence Principle*:

Gravitational and inertial mass are exactly the same thing.

Einstein proved it with the following simple conceptual proof, whose consequences are however fundamental for the rest of the theory [34]:

Consider a particle, undergoing the gravitational acceleration $\boldsymbol{g}$, being inside a closed room. Imagine the same particle being in a closed room in a space without any gravitational field, which room is moving with acceleration $-\boldsymbol{g}$[1]. The particle itself is not able to feel the difference between the gravitational field and the acceleration of the room.

This means that there is actually no difference between gravity and acceleration. Therefore, this implies the equivalence of defining the mass through inertia and gravity. This allows to cancel the mass on both sides of the gravitational equation of motion (e. g. Equation (A.34)), reducing the problem to one of pure and simple geometry.

B.2.2 *Curved, riemannian space*

All the geometric considerations done in Section A.3 come together here, in this concept. Particularly, and this is exactly the characterisation of riemannian space (presented in Section A.4), the space is described by the set of generalised coordinates q_i and the generalised basis vectors $\mathbf{e}_i(\mathbf{q})$. The line element then becomes:

$$d\mathbf{s} = \mathbf{e}_i(\mathbf{q})dq^i \tag{B.1}$$

And the physical interval can be expressed in terms of the metric g_{ij} (defined in the same way as in Equation (A.24)):

$$(d\mathbf{s})^2 = g_{ij}dq^i dq^j \tag{B.2}$$

At each point of this space there exists a flat tangent Minkowski space with a Lorentz metric $g_{ij}^{tangent}$ (the same described in Equation (A.13)) in a cartesian basis equal to:

$$g_{ij}^{tangent} = \begin{bmatrix} 1 & 0 & 0 & 0 \\ 0 & 1 & 0 & 0 \\ 0 & 0 & 1 & 0 \\ 0 & 0 & 0 & -1 \end{bmatrix} \tag{B.3}$$

In this flat tangent space, it is possible to define another cartesian space, the so called *local freely falling frame* LF[3]. This space is characterised by being subjected to the acceleration (freely falling) given by the gravitational field. As a consequence, the local effects of the gravitational field are exactly canceled by inertial forces; what is left

1 This particular will be discussed in Subsection B.2.2, it is exactly the definition of *Local Freely Falling Frame*.

are then just the Lorentz's metric (exactly the same of the local tangent space) and the laws of SR[2]. This space can become useful when it comes to provide some physical interpretations to GR, or to specialise any description in a reference frame embedded with a particular body moving in a gravitational field.

B.2.3 *Einstein's field equations*

Saying that the structure of the space is provided by the solution of Einstein's field equations means that they will lead to the definition of the metric. Those equations are indeed (from [34]):

From now on, the dependence on the position $\boldsymbol{q}$, unless otherwise specified, will be assumed as implicit and always present, without writing it explicitly.

$$G_{ij} = kT_{ij} \tag{B.4}$$

Where:

- T_{ij} is the *energy-momentum tensor*, whose elements account for all the energy, mass and momentum sources in the space;
- k is a constant, the *strength* of the gravitational field, to be determined;
- G_{ij} is the *Einstein Tensor* (nonlinear differential form in the *Metric*) of the current generalized space.

Note that G_{ij} has already been defined in Equation (A.42) as function of the Ricci tensor R_{ij} which, similarly, has been defined as function of the Riemann curvature tensor R^i_{jlk} (Equation (A.40)). This last tensor, through its definition (Equation (A.37)), comes from the affine connection Γ^i_{jk} and finally, using Equation (A.28), this is in turn defined as function of the metric g_{ij}. One can already feel the mathematical path that rules this principle of GR, if it were possible to have an analytical solution of all these equations then a simple backward process would be enough to fully characterise the structure (metric and curvature) of the space.

Note also that G_{ij} is proportional to T_{ij} through k. Intuitively, one can already say that a strong set of forces (of any nature) influences a lot the geometry of the space. Particularly talking about a gravitational field, being it stronger close to the massive body, it produces an higher curvature of the space nearby the massive body itself.

B.2.4 *Geodesic motion*

It is in this matter that the equivalence principle plays its most important role, reducing the dynamics problem into a purely geometrical one.

2 This definition is only local, therefore it holds in an infinitesimal portion of space only. There cannot be cancellation of gravitational effects due to inertia in an extensive sense, plus one should note also that, keeping it general, the gravitational field is different in all the points of the space.

Taking a look again at the equations of motion of a particle of mass m (Equation (A.34)), that mass m should be called m_i (inertial mass). By adding a gravitational force (right hand side of the equation, as a simple term proportional to the gravitational mass m_g), it is clearly possible to see that the equivalence principle is the key to reach the pure geometry problem, where there is no mass dependence indeed.

The motion is then said to happen particularly along geodesics because of the definition of the space itself. Any kind of force or energy in the context of GR goes into the energy-momentum tensor T_{ij}, which is then linked to the Einstein tensor G_{ij} and so on, dictating finally the metric, thus the geometry, of the space.

B.2.5 *Newtonian limit*

GR is an extension of classical physics. It should be therefore possible to re-obtain newtonian mechanics laws just by applying some assumptions to the equations of GR. The necessary steps will be covered in this subsection, following what presented in [34].

It should be clear at this point that the presence of gravity, and so of any mass, is a source of curvature, with the most significant curvatures to exist nearby the source itself. A first assumption is then made, which is for a point to be located at far enough from all the curvature sources: here the space can be approximated as almost flat. Getting also back to the set of coordinates introduced in Section A.2, when talking about SR:

$$\mathbf{x} = (x_1, x_2, x_3, ct) = (q_1, q_2, q_3, q_4) \tag{B.5}$$

Since the space is almost flat, the metric g_{ij} at the point $\mathbf{x}$ can be defined as a slight modification of a Lorentz's Metric g^0_{ij}:

$$g_{ij}(\mathbf{x}) = g^0_{ij} + \gamma_{ij}(\mathbf{x}) \tag{B.6}$$

with $\|\gamma_{ij}(\mathbf{x})\| << 1$[3]. A static dependence only is assumed, with $\gamma_{ij}(\mathbf{x})$ depending only on the position $\mathbf{x}$ and not on the velocity of the sources, or of any other particle moving nearby there.

The relation between time and proper time can be re-written, manipulating Equation (A.23) with Equation (B.6) to obtain:

$$\left(\frac{ds}{dct}\right)^2 = -\left(\frac{d\tau}{dt}\right)^2 = \left[g^0_{ij} + \gamma_{ij}(\mathbf{x})\right]\frac{dx^i}{dct}\frac{dx^j}{dct} \tag{B.7}$$

The newtonian limit can now be introduced: since the speed of light is constant wherever in space (no matter the curvature), if the velocities are small enough it can be assumed that $c \to \infty$. This implies that Equation (B.7), at the newtonian limit, can be expressed as function of

3 Note that, for the purposes of this analysis, any kind of norm can be considered in this assumption.

the time coordinate (coordinate 4) only and, exploiting the definition of Lorentz metric, further manipulated with a first order power series expansion to obtain:

$$\frac{d\tau}{dt} \approx \left[1 - \gamma_{44}(\mathbf{x})\right]^{1/2} \approx 1 - \frac{1}{2}\gamma_{44}(\mathbf{x}) \tag{B.8}$$

because of $\gamma_{44}(\mathbf{x})$ being small.

Note that by proving $\gamma_{44}(\mathbf{x} = O(1/c^2))$ the time t would be proven to be indistinguishable from the proper time τ, therefore newtonian mechanics and GR would be linked.

The dependence on the position $\mathbf{x}$ has vanished as a consequence of the newtonian limit.

Some of the key concepts of newtonian mechanics are now introduced, by considering the gravitational field provided by a single mass M:

$$\begin{aligned} \phi &= -\frac{MG}{r} && \text{Gravitational Potential} \\ \mathbf{g} &= \vec{\nabla}\phi && \text{Gravitational Field} \\ m_i \frac{d^2\mathbf{x}}{dt^2} &= -m_g \vec{\nabla}\phi && \text{Particle motion} \end{aligned} \tag{B.9}$$

With G being Newton's constant and r the distance of the particle m from the source.

The two masses m_i (inertial) and m_g (gravitational) are equal because of the equivalence principle. They can then be simplified to obtain:

$$\frac{d^2\mathbf{x}}{dt^2} = -\vec{\nabla}\phi \tag{B.10}$$

Yet again, the orbit has become a function of the source and the geometry only.

The strength (from [34]) of the gravitational field can be characterised by the non-dimensional ratio $2\phi/c^2$, with $2\phi/c^2 \to 0$ at the newtonian limit.

Getting back to GR, from the 3rd principle (presented at the beginning of Section B.1) the particle m should move along geodesics in the space, which, in the coordinate system introduced in Equation (B.5), are defined as:

$$\frac{d^2x^i}{d\tau^2} + \Gamma^i_{jk}\frac{dx^j}{d\tau}\frac{dx^k}{d\tau} = 0 \tag{B.11}$$

In the newtonian limit the only relevant part of the second contribution is the one in the coordinate $x^4 = ct$:

$$\frac{d^2x^i}{d\tau^2} + \Gamma^i_{44}c^2 \approx 0 \tag{B.12}$$

The affine connection Γ^i_{44} is connected, by its definition (Equation (A.28)), to the metric g_{ij} introduced in Equation (B.6). This definition

can be exploited together with $\gamma_{ij}(\mathbf{x})$ being not dependent on time to obtain:

$$\Gamma^i_{44} = -\frac{1}{2}\frac{\partial}{\partial x^i}\gamma_{44}(\mathbf{x}) = -\frac{1}{2}\vec{\nabla}\gamma_{44}(\mathbf{x}) \qquad \text{for } i = 1,2,3$$
$$\text{and} \tag{B.13}$$
$$\Gamma^4_{44} = 0$$

Therefore the geodesics equation becomes:

$$\frac{d^2x^i}{d\tau^2} = \vec{\nabla}\left[\frac{c^2}{2}\gamma_{44}(\mathbf{x})\right] \qquad \text{for } i = 1,2,3 \tag{B.14}$$

Note that now Equations (B.10) and (B.14) (thus GR and newtonian mechanics) can be connected simply by imposing:

$$\gamma_{44}(\mathbf{x}) = \frac{2\phi}{c^2} \tag{B.15}$$

The assumption of being far from the source ($r \to \infty$) allows us to say $2\phi/c^2 \to 0$, thus the metric is almost flat indeed.

GR and newtonian mechanics have successfully been connected, under the simple assumptions (almost flat, static metric and newtonian limit) made throughout the proof. One could however argue on the imposition stated in Equation (B.15), claiming this situation to be just a particular case. This last doubt will be solved in Sections B.3 and B.4 for two different cases, where, respectively, the final expression of the lagrangian L and the equation of motion itself will be obtained in a more rigorous way.

B.3 SCHWARZSCHILD'S SOLUTION

The first, simple but meaningful gravitational field that can be analysed is the one produced by a single, spherically symmetric, non-rotating source, which an analytical solution is eventually available for. This section will follow what presented on [35], providing the key results and consequences of this particular case, called *Schwarzschild's solution*.

B.3.1 *Field solution*

This kind of field source allows to operate directly some assumptions on the metric, without the need to define the energy-momentum tensor T_{ij} and solve Einstein's field Equations, leading to a static, isotropic metric to be diagonal if expressed in a reference frame centered at the source M, with spherical coordinates (r, θ, φ, t). In tensor notation it is defined as:

$$\begin{aligned} g_{rr} &= A(r); \\ g_{\theta\theta} &= r^2 \\ g_{\varphi\varphi} &= r^2 \sin^2\theta \\ g_{tt} &= -B(r) \end{aligned} \tag{B.16}$$

As it can be seen from Equation (B.16), static, isotropic means quasi-Lorentzian metric, where also one has that the proper time τ does not depend on the time t. The spherical symmetry is guaranteed by the definitions of $g_{\theta\theta}$ and $g_{\varphi\varphi}$. The terms $A(r)$ and $B(r)$ are to be determined by solving the field equations (Equation (B.4)).

The affine connection can be computed using Equation (A.28), to obtain the following non-vanishing terms:

$$\begin{aligned}
\Gamma^r_{rr} &= \frac{1}{2A(r)}\frac{dA(r)}{dr} & \Gamma^r_{\theta\theta} &= -\frac{r}{A(r)} \\
\Gamma^r_{\varphi\varphi} &= -\frac{r\sin^2\theta}{A(r)} & \Gamma^r_{tt} &= \frac{1}{2A(r)}\frac{dB(r)}{dr} \\
\Gamma^\theta_{r\theta} &= \Gamma^\theta_{\theta r} = \frac{1}{r} & \Gamma^\theta_{\varphi\varphi} &= -\sin\theta\cos\theta \\
\Gamma^\varphi_{r\varphi} &= \Gamma^\varphi_{\varphi r} = \frac{1}{r} & \Gamma^\varphi_{\varphi\theta} &= \Gamma^\varphi_{\theta\varphi} = \cot\theta \\
\Gamma^t_{tr} &= \Gamma^t_{rt} = \frac{1}{2B(r)}\frac{dB(r)}{dr}
\end{aligned} \tag{B.17}$$

Without passing through the Riemann curvature tensor, the Ricci tensor can be directy linked to the affine connection through

$$R_{ij} = \frac{\partial\Gamma^k_{ik}}{\partial x^j} - \frac{\partial\Gamma^k_{ij}}{\partial x^k} + \Gamma^l_{ik}\Gamma^k_{jl} - \Gamma^l_{ij}\Gamma^k_{kl} \tag{B.18}$$

Using Equation (B.18) R_{ij} becomes:

$$\begin{aligned}
R_{rr} &= \frac{B''(r)}{2B(r)} - \frac{1}{4}\left(\frac{B'(r)}{B(r)}\right)\left(\frac{A'(r)}{A(r)} + \frac{B'(r)}{B(r)}\right) - \frac{1}{r}\left(\frac{A'(r)}{A(r)}\right) \\
R_{\theta\theta} &= -1 + \frac{r}{2A(r)}\left(-\frac{A'(r)}{A(r)} + \frac{B'(r)}{B(r)}\right) + \frac{1}{A(r)} \\
R_{\varphi\varphi} &= \sin^2\theta R_{\theta\theta} \\
R_{tt} &= -\frac{B''(r)}{2A(r)} + \frac{1}{4}\left(\frac{B'(r)}{A(r)}\right)\left(\frac{A'(r)}{A(r)} + \frac{B'(r)}{B(r)}\right) - \frac{1}{r}\left(\frac{B'(r)}{A(r)}\right) \\
R_{ij} &= 0 \qquad \text{for } i \neq j
\end{aligned} \tag{B.19}$$

Where the notation C' means differentiation of the quantity C with respect to r, as also reported in [35]. Note that the symmetry of R_{ij} is a direct consequence of the metric and the set of coordinates chosen (according to the physics of the problem).

One can also observe that, being still made of differential equations, boundary conditions are actually needed. This case can be seen as a specific particular solution, where the homogeneous case is represented by the empty space, where obviously

$$R_{ij} = 0 \tag{B.20}$$

It can be noted that

$$\frac{R_{rr}}{A(r)} + \frac{R_{tt}}{B(r)} = -\frac{1}{rA(r)}\left(\frac{A'(r)}{A(r)} + \frac{B'(r)}{B(r)}\right) \tag{B.21}$$

Therefore, imposing the condition as in Equation (B.20) for R_{rr} and R_{tt}, what expressed into Equation (B.21) turns into a requirement on $A(r)$ and $B(r)$, which can be expressed as

$$\begin{gathered} \frac{B'(r)}{B(r)} = -\frac{A'(r)}{A(r)} \\ \text{or} \\ A(r)B(r) = constant \end{gathered} \tag{B.22}$$

One should not forget that, even for empty spaces, $A(r)$ and $B(r)$ have been defined as referred to the metric of the space which includes a source. The same assumption made in Section B.2.5 of flat space for $r \to \infty$ can be applied:

This means that the space must become Minkowskian for $r \to \infty$.

$$\lim_{r\to\infty} A(r) = \lim_{r\to\infty} B(r) = 1 \tag{B.23}$$

Therefore using Equation (B.23)the condition in Equation (B.22) becomes:

$$A(r) = \frac{1}{B(r)} \tag{B.24}$$

The only condition left to be used is the definition of R_{ij}, setting all the elements equal to 0. Plugging the result obtained in Equation (B.24) into their definitions in Equation (B.19) we obtain[4]:

$$\begin{aligned} R_{\theta\theta} &= -1 + B'(r)r + B(r) \\ R_{rr} &= \frac{B''(r)}{2B(r)} + \frac{B'(r)}{rB(r)} = \frac{R'_{\theta\theta}}{2rB(r)} \end{aligned} \tag{B.25}$$

It is then enough to set $R_{\theta\theta}$ equal to zero, to obtain

$$\frac{d}{dr}(rB(r)) = rB'(r) + B(r) = 1 \tag{B.26}$$

With solution (from [35]):

$$rB(r) = r + constant \tag{B.27}$$

The constant of integration can be found by again making use of the metric becoming Minkowskian for $r \to \infty$, particularly

$$g_{tt} = -B(r) \xrightarrow[r\to\infty]{} -1 - \frac{2\phi}{c^2} \tag{B.28}$$

as a consequence of what presented in Subsection B.2.5, with the same definition for ϕ (reported in Equation (B.9)). The constant of integration is therefore equal to $-2MG/c^2$, leading to the following definitions for $A(r)$ and $B(r)$:

$$\begin{aligned} A(r) &= \left[1 - \frac{2MG}{c^2 r}\right]^{-1} \\ B(r) &= \left[1 - \frac{2MG}{c^2 r}\right] \end{aligned} \tag{B.29}$$

4 Note that it is enough to study the condition in these two elements, the others are easily obtained from these two with Equations (B.19) and (B.21).

and the metric of the space with this source of mass M at its center is

$$g_{ij}(r,\theta,\varphi,t) = \begin{bmatrix} \left[1-\frac{2MG}{c^2 r}\right]^{-1} & 0 & 0 & 0 \\ 0 & r^2 & 0 & 0 \\ 0 & 0 & r^2\sin^2\theta & 0 \\ 0 & 0 & 0 & -\left[1-\frac{2MG}{c^2 r}\right] \end{bmatrix} \tag{B.30}$$

found by Karl Schwarzschild in 1916.

B.3.2 *Observations*

This subsection will present the observations and considerations available in [34] about the Schwarzschild's solution.

An interesting quantity can be highlighted, the Schwarzschild radius R_s:

$$R_s = \frac{2MG}{c^2} \tag{B.31}$$

For values $r < R_s$ g_{ij} becomes singular[5], with the result that as currently formulated there does not exist a solution for $r < R_s$. This is actually the lower limit of r domain.

Another interesting observation can help to understand the concept of curvature: at a fixed time instant t and for $\theta = \pi/2$, the space become a 3-dimensional surface, identified as z in Figure B.1. If one lived into this kind of space, their existence would be constrained to that surface. This is an extremely visual result and it can give a "classical" physical interpretation to the space-time curvature. Note that by existing in that space one would not feel the curvature, because constrained inside the curved reference frame. These effects can be observed only by being on an inertial and external reference frame, like if the world under study were enclosed in a fixed and inertial laboratory room.

B.3.3 *Classical tests of general relativity*

In this subsection a list of the classical tests of general relativity is presented. It is provided within this Section (B.3) because these are in their most significant effect (the variations due to the other bodies of the Solar System are small) due to the gravitational field of the Sun, which can be accurately modelled with the Schwarzschild's solution.

- *Gravitational redshift*

5 This is, intuitively because the reality is more complex, the key that makes the Black Holes black. They are so massive that R_s is big enough to include the whole body (for Earth $R_s \propto 10^{-3}$m), therefore nearby these objects the high curvature of the space forces the light to follow a curved and closed path, keeping it trapped in the field (this is why they are black, the light cannot literally abandon the field).

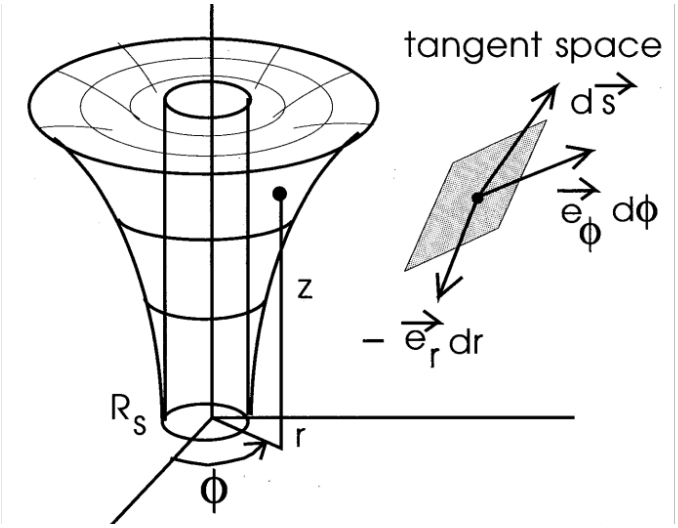

Figure B.1: Image from [34]. The concept of curvature turns now in dilatation and contraction of the space. Particularly, for increasing values of r and the same angle $\Delta\varphi$ the length of the arc in the inertial, fixed laboratory frame $\Delta s = r\Delta\varphi$ increases as well.

Practically speaking, the name of this effect calls to something happening to the light signals, observed shifted towards lower frequency values nearby the source[6]. This phenomenon is indeed observed because of the time dilatation produced by the gravitational field, which can actually be quantified as:

$$dt_{near} = \frac{dt_{far}}{\sqrt{1 - R_s/r}} \tag{B.32}$$

The expression looks similar in the shape to what already mentioned for SR in Section A.2. Note that the gravitational field is introduced here with its Schwarzschild radius R_s and the dilatation becomes stronger for $r \to R_s^+$ (i. e. the time runs slower close to the source.)

- *Deflection of light*

  This is the pure consequence of the space being curved by the source. Photons are massless particles, therefore they do not modify the field[7] and travel purely on the geodesics of the space curved by the sources. As a consequence, the position of some stars is observed to be slightly different than expected, not because it actually is, but because the relative position Earth-Sun-star makes the photons travel close to the Sun in some periods of the year, with the consequence of them being slghtly deflected and, looking at that star from Earth, resulting in a change of the apparent position of that particular star.

6 Red because of the visible spectrum, UV at high and IR at low frequencies.

7 Any massive body contributes to the whole gravitational field, this is being discussed in Section B.4.

- *Precession of perihelia*

  Massive particle motion in GR has slightly different results. It happens always along geodesics, but they have to be computed taking into account the particle masses in the energy-momentum tensor. Planets can be considered as, when orbiting the Sun, as point masses that do not curve the space, therefore the only curvature can be approximated as produced by the Sun only. As it will be shown in Subsection B.3.4 for the simple 2-Body problem, GR influences the dynamics with an additive term. This modifies all the orbital elements of all the bodies, exactly as a perturbation effect (shown in Chapter 2), but the results are more visible when talking about Mercury, because of its vicinity to the Sun, and particularly of its perihelion, the orbital parameter most affected by the space being curved. Results of GR (already just with the simple case of the Schwarzschild's solution) are actually able to explain a small orbital anomaly that the newtonian N-Body problem was not able to show alone (the effects are by the way small, over 100 years Mercury's perihelion experience a precession of $\approx 1.54°$ due to the N-Body perturbation and $\approx 43''$ due to GR).

B.3.4 *Particle motion in the Schwarzschild field*

The path to the equation of motion for a massive particle will be shown in this subsection, following what presented on [34] using Lagrange Equations and until reaching the expanded formulation of the lagrangian. The comparison between relativistic and non-relativistic case is already visible there, for the purposes of this work it does not make much sense to go deeper in the derivation in this case. A qualitative explanation of the path until the actual equations will be followed in the N-Body case, tackled in Section B.4, because that particular result is to be applied in Chapter 2.

The reader can find more details about it in [34].

All the analytical steps and assumptions can be found in [35], the purpose of this work is just to give the reader an idea about the meaning of the derivation.

In this context, the lagrangian L still equals the kinetic energy of the particle T, with the gravitational effects to lay in the metric. Reporting what already presented in Equation (A.32):

$$L = \frac{1}{2} m \mathbf{u} \cdot \mathbf{u} = \frac{1}{2} m g_{ij} \frac{dx^i}{d\tau} \frac{dx^j}{d\tau} \tag{B.33}$$

which in the Schwarzschild metric becomes (from [34]):

$$L = m\left(\frac{d\mathbf{s}}{dt}\right)^2 \left(\frac{dt}{d\tau}\right) = -mc^2 \frac{d\tau}{dt}$$
$$= -mc^2 \left\{ \left[1 + \frac{2\phi(r)}{c^2}\right] - \frac{1}{c^2}\left[\frac{\dot{r}^2}{1 + 2\phi(r)/c^2} + r^2\dot{\theta}^2 + r^2 \sin^2\theta \dot{\varphi}^2\right] \right\}^{1/2} \tag{B.34}$$

with $\phi(r) = MG/r$, the usual gravitational potential of the source of mass M as in Equation (B.9).

Some observations can be made before going on with the derivation:

- by neglecting all the terms $O(1/c^2)$ the exact newtonian lagrangian is obtained;
- terms up to $O(1/c^4)$ are deep enough to catch the relevant relativistic effects, such as Mercury's perihelion precession.

This suggests to carry out a power series expansion over $\varepsilon = 1/c^2$, to have a simplified but still analytical final form of the lagrangian L. Note that:

- the power series expansion of $1+\varepsilon$ under the square root is

$$(1+\varepsilon)^{1/2} \approx 1 + \frac{1}{2}\varepsilon - \frac{1}{8}\varepsilon^2 + ... \tag{B.35}$$

- in polar coordinates the square of the velocity is defined as

$$v^2 = \dot{r}^2 + +r^2\dot{\theta}^2 + r^2\sin^2\theta\dot{\varphi}^2 \tag{B.36}$$

Therefore, considering the terms up to $O(1/c^4)$ for what is inside the square root, L becomes:

$$L \approx -mc^2\left[1 + \frac{1}{c^2}\left(2\phi(r) - v^2 + \frac{2\phi(r)\dot{r}^2}{c^2}\right)\right]^{1/2} \tag{B.37}$$

Expanding now the square root:

$$L \approx -mc^2 - \frac{m}{2}\left(2\phi(r) - v^2 + \frac{2\phi(r)\dot{r}^2}{c^2}\right) + \frac{m}{8c^2}\left(2\phi(r) - v^2\right)^2 \tag{B.38}$$

The value $-mc^2$ is a constant and would anyway disappear in the Lagrange mechanics calculations. Neglecting it and re-organising the terms, the lagrangian L becomes:

$$L = \frac{mv^2}{2}\left(1 + \frac{v^2}{4c^2}\right) - m\phi(r)\left(1 + \frac{\dot{r}^2}{c^2} + \frac{v^2}{2c^2} - \frac{\phi}{2c^2}\right) + O(1/c^4) \tag{B.39}$$

Note that truncating the expansion to $O(1/c^2)$ would lead exactly at the Newtonian lagrangian:

$$L_{Newtonian} = \frac{mv^2}{2} - m\frac{MG}{r} \tag{B.40}$$

The usual Lagrange equations can now be used to obtain the equations of motion[8]:

$$\frac{d}{dt}\left(\frac{\partial L}{\partial \dot{x}_i}\right) - \frac{\partial L}{\partial x_i} = 0 \tag{B.41}$$

8 The lagrangian has been obtained in spherical coordinates, but it is of course possible to go back to cartesian coordinates with the usual transformation rule.

B.4 POST-NEWTONIAN MECHANICS, N-BODY RELATIVISTIC MOTION

Whenever it comes to deal with relativistic effects in a more general sense, the simple Schwarzschild's solution (treated in Section B.3) may not suffice, even though it provides an accurate mathematical support to the usual tests of GR in the Solar System. Such cases could be an higher level of precision needed or an approach capable to tackle also problems of more general nature.

In this regard, post-newtonian mechanics (PNM) is a formalism that answers to those questions and doubts, providing an analytical tool to derive the equations of motion of a generalised system, expanding all the terms in a power series over $1/c^2$ and neglecting all the terms which are $O(1/c^4)$. As it is built, this formalism is even more general than GR itself, with its scalar-coefficient-based formulation called parametrised post-newtonian mechanics (PPN), since it can be fully used also with other metric gravitational theories[9]. Particularly, PPN consists of generalising the metric into a super-metric, dependent on some scalar coefficients. The values assigned then to those coefficients will make the distinction between the different metric theories of gravity. This introduction will become more clear during the development of the section, with a discussion that will follow what presented in [35] and [36].

B.4.1 *Post-Newtonian mechanics framework*

The assumption of the gravitational field affecting the metric of the space with particles moving along geodesic remains. What distinguishes GR from the other gravitational metric theories is the way the space is affected, with laws more general than Einstein Field equations.

It is possible then to still make use of the already obtained result presented in Equation (A.35):

$$\frac{d^2x^k}{d\tau^2} + \Gamma^k_{ij}\frac{dx^i}{d\tau}\frac{dx^j}{d\tau} = 0 \tag{B.42}$$

From [35], the following expression for the acceleration is obtained, for $(i,j,k) = (1,2,3)$:

$$\begin{aligned}\frac{d^2x^i}{dt^2} &= \left(\frac{dt}{d\tau}\right)^{-1}\frac{d}{d\tau}\left[\left(\frac{dt}{d\tau}\right)^{-1}\frac{dx^i}{d\tau}\right] \\ &= \left(\frac{dt}{d\tau}\right)^{-2}\frac{d^2x^i}{d\tau^2} - \left(\frac{dt}{d\tau}\right)^{-3}\frac{d^2t}{d\tau^2}\frac{dx^i}{d\tau} \\ &= -\Gamma^i_{jk}\frac{dx^j}{dt}\frac{dx^k}{dt} + \Gamma^t_{jk}\frac{dx^j}{dt}\frac{dx^k}{dt}\frac{dx^i}{dt}\end{aligned} \tag{B.43}$$

9 The only requirement asked to these gravitational theories to be studied with the PPN formalism is to be metric theories. Examples of non-metric theories are the ones that treat quantum gravity, not reported in this thesis because going way far beyond the purposes of this work.

It is now possible to highlight all the affine connection terms involved:

$$\begin{aligned}\frac{d^2x^i}{dt^2} =& -\Gamma^i_{tt} - 2\Gamma^i_{tj}\frac{dx^j}{dt} - \Gamma^i_{jk}\frac{dx^j}{dt}\frac{dx^k}{dt} \\ &+ \left[\Gamma^t_{tt} + 2\Gamma^t_{tj}\frac{dx^j}{dt} + \Gamma^t_{jk}\frac{dx^j}{dt}\frac{dx^k}{dt}\right]\frac{dx^i}{dt}\end{aligned} \tag{B.44}$$

The goal is to obtain the accelerations up to $O(1/c^4)$, therefore the following orders are the ones needed:

The derivative operators have to be intended as $\frac{\partial}{\partial x^i} \sim \frac{1}{r}$ and $\frac{\partial}{\partial t} \sim \frac{v}{r}$, where r and v are characteristic length and velocity of the problem. They respectively lower the infinitesimal level of $1/c^2$ and $1/c$, further details and the proof can be found in [35], the link involves $c = 1$ in that book, working with slightly different units.

$$\begin{aligned}&\Gamma^i_{tt} \text{ up to } O(1/c^4); \quad \Gamma^i_{tj} \text{ up to } O(1/c^3); \\ &\Gamma^i_{jk} \text{ up to } O(1/c^2); \quad \Gamma^t_{tt} \text{ up to } O(1/c^3); \\ &\Gamma^t_{tj} \text{ up to } O(1/c^2); \quad \Gamma^t_{jk} \text{ up to } O(1/c).\end{aligned} \tag{B.45}$$

B.4.2 *Equation of motion, energy-momentum tensor, relativistic potentials*

Given Equation (B.44) and the orders needed from (B.45), one should now already have an idea of what is the actual path to follow. Detaching from the generality of PNM and underlining the path for GR, it is possible to underline a backward process that leads to the components of the affine connection Γ^i_{jk}, expressed as function of the power series expansion of the energy-momentum tensor T_{ij} (as described in Subsection B.2.3 and making use of the definitions reported in Equations (A.42), (A.40) and (A.37)).

It is worth to mention that, like for the Schwarzschild's solution presented in Section B.3, even in this framework it is possible to find a metric that is quasi-minkowskian, with the consequence to arrive to the equations that will be shown in a few lines. The detailed derivation can be found in [35].

The equation of motion for the particle n of mass m_n in an N-Body system, under this framework is:

$$\begin{aligned}\ddot{\mathbf{r}}_n =& -\vec{\nabla}\left(\phi + 2\phi^2 + \psi\right) - \dot{\vec{\zeta}} + \dot{\mathbf{r}}_n \times (\nabla \times \vec{\zeta}) \\ &+ 3\frac{d\phi}{dt}\dot{\mathbf{r}}_i + 4\dot{\mathbf{r}}_n(\nabla \cdot \dot{\mathbf{r}}_n)\phi - \|\dot{\mathbf{r}}_n\|^2\vec{\nabla}\phi\end{aligned} \tag{B.46}$$

where $\mathbf{r}_n$ is the position vector of m_n and ϕ is the newtonian potential:

$$\phi(\mathbf{r}, t) = -G\int \frac{\overset{0}{T}{}^{tt}(\mathbf{s}, t)}{\|\mathbf{r} - \mathbf{s}\|}d\mathbf{s} \tag{B.47}$$

ζ is a vectorial potential.

And the other potentials ψ and ζ are defined as:

$$\begin{aligned}\psi(\mathbf{r}, t) &= -\int \frac{1}{\|\mathbf{r} - \mathbf{s}\|}\left[\frac{1}{4\pi}\frac{\partial^2\phi(\mathbf{s}, t)}{\partial t^2} + G\,\overset{2}{T}{}^{tt}(\mathbf{s}, t) + \overset{2}{T}{}^{ii}(\mathbf{s}, t)\right]d\mathbf{s} \\ \zeta_i(\mathbf{r}, t) &= -4G\int \frac{\overset{1}{T}{}^{it}(\mathbf{s}, t)}{\|\mathbf{r} - \mathbf{s}\|}d\mathbf{s}\end{aligned} \tag{B.48}$$

with the symbol $\overset{\alpha}{A}$ denoting the term of the expansion of the quantity A to be of order $1/c^{\alpha}$ and $\mathbf{r} = (r^1, r^2, r^3)$ a generic position in the 3-dimensional space. The boundary conditions used are the newtonian limit and Minkowski metric at infinity, for the derivations of all the three potentials.

It is only left to give a definition of the energy-momentum tensor T^{ij}, which is (from [35]):

$$T^{ij}(\mathbf{r}, t) = g^{-1/2}(\mathbf{r}, t) \sum_n m_n \frac{dr_n^i(t)}{dt} \frac{dr_n^j(t)}{dt} \left(\frac{d\tau_n}{dt}\right)^{-1} \delta^3(\mathbf{r} - \mathbf{r}_n) \tag{B.49}$$

where $g(\mathbf{r}, t)$ is the determinant of the metric matrix $g^{ij}(\mathbf{r}, t)$, r^i is the $i-th$ component of the position vector $\mathbf{r}$, τ_n is the proper time for the particle n and δ^3 is a 3×3 matrix with components according to the Kronecker delta (i. e. the identity matrix).

B.4.3 *N-body barycentric equations of motion*

The equations of motion presented in Subsection B.4.2 are still general, no assumption is made on the reference frame in which they are expressed.

The reference now will be put onto a system of N point masses, each denoted with the indexes (i, j, k). A formulation of the equations of motion can be obtained in this PNM context, with a cartesian reference frame centered in the center of mass of the N-Body system. It is reported in Equation (B.50), from [25], although its derivation is available in [36]. It has been already simplified of all the extensive contributions and the conservation laws have already been exploited[10]. Note also that Einstein notation will be abandoned, to highlight better the similarities with the usual N-body problem.

The derivation in [36] takes into account the shape of the bodies, not necessarily spherical, with their mass distributions, not necessarily uniform and solid, and for rotating bodies.

$$\begin{aligned}
\ddot{\mathbf{r}}_i = &\sum_{j \neq i} \frac{\mu_j (\mathbf{r}_j - \mathbf{r}_i)}{r_{ij}^3} \Bigg\{ 1 - \frac{2(\beta + \gamma)}{c^2} \sum_{k \neq i} \frac{\mu_k}{r_{ik}} - \frac{(2\beta - 1)}{c^2} \sum_{k \neq j} \frac{\mu_k}{r_{jk}} \\
&+ \gamma \left(\frac{v_i}{c}\right)^2 + (1 + \gamma) \left(\frac{v_j}{c}\right)^2 - \frac{2(1 + \gamma)}{c^2} \dot{\mathbf{r}}_i \cdot \dot{\mathbf{r}}_j - \frac{3}{2c^2} \left[\frac{(\mathbf{r}_i - \mathbf{r}_j) \cdot \dot{\mathbf{r}}_j}{r_{ij}}\right]^2 \\
&+ \frac{1}{2c^2} (\mathbf{r}_j - \mathbf{r}_i) \cdot \ddot{\mathbf{r}}_j \Bigg\} + \frac{1}{c^2} \sum_{j \neq i} \frac{\mu_j}{r_{ij}^3} \Big\{ \big[\mathbf{r}_i - \mathbf{r}_j\big] \cdot \big[(2 + 2\gamma)\dot{\mathbf{r}}_i \\
&- (1 + 2\gamma)\dot{\mathbf{r}}_j\big] \Big\} (\dot{\mathbf{r}}_i - \dot{\mathbf{r}}_j) + \frac{3 + 4\gamma}{2c^2} \sum_{j \neq i} \frac{\mu_j \ddot{\mathbf{r}}_j}{r_{ij}}
\end{aligned} \tag{B.50}$$

10 The equations are expressed in the context of PPN, therefore they do not assume *a priori* a gravitation theory. Some of these theory allow the violation of principles like the conservation of mass, energy, linear and angular and momentum, expressing this fact with some particular values assumed by the PPN coefficients. Those last have already been set equal to 0, specific value of the same for fully conservative theories, again reported in [36].

The symbols not already mentioned are defined as:

- μ_i is the gravitational constant of body i ($\mu_i = m_i G$);
- $r_{ij} = \|\mathbf{r}_i - \mathbf{r}_j\|$;
- $v_i = \|\dot{\mathbf{r}}_i\|$;
- β and γ are the two PPN parameters that define all the *Full Conservative* gravitation theories.

It now remains to determine the values of γ and β. This is indeed done with the equivalence principle (discussed in Subsection B.2.1) formulated in the context of PNM. It suffices then to impose the equivalence of the inertial and both gravitational active and passive[11] (as reported in [36]) masses, the result obtained is "simply":

$$\gamma = \beta = 1 \tag{B.51}$$

Plugging in the values for γ and β Equation (B.50) becomes:

$$\begin{aligned}\ddot{\mathbf{r}}_i = &\sum_{j\neq i} \frac{\mu_j(\mathbf{r}_j - \mathbf{r}_i)}{r_{ij}^3}\left\{1 - \frac{4}{c^2}\sum_{k\neq i}\frac{\mu_k}{r_{ik}} - \frac{1}{c^2}\sum_{k\neq j}\frac{\mu_k}{r_{jk}} + \left(\frac{v_i}{c}\right)^2 + 2\left(\frac{v_j}{c}\right)^2\right.\\ &\left. - \frac{4}{c^2}\dot{\mathbf{r}}_i\cdot\dot{\mathbf{r}}_j - \frac{3}{2c^2}\left[\frac{(\mathbf{r}_i - \mathbf{r}_j)\cdot\dot{\mathbf{r}}_j}{r_{ij}}\right]^2 + \frac{1}{2c^2}(\mathbf{r}_j - \mathbf{r}_i)\cdot\ddot{\mathbf{r}}_j\right\}\\ &+ \frac{1}{c^2}\sum_{j\neq i}\frac{\mu_j}{r_{ij}^3}\left\{\left[\mathbf{r}_i - \mathbf{r}_j\right]\cdot\left[4\dot{\mathbf{r}}_i - 3\dot{\mathbf{r}}_j\right]\right\}(\dot{\mathbf{r}}_i - \dot{\mathbf{r}}_j) + \frac{7}{2c^2}\sum_{j\neq i}\frac{\mu_j\ddot{\mathbf{r}}_j}{r_{ij}}\end{aligned} \tag{B.52}$$

Equation (B.52) is now the starting point for what discussed in Chapter 2, where it was manipulated and used to study what effects GR has on the N-Body dynamics.

11 It is now necessary to impose the principle for both active and passive masses, meaning that each mass m_i is contributing in the generation of the gravitational field and being subjected to the attraction of the other masses m_j, whereas in the Schwarzschild case the mass m was only subjected to the source M without affecting it.

BIBLIOGRAPHY

[1] Charles H. Acton. "Ancillary data services of NASA's navigation and Ancillary Information Facility." In: *Planetary and Space Science* (1996). ISSN: 00320633. DOI: 10.1016/0032-0633(95)00107-7.

[2] European Space Agency. *Solar Orbiter Definition Study Report (Red Book)*. Tech. rep. July. 2011. DOI: 10.1088/1742-6596/271/1/011004.

[3] John D. Anderson and Giacomo Giampieri. "Theoretical Description of Spacecraft Flybys by Variation of Parameters." In: *Icarus* (1999). ISSN: 00191035. DOI: 10.1006/icar.1998.6075.

[4] Vincenzo Barone. *Relatività: Principi e Applicazioni*. Bollati e Boringhieri, 2004.

[5] A Bourdoux and D Izzo. *Characterization and hazard mitigation of resonant returning Near Earth Objects*. Tech. rep. CHMRRNEO05. 2005. URL: http://www.esa.int/gsp/ACT/doc/MAD/pub/ACT-TNT-MAD-CHMRRNEO05.pdf.

[6] Stefano Campagnola and Yasuhiro Kawakatsu. "Three-dimensional resonant hopping strategies and the Jupiter magnetospheric orbiter." In: *Journal of Guidance, Control, and Dynamics* (2012). ISSN: 07315090. DOI: 10.2514/1.53334.

[7] Stefano Campagnola and Ryan P. Russell. "Endgame problem part 2: Multibody technique and the tisserand-poincare graph." In: *Journal of Guidance, Control, and Dynamics* (2010). ISSN: 07315090. DOI: 10.2514/1.44290.

[8] Stefano Campagnola et al. "Tisserand-leveraging transfers." In: *Journal of Guidance, Control, and Dynamics* (2014). ISSN: 07315090. DOI: 10.2514/1.62369.

[9] A. Carusi, G. B. Valsechi, and R. Greenberg. "Planetary close encounters: geometry of approach and post-encounter orbital parameters." In: *Celestial Mechanics and Dynamical Astronomy* (1990). ISSN: 09232958. DOI: 10.1007/BF00050709.

[10] Matteo Ceriotti and Colin R. McInnes. "Design of ballistic three-body trajectories for continuous polar earth observation in the Earth-Moon system." In: *Acta Astronautica* (2014). ISSN: 00945765. DOI: 10.1016/j.actaastro.2014.06.001.

[11] Camilla Colombo, Francesca Letizia, and Jeroen Van Der Eynde. *SNAPPshot ESA planetary protection compliance verification software Final report, Technical Report ESA-IPL-POM-MB-LE-2015-315*. Tech. rep. University of Southampton, 2016.

[12] EADS-Astrium. "Solar Orbiter." In: *Journal of Physics: Conference Series* (2011). ISSN: 0038-0938. DOI: 10.1088/1742-6596/271/1/011004.

[13] John Guckenheimer, Philip Holmes, and M. Slemrod. "Nonlinear Oscillations Dynamical Systems, and Bifurcations of Vector Fields." In: *Journal of Applied Mechanics* (1984). ISSN: 0021-8936. DOI: 10.1115/1.3167759.

[14] E J. Opik. "Interplanetary Encounters: Close-Range Gravitational Interactions." In: 2 (1976).

[15] Jennie R. Johannesen and Louis A. D'Amario. "Europa orbiter mission trajectory design." In: *Advances in the Astronautical Sciences* (2000). ISSN: 00653438.

[16] G. Kminek. *ESA planetary protection requirements, Technical Report ESSB-ST-U-001*. Tech. rep. European Space Agency, 2012.

[17] Gregory Lantoine, Ryan P. Russell, and Stefano Campagnola. "Optimization of low-energy resonant hopping transfers between planetary moons." In: *Acta Astronautica* (2011). ISSN: 00945765. DOI: 10.1016/j.actaastro.2010.09.021.

[18] Francesca Letizia et al. "SNAPPSHOT: Suite for the numerical analysis of planetary protection." In: *6th International Conference on Astrodynamics Tools and Techniques (ICATT)*. 2016, pp. 14–17.

[19] Ya zhong Luo and Zhen Yang. *A review of uncertainty propagation in orbital mechanics*. 2017. DOI: 10.1016/j.paerosci.2016.12.002.

[20] Andrea Milani et al. "Asteroid Close Approaches: Analysis and Potential Impact Detection." In: *Asteroids III* (2002).

[21] Kenta Oshima, Stefano Campagnola, and Tomohiro Yanao. "Global search for low-thrust transfers to the Moon in the planar circular restricted three-body problem." In: *Celestial Mechanics and Dynamical Astronomy* (2017). ISSN: 15729478. DOI: 10.1007/s10569-016-9748-2.

[22] A Quarteroni, R Sacco, and F Saleri. *Numerical Mathematics Texts in Applied Mathematics*. 2007. ISBN: 9783540346586.

[23] A. J. Roberts. "The Utility of an Invariant Manifold Description of the Evolution of a Dynamical System." In: *SIAM Journal on Mathematical Analysis* (1989). ISSN: 0036-1410. DOI: 10.1137/0520094.

[24] Shane D. Ross and Daniel J. Scheeres. "Multiple Gravity Assists, Capture, and Escape in the Restricted Three-Body Problem." In: *SIAM Journal on Applied Dynamical Systems* (2007). ISSN: 1536-0040. DOI: 10.1137/060663374.

[25] P. Kenneth Seidelmann. *Explanatory Supplement To The Astronomical Almanac*. University Science Books, 1992.

[26] Francesco Topputo, Edward Belbruno, and Marian Gidea. "Resonant motion, ballistic escape, and their applications in astrodynamics." In: *Advances in Space Research* (2008). ISSN: 02731177. DOI: 10.1016/j.asr.2008.01.017.

[27] Francesco Topputo, Massimiliano Vasile, and Franco Bernelli-Zazzera. "Earth-to-moon low energy transfers targeting L1 hyperbolic transit orbits." In: *Annals of the New York Academy of Sciences* (2005). ISSN: 17496632. DOI: 10.1196/annals.1370.025.

[28] G. B. Valsecchi, E. M. Alessi, and A. Rossi. "An analytical solution for the swing-by problem." In: *Celestial Mechanics and Dynamical Astronomy* (2015). ISSN: 15729478. DOI: 10.1007/s10569-015-9631-6.

[29] G. B. Valsecchi, Cl Froeschlé, and R. Gonczi. "Modelling close encounters with Opik's theory." In: *Planetary and Space Science* (1997). ISSN: 00320633. DOI: 10.1016/S0032-0633(97)00072-X.

[30] G. B. Valsecchi et al. "Resonant returns to close approaches: Analytical theory." In: *Astronomy & Astrophysics* (2003). ISSN: 0004-6361. DOI: 10.1051/0004-6361:20031039.

[31] Giovanni B. Valsecchi. "Geometric conditions for quasi-collisions in Öpik's theory." In: *Lecture Notes in Physics* (2006). ISSN: 00758450. DOI: 10.1007/3-540-32455-0_6.

[32] Mar Vaquero and Kathleen C. Howell. "Design of transfer trajectories between resonant orbits in the Earth-Moon restricted problem." In: *Acta Astronautica* (2014). ISSN: 00945765. DOI: 10.1016/j.actaastro.2013.05.006.

[33] Mar Vaquero and Kathleen C. Howell. "Transfer design exploiting resonant orbits and manifolds in the Saturn-Titan system." In: *Journal of Spacecraft and Rockets* (2013). ISSN: 00224650. DOI: 10.2514/1.A32412.

[34] John Dirk Walecka. *Introduction to General Relativity*. 2013.

[35] Steven Weinberg. *Gravitation and Cosmology*. 1993.

[36] Clifford M. Will. *The Theoretical Tools of Experimental Gravitation*. California Institute of Technology, Pasadena (CA), USA, 1974.

[37] Ryan C. Woolley and Daniel J. Scheeres. "Applications of V-infinity leveraging maneuvers to endgame strategies for planetary moon orbiters." In: *Journal of Guidance, Control, and Dynamics* (2011). ISSN: 07315090. DOI: 10.2514/1.50428.

DECLARATION

I, Alessandro Masat, declare that whatever presented in this thesis and not specifically referenced is all work of my own, performed with the advice of my supervisors.

Milano, 18th December 2019

Alessandro Masat